The Hydrodynamic Design and Analysis of a Liquid Oxygen Pump Impeller for a Rocket Engine

Nalendran Singh

Submitted in fulfilment of the academic requirements for the degree of Master of Science in Mechanical Engineering, College of Agriculture, Engineering and Science, University of KwaZulu-Natal.

Durban, South Africa

January 2018

Supervisor: Dr Michael J Brooks

Co-Supervisor: Prof Graham DJ Smith

Co-Supervisor: Dr Glen C Snedden

EXAMINER'S COPY

DECLARATION 1 - PLAGIARISM

I, Nalendran Singh, declare that,

1. The research reported in this thesis, except where otherwise indicated, is my original research.
2. This thesis has not been submitted for any degree or examination at any other university.
3. This thesis does not contain other person's data, pictures, graphs or other information, unless specifically acknowledged as being sourced from other persons.
4. This thesis does not contain other person's writing, unless specifically acknowledged as being sourced from other researchers. Where other written sources have been quoted, then:
    i. Their words have been re-written but the general information attributed to them has been referenced
    ii. Where their exact words have been used, then their writing has been placed in italics and inside quotation marks, and referenced.
5. This thesis does not contain text, graphics or tables copied and pasted from the Internet, unless specifically acknowledged, and the source being detailed in the thesis and in the References sections.

Signed

……

Mr Nalendran Singh

As the candidate's Supervisor I agree/do not agree to the submission of this thesis.
Signed:

.....

Dr Michael J Brooks

As the candidate's Supervisor I agree/do not agree to the submission of this thesis.
Signed:

.....

Prof Graham DJ Smith

As the candidate's Supervisor I agree/do not agree to the submission of this thesis.
Signed:

.....

Dr Glen C Snedden

Acknowledgements

I would sincerely like to thank my supervisors, Dr Michael Brooks, Prof Graham Smith and Dr Glen Snedden for their guidance and advice through the duration of this study. Their encouragement and motivation allowed for this work to be complete.

I would like to specially thank the CSIR, especially Dr Snedden and Mr Radeshen Moodley, who provided access to software required to design the pump impeller and provided valuable technical advice that made this work possible. Thanks to Dr Snedden for an invitation to Pretoria to learn about the software and Mr Radeshen Moodley for hosting this interchange and providing excellent support. I would also like to thank Mr Christiaan de Wet who provided excellent support and valuable technical advice on the use of Star-CCM+™.

I would like to thank my colleague Creason Chetty, who worked on the fuel pump impeller for SAFFIRE, for providing a partner to discuss ideas and solutions for the design process. I would also like to thank Nino Wunderlin who provided the excellent renderings of SAFFIRE seen in the thesis.

Special thanks to the entirety of the ASReG and GSET group: Duran Martin, Tim Velthuysen, Kai Broughton, Dylan Williams, Chikhar Maharaj, Brandon van Bakel and Mathew Jo Mathew, for their advice and providing humour at tough times. Special thanks to past members Donald Fitzgerald and Udil Balmogim for providing advice at the inception of the project.

Thanks to Armscor for providing financial assistance throughout the study duration.

Lastly, I would like to thank my parents, Dr Sooboo Singh and Prof Mogie Singh and sister Teshnee for their support and patience throughout my studies.

Abstract

The deployment of micro- and nanosatellites has greatly increased over the past few decades with advances in miniaturized electronics for communication, imaging and attitude control. The South African satellite industry is now also currently developing two microsatellites and nanosatellites for launch by foreign providers. The outsourcing of launch services to foreign providers is costly and can lead to unanticipated delays. In this context, the UKZN Aerospace Systems Research Group (ASReG), in conjunction with the Council for Scientific and Industrial Research (CSIR) has begun designing a modular and compact liquid propulsion engine (LOX/RP-1) named SAFFIRE (South AFrican First Integrated Rocket Engine).

This dissertation details the design and analysis of the liquid oxygen pump that delivers the oxidiser to the SAFFIRE combustion chamber at high pressure, where the propellants are burnt and expelled, generating thrust. The pump is electrically powered as opposed to the conventional turbine-driven turbopump, to further simplify start-stop procedures and reduce the complexity of the engine. The pump's operating conditions were determined by an engine performance analysis, with these results forming the initial conditions for the pump design process. The oxidiser pump is required to deliver a mass flow rate of 6.13 kg/s at a pressure of 62.8 bar.

The pump was designed using conventional centrifugal pump design procedures, with special considerations taken due to the working temperature of liquid oxygen being -183°C. The final one-dimensional design for the impeller was developed using the commercial software PUMPAL™, which was provided by the CSIR. A 3D impeller geometry was developed by importing the one-dimensional design into AxCent™, where quasi-3D Multiple Stream Tube (MST) analysis and full 3D computational fluid dynamics (CFD) simulations were performed. The impeller design was refined multiple times until the parameters set by the engine performance analysis were met. The AxCent™ analyses determined that low-pressure zones occurred at the inlet of the pump impeller. Hence Star-CCM+™, which has a more robust computational solver and allows for a full transient, multiphase CFD to be performed, was employed to analyse any potential cavitation affects. The results from Star-CCM+™ and AxCent™ were compared and designs altered until a final design was realized that met the prescribed performance parameters.

The final pump impeller has an outer diameter of 86 mm, delivering a mass flow rate of 6.13 kg/s at a pressure of 64.2 bar. The pump operates at an efficiency of 60.8% requiring a power input of 51.96 kW at a rotational speed of 26000 rpm.

Table of Contents

List of Figures

Chapter 6

Appendix C

List of Tables

Appendix A

Nomenclature

Symbols	Description	Units
A	Area	[m^2]
AK	Ratio of the tip to mean meridional velocity	[-]
AR	Area ratio	[-]
b	Passage width	[m]
$BLK1$	Inlet blockage factor	[-]
c	Absolute velocity	[m/s]
CFL	Convective Courant number	[-]
c_m	Meridional velocity	[m/s]
C_p	Pressure recovery coefficient	[-]
c_u	Tangential velocity	[m/s]
D	Diameter	[m]
DR_2	Diffusion ratio	[-]
e	Nominal blade thickness	[m]
g	Gravitational acceleration	[9.81 m/s^2]
H	Head rise	[m]
i	Incidence angle	[°]
I_{sp}	Specific impulse	[s]
k	Disk friction coefficient	[-]
Km_2	Stepanoff capacity constant	[-]
$LC1$	Inlet loss coefficient	[-]
$\dot{m}$	Mass flow rate	[kg/s]
m_i	Initial mass	[kg]
m_p	Propellant mass	[kg]
$Msec/M$	Ratio of secondary mass flow to primary	[-]
N	Rotational rate	[rpm]
n_d	Dimensionless specific speed	[-]
n_q	Metric specific speed	[-]
P	Pressure	[bar]
P_{df}	Power loss due to disk friction	[W]
P_h	Hydraulic power	[W]
Q	Volumetric flow rate	[m^3/s]
r	Radius	[m]

Re	Reynolds number	[-]
T	Temperature	[K]
t_{cler}	Tip clearance	[m]
T_{0c}	Chamber stagnation temperature	[K]
Δt	Time step	[s]
Δx	Length interval	[m]
u	Tip velocity	[m/s]
v	Magnitude of the velocity relative to the mesh	[m/s]
u^*	Shear velocity	[m/s]
w	Relative velocity	[m/s]
W_{2p}	Relative velocity in the primary zone	[m/s]
y	Distance to first cell centroid	[m]
$y+$	Dimensionless wall distance	[-]

Greek Symbols	**Description**	**Units**
α	Flow angle	[°]
β	Blade angle	[°]
β_F	Blade angle before incidence	[°]
γ	Specific heat ratio	[-]
$\frac{\varepsilon}{k}$	Lennard-Jones energy parameter	[-]
η	Dynamic viscosity	[Pa.s]
η^0	Dilute gas viscosity	[Pa.s]
η^τ	Residual fluid viscosity	[Pa.s]
η_h	Hydraulic efficiency	[%]
λ	Exit swirl	[-]
ν	Kinematic viscosity	[$m^{2/}s$]
ρ	Density	[kg/m^3]
σ	Lennard-Jones size parameter	[-]
σ_b	Blade cavitation coefficient	[-]
τ_w	Wall shear stress	[Pa]
χ	Mass fraction of primary to secondary zone	[-]
ψ	Head coefficient	[-]
ω	Angular velocity	[rad/s]
ϕ	Flow coefficient	[-]
Ω	Collision integral	[-]

Subscripts	Description
c	Critical point
h	Hub
p	Pressure side
ref	Reference
s	Suction side
t	Tip
TH	Theoretical
v	Vapour
1	Impeller inlet
2	Impeller exit
3	Diffuser inlet
4	Diffuser throat
5	Volute inlet
6	Centroid from volute cutwater
7	Volute throat
8	Volute exit

Abbreviations	Description
ASReG	Aerospace Systems Research Group
B – B	Blade-to-blade loading [-]
CADB	Chemical Automatic Design Bureau
CEA	Chemical Equilibrium with Applications
CFD	Computational Fluid Dynamics
CSIR	Council for Scientific and Industrial Research
DEAN	Dual Expander Aerospike Nozzle
DNS	Direct Numerical Simulation
FSI	Fluid-Structure Interaction
GSET	Group for Solar Energy Thermodynamics
IHPRPT	Integrated High Payoff Rocket Propulsion Technology
LES	Large Eddy Simulation
LOX	Liquid oxygen
MRF	Moving Reference Frame
MST	Multiple Stream-Tube
NASA	National Aeronautics and Space Administration

NIST	National Institute of Standards and Technology
$NPSH_r$	Net Positive Suction Head required [m]
NPSS	Numerical Propulsion Simulation System
PCTFE	Polychlorotrifluoroethylene
RANS	Reynolds Averaged Navier-Stokes
RP-1	Rocket Propellant 1 (Kerosene)
RPM	Revolutions per minute
RST	Reynolds stress transport
SAFFIRE	South African First Integrated Rocket Engine
SST	Shear-Stress Transport
TEIS	Two Elements In Series
T – T	Total-to-total
UKZN	University of KwaZulu-Natal
US	United States
VOF	Volume of Fluid

Chapter 1. Introduction

1.1 Background and motivation

The capabilities of low earth orbit satellites are rapidly increasing with advances in nanosatellite technology (Woellert et al., 2011). The South African satellite industry is gradually developing, having previously developed two micro satellites that were launched by foreign providers. In early 2017, a further two South African nanosatellites were launched as part of the European Union QB50 project which aims to collect data in order to aid current atmospheric models (Anderson, 2017). The University of KwaZulu-Natal (UKZN) Aerospace Systems Research Group (ASReG) proposes the design of compact liquid engine, called the South African First Integrated Rocket Engine (SAFFIRE), for a small-satellite launch vehicle capable of placing CubeSats and nanosats into a low earth or sun synchronous orbit. The development of a rocket using these constraints, could eliminate South Africa's reliance on foreign launch services thus reducing costs and potentially enabling South Africa to become a launch provider in the small satellite market.

Liquid propellant rocket engines consist of a combustion chamber, nozzle, propellant tanks and a propellant feed system (Turner, 2006). Typically, combustion propellants (fuel and oxidiser) are supplied to the combustion chamber by a gas-driven turbopump, in which separate pump impellers are powered by a single turbine, or through a simpler pressurized gas feed system (Figure 1-1) (Haidn, 2008).

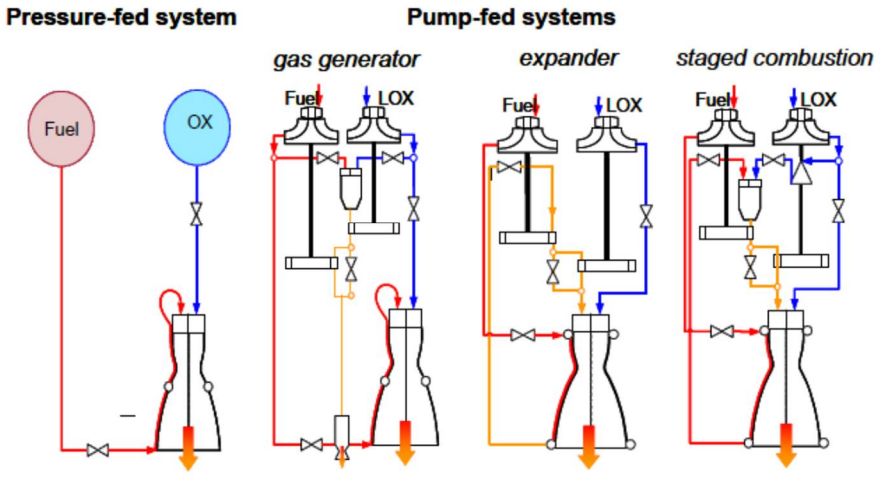

Figure 1-1: Typical liquid propulsion feed systems (Haidn, 2008)

In this study, the proposed engine SAFFIRE, will make use of electric motors, powered by battery packs, to drive the propellant pumps (Figure 1-2). The advantage of this approach is the elimination of the high-speed gas turbine, gearbox and gas generator, while allowing the pumps

to be driven independently at their optimum speeds for the greatest efficiency. Furthermore, electric motors also enable a stop-start capability, aiding operational simplicity. The rapid development of battery technology and likely improvements in power density in the coming years augur well for the future of this approach (Rachov, 2010).

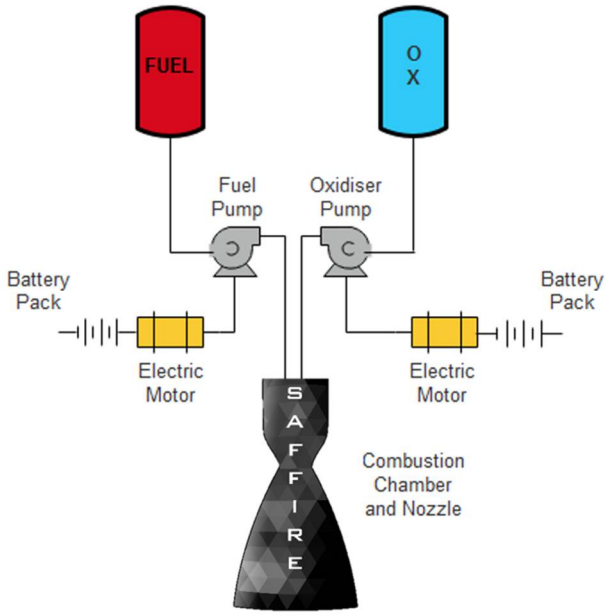

Figure 1-2: Electric feed system

ASReG has previous experience in the design of liquid propulsion rockets, having worked on the design of a launch vehicle engine with a payload capacity of 500 kg. The proposed engine utilised the gas generator cycle consisting of the two turbopumps and a single driving turbine. Smyth (2014) completed the design of the RP-1 fuel impeller along with mission outline for the accompanying launch vehicle. The fuel impeller was then further analysed using a cavitation model approach using Computational Fluid Dynamics (CFD) as developed by Richings (2015) and a test rig for a small-scaled version of the impeller was built by Philogene (2014). Lastly, the turbine for the engine was designed and analysed by Fitzgerald (2016). The experience gained in the development of this engine has aided in the development of the SAFFIRE concept.

At the time of writing, there are four studies related to the design of SAFFIRE. This dissertation details the design and analysis of the liquid oxygen oxidiser ‘electro-pump’ for SAFFIRE. The accompanying studies include the design of the fuel (RP-1) pump impeller by Chetty (2017), the design and analysis of the combustion chamber and nozzle and the design of the injector.

The primary objectives of this study are:

1) To propose a working design for a liquid oxygen pump
2) To characterise the performance of the pump using industry-standard mean-line design software
3) To validate performance using computational fluid dynamic (CFD) software

1.2 Dissertation outline

The working fluid for the oxidiser pump, liquid oxygen (LOX), is cryogenic and this increases the complexity of the design study. Chapter 2 details the various thermodynamic properties of liquid oxygen and how they affect the hydrodynamic design and material compatibility. A review of liquid oxygen pump designs and their effects on the design process is also presented.

Chapter 3 includes a survey of current and in-development small satellite launch vehicles, delivering similar payloads to the hypothetical launch vehicle. A hypothetical launch vehicle for SAFFIRE is proposed along with an appropriate mission plan. The requirements for the oxidiser pump are outlined based upon the mission plan and SAFFIRE requirements.

The hydrodynamic design of the impeller, vaneless diffuser and volute are detailed in Chapter 4. A one-dimensional mean-line design along with an applicable design space for each of the components is presented for further refinement using the commercial turbomachinery mean-line design software, PUMPAL™.

The major flow phenomena that occur within centrifugal pump impellers as well the models used to analytically realise the flow are described in Chapter 5. Chapter 5 also includes the refinement of the analytical pump design in PUMPAL™. PUMPAL™ was utilised to performed design refinement and optimisation, providing the necessary data for use in the accompanying CFD package, AxCent™. The final 3D model of the impeller and its components are presented along with quasi-3D and full 3D analyses on the impeller using AxCent™.

The impeller CFD analysis performed in AxCent™ was validated with a second CFD package, Star-CCM+™. Chapter 6 details the setup of the impeller simulation parameters in Star-CCM+™. This includes the setup of the computational domain, physics models and the generation of the mesh. A cavitation analysis was performed using Star-CCM+™, to ensure the pump met the prescribed requirements.

Chapter 7 provides a summary of the pump impeller study and includes recommendations to improve the pump performance and analysis. Lastly, considerations for the future work required to produce a working pump assembly are addressed.

Chapter 2. Overview of Liquid Oxygen

2.1 Introduction

Cryogenics is the study of fluids that exist in their liquid state at temperatures below -150°C (123K) as defined by the United States National Bureau of Standards (Haselden, 1971). Liquid oxygen (LOX) is to be used as the oxidiser for the proposed liquid rocket engine (SAFFIRE) and the thermodynamic properties, material selection and state of the art associated with LOX and LOX pumps are elaborated upon in the following sections.

2.2 Thermodynamic properties of liquid oxygen

Liquid oxygen has a characteristic blue colour due to the presence of the long chain O_4 molecule contained in the mix. Furthermore, oxygen is slightly magnetic (paramagnetic) allowing for the detection of small amounts of oxygen in mixtures. Some of the common properties of oxygen are described in Table 2-1 (Barron, 1985; Hands, 1986; Stewart and Jacobsen, 1991).

Table 2-1: Oxygen properties

Parameter	**Value**
Molecular mass [g/mol]	32.0
Boiling point at 1 atm [K]	90.2
Melting point at 1 atm [K]	54.4
Heat of vaporisation [kJ/kg]	213.0
Critical temperature [K]	154.6
Critical pressure [bar]	50.4
Critical density [kg/m$^{3]}$	436.2
Triple point temperature [K]	54.4
Triple point pressure [Pa]	146.3

The density of a propellant is an important factor in the design of the overall vehicle geometry. A high density is desirable as it allows for a more compact propellant tank design and for a larger quantity of propellant to be stored. An equation for the saturated liquid density of liquid oxygen, ρ, was determined over the course of a decade from the results of multiple experiments and data extrapolations by Pentermann and Wagner (1978) and Weber (1977). The equation was determined statistically using the least squares method and is given below in Equation 2.1 (Stewart and Jacobsen, 1991):

$$\frac{\rho}{\rho_c} = 1 + n_1\tau^{\frac{1}{3}} + n_2\tau^{\frac{2}{3}} + n_3\tau^3 \qquad [2.1]$$

where ρ_c is the critical density, $\tau = \frac{(T_c - T)}{T_c}$, T_c is the critical temperature, T is the temperature of the fluid, n_1 = 1.507678, n_2 = 0.85810805 and n_3 = 0.19035504. Figure 2-1 is the graphical representation of Equation 2.1:

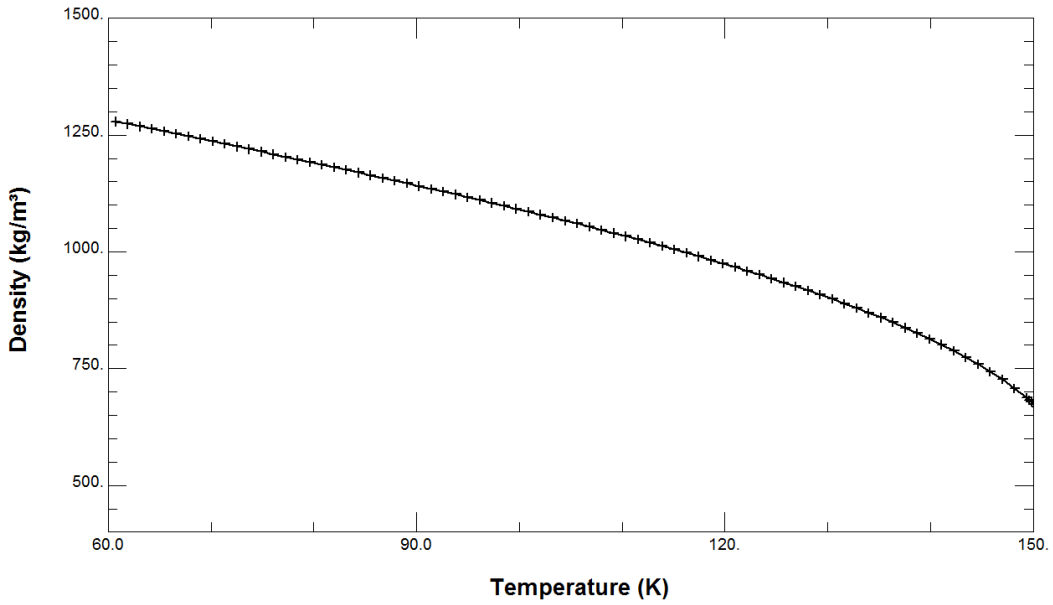

Figure 2-1: Saturated liquid density of LOX

The vapour pressure, p_v, of a fluid is the force that the vapour exerts, in thermodynamic equilibrium, upon its condensed phases. A low vapour pressure amongst propellants is desirable as it permits easier handling of propellants and reduces the potential for cavitation. Liquid oxygen has a relatively high vapour pressure thus requiring special design provisions, unique handling considerations and materials tolerant of low temperatures (Huzel and Huang, 1992; Sutton, 2001). Wagner further developed an equation for vapour pressure based on a review of published vapour pressure data and is shown described in Equation 2.2 and Figure 2-2 (Stewart and Jacobsen, 1991):

$$In\left(\frac{P_v}{P_c}\right) = \left(\frac{T_c}{T}\right)(n_1\tau + n_2\tau^{\frac{3}{2}} + n_3\tau^3 + n_4\tau^7 + n_5\tau^9) \qquad [2.2]$$

where n_1 = -6.043938, n_2 = 1.175627, n_3 = -0.994086, n_4 = -3.456781 and n_5 = 3.361499.

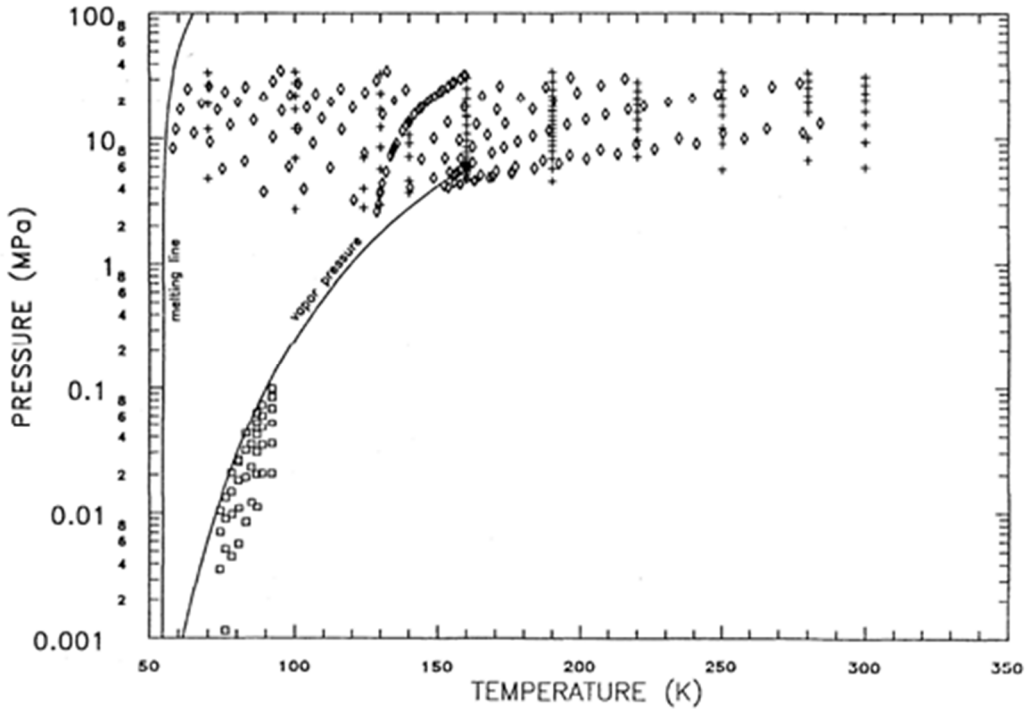

Figure 2-2: Vapour pressure of liquid oxygen (Stewart and Jacobsen, 1991)

The transport properties of LOX, especially dynamic viscosity, are important to consider when performing the hydrodynamic design as well as the computational analysis of the impeller. Viscosity affects the amount of liquid shear in the impeller and can reduce the pressure output of the pump. Lemmon and Jacobsen (2004) developed standardised equations for the calculation of viscosity based on experimental work and extrapolation by researchers at the National Institute of Standards and Technology (NIST). The viscosity of liquid oxygen is given in the form of Equation 2.3:

$$\eta = \eta^0(T) + \eta^\tau(\tau, \delta) \qquad [2.3]$$

where η is the viscosity of liquid oxygen at a given temperature. η^0 and η^τ are the dilute gas and residual fluid viscosities and are given by Equation 2.4 and Equation 2.5 respectively (Lemmon and Jacobsen, 2004):

$$\eta^0(T) = \frac{0.0266958\sqrt{MT}}{\sigma^2\Omega(T^*)} \qquad [2.4]$$

where σ is the Lennard-Jones size parameter. The collision integral (Ω) and the temperature (T^*) is given by $\Omega(T^*) = \exp\left(\sum_{i=0}^{4} b_i[In(T^*)]^i\right)$ and $T^* = \frac{T}{\left(\frac{\epsilon}{k}\right)}$ respectively. $\left(\frac{\epsilon}{k}\right)$ is the Lennard-Jones energy parameter.

$$\eta^{\tau}(\tau,\delta) = \sum_{i=1}^{n} N_i \tau^{t_i} \delta^{d_i} \exp(-\gamma_i \delta^{l_i}) \qquad [2.5]$$

All data for the parameters and coefficients in Equations 2.4 and 2.5 are included in Table A-1. Equations 2.3, 2.4 and 2.5 are used in combination to form Figure 2-3 which shows the relationship between viscosity and temperature.

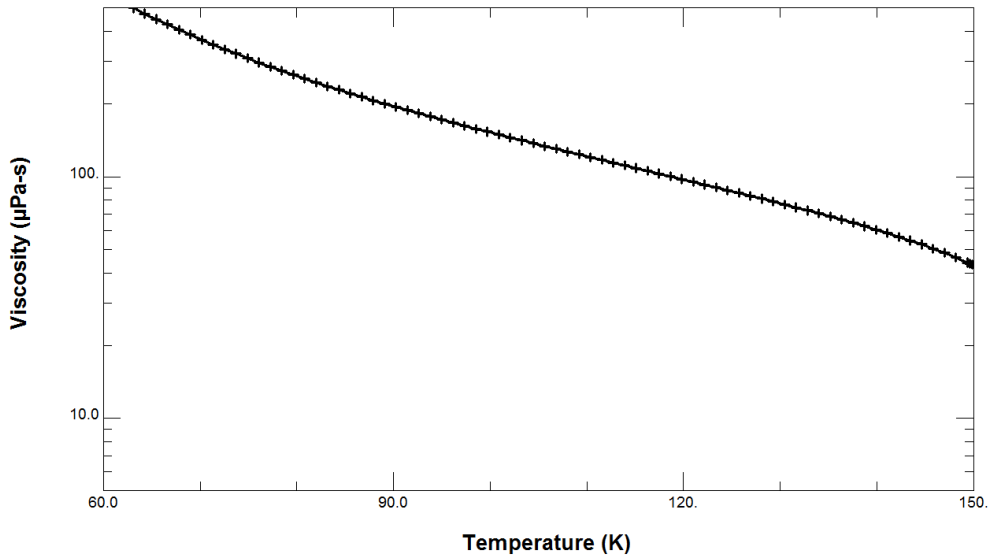

Figure 2-3: Viscosity versus temperature

Liquid oxygen utilised in the aerospace industry is produced using cryogenic air separation units that provide a high purity (> 99.5%), high volume and high pressure product. For use as a propellant, liquid oxygen has specific production requirements (Malone, 1976). These are defined by the military specification MIL-P-25508B and requirements of which are given in Table 2-2.

Table 2-2: Oxygen purity requirements (Malone, 1976)

Requirement	**Value**
Purity [%]	99.5+
Carbon [ppm]	< 25
Moisture [ppm]	< 26.3
Acetylene [ppm]	< 0.5

2.3 Material selection for LOX

Proper material selection is essential in cryogenic systems as the correct material for the application can reduce the probability of system failure. The final selection of cryogenic materials

often involves a compromise between the varying properties (strength, conductivity and cost) and the fluid in question. In order to make an educated decision on the material choice , the cryogenic engineer is therefore required to have a wide knowledge base of material properties and their advantages which is generally gained through experience using cryogenic systems (Haselden, 1971). However, various NASA monographs and other texts provide general guidelines to aid in the selection of materials for oxygen systems (NASA, 1996). The broad guidelines are as follows:

1. The use of non-metals in oxygen systems is to be limited since non-metals are prone to ignition more so than metals.
2. An experience based material database is to be utilised for systems operating in the range of pressures, 1 – 20.7 MPa.
3. Information pertaining to the operating and safety system such as material compositions, operational conditions and the material ignition behaviour is required.
4. Materials utilised in oxygen systems are required to be certified by the manufacturer. The material should also have satisfactory physical properties.

2.3.1 Non-metallic materials

Non-metallic materials are rarely utilised in the design of oxygen systems. However, some materials such as elastomers, polymers and lubricants are used due to their advantageous properties. The following section will deal briefly with the use of various elastomers and composites in oxygen systems.

2.3.1.1 Elastomers

Elastomers are generally used for components such as O-rings and diaphragms due to their flexibility and their low glass transition temperature. For O-rings, Kalrez is a commonly used fluorinated elastomer due to its low glass transition temperature and good low temperature performance (Kalia and Fu, 2013).

2.3.1.2 Composites and polymers

Polymers, which are used extensively in some oxygen applications, are flammable in the presence of oxygen but, through proper design considerations the risk of ignition can be minimized. The most common cause of polymeric ignition is through adiabatic compression heating due to rapid pressurization (NASA, 1996). It is therefore advised that systems containing polymers are pressurized relatively slowly. Polymer materials utilised in aerospace applications are generally employed as electrical and thermal insulators as well as vacuum sealants (Kalia and Fu, 2013).

The mechanical properties of polymers at cryogenic temperatures are a major concern in the design of successful oxygen systems. Fibre-reinforced composites are generally unsuitable for cryogenic applications due to the unequal coefficients of thermal expansion between the fibres and the matrix. This results in internal stresses in the material and can lead to micro-cracking of the composite matrix which is detrimental to the mechanical properties and can lead to material failure (Kalia and Fu, 2013).

Thermal expansion is a crucial parameter when selecting polymers for cryogenic oxygen systems. Detailed knowledge of thermal expansion of composite materials is advantageous in the design of cryogenic systems as it allows for safer structural design and correct dimensional stability and strength (Kanagaraj and Pattanayak, 2004). Fibre based composites generally have low thermal expansion ratios which is desirable for cryogenic applications. Carbon fibre, which has been recently used as propellant tanks, has a slight negative thermal expansion ratio resulting in a slight expansion of the tank at cryogenic temperatures. Carbon fibre tanks were previously utilised using an inner liner material in order to prevent micro cracking in the composite matrix (Performance Composites, 2017). However, SpaceX plan to use one of the first fully carbon fibre tanks without a liner for their Interplanetary Transport System to Mars. Figure 2-4 shows the completed carbon fibre tank (Milberg, 2016).

Figure 2-4: SpaceX carbon fibre liquid oxygen propellant tank (Milberg, 2016)

Epoxy resins are generally used as insulators, vacuum sealants and matrix materials for cryogenic oxygen systems. The resins provide good properties in severe cryogenic environments but are largely brittle with thermal cycling leading to fractures of the resin. The resin matrix tends to become stiff at temperatures of 77 K due to the restrained mobility of the molecules. This results in a higher tensile strength of epoxy resin composites at 77 K as compared to the same material at room temperature (Kalia and Fu, 2013).

2.3.2 Metallic materials

Metals are frequently used in the construction and manufacturing of oxygen systems and components. They are generally less susceptible to ignition as compared to non-metals, with critical ignition occurring due other organic matter or an added polymer containment. As with non-metallic components, proper material selection can reduce ignition and combustion hazards. Metals such as iron and aluminium have protective oxide coatings providing an increased resistance to ignition. There are four main metal alloys that are used in the construction of an 'oxygen system' (NASA, 1996).

2.3.2.1 Nickel and Nickel alloys

Nickel and nickel alloys are a very common material used in the construction of oxygen systems due to their high strength, excellent low temperature toughness and very high corrosion resistance. They possess very low thermal conductivity and are commonly used in components where heat influxes are to be minimized (Haselden, 1971). There are two common alloys are: nickel-iron (Inconel) and nickel-copper (Monel) alloys.

Inconel 718

Inconel 718 is a nickel-chromium-molybdenum superalloy that is extensively utilised in the aerospace industry due to its wide resistance range to severely corrosive environments and resistance to pitting and crevice corrosion. It is especially useful due to its wide temperature range limit that extends from cryogenic temperatures up to higher temperatures of approximately 650ºC. A special feature of Inconel 718 is the addition of niobium, which age hardens the alloy, allowing the alloy to be welded and annealed without spontaneous hardening. Niobium interacts with molybdenum which stiffens the alloy's matrix, offering a higher strength material without requiring heat treatment (High Performance Alloys, 2013).

Inconel 718 has been successfully used at pressures of up to 69 MPa and possesses good structural properties with an increased ignition resistance as compared to stainless steel (NASA, 1996). The good structural properties include excellent mechanical properties such as tensile, fatigue and creep rupture, yield strength, a great range of temperature resistances as well as excellent welding characteristics due to the age hardening. Furthermore, Inconel possesses low thermal conductivity, as well as high hardness and strength at high temperatures as well as cryogenic temperatures (Ono et al., 2006). Inconel 718 has been used successfully in multiple rocket engines, most notably in Space Shuttle Main Engine (SSME) whereby it compromised 51% of the engine weight and was included in the main components such as the LOX/LH2 turbopump and the thrust chamber (Jewett and Halchak, 1991).

Monel Alloy

Monel is a nickel-copper alloy that has the highest ignition resistance of all commonly used structural materials. It has excellent particle impact resistance and has resisted combustion in flammability tests in oxygen rich environments at pressures above 69 MPa. However, frictional heating tests have resulted in ignition in some cases but usually at higher loads than stainless steel. Although Monel has excellent ignition resistances, precautions should still be taken to ensure ignition sources are minimized (NASA, 1996).

The major disadvantage of Monel is its higher density as compared to other alloys and it is rarely utilised in flight systems. Monel K-500 is commonly used for valve stems and valve bodies, and is generally utilised in ground based systems. Monel sections are used in key areas in an aerospace system when extra ignition protection is desired. The sections are to be limited as weight is an important constraint in aerospace system (NASA, 1996).

2.3.2.2 Stainless Steel

Stainless steels are used in high pressure oxygen systems due to their superior ignition and burn resistance as compared to other metals such as titanium and aluminium alloys. They are commonly used in oxygen feed systems as storage tanks and lines. They are less commonly used as valves due to ignition occurring in some cases at high pressures. Furthermore, stainless steel is easily ignited by frictional heating and particle impact (NASA, 1996).

2.3.2.3 Copper and Copper Alloys

Copper and its alloys were among the first metals used for cryogenic purposes and are extensively used in oxygen systems at varying pressures, including high pressure systems. The yield strength of copper gradually increases up to pressures of 69 MPa (10 000 psi). Furthermore, the ultimate tensile strength of copper increases significantly at low temperatures. Lastly, the percentage elongation at low temperatures is increased resulting in extremely ductile failure at all temperatures (Haselden, 1971).

Copper is usually utilised for impingement plates due to its excellent resistance to particle impact ignition. Although it is resistant to ignition and combustion, contamination can occur in some systems due to a low ductility oxide that easily sheds off the material. Bronze is also a common option for oxygen systems, being less flammable than Monel and stainless steel for filter element material (NASA, 1996).

2.3.2.4 Aluminium and Aluminium Alloys

Aluminium and its alloys are widely used in aerospace and aeronautical applications due to their numerous favourable characteristics such as the high strength to weight ratios, good availability and ease of fabrication (Haselden, 1971). They are almost exclusively used in aerospace systems as pressure vessels and most importantly for lightweight structures where there are no credible ignition hazards. Aluminium-magnesium alloys in particular are prized for their strength and are primarily used in the construction of large storage tanks (Haselden, 1971; NASA, 1996).

Heat-treated alloys such as copper and magnesium-silicon, have increased yield and tensile strength at the cost of ductility. Magnesium-silicon alloy type 6061 is widely used as cryogenic tanks and has a greater resistance to ignition through mechanical impact tests up to pressures of 69 MPa. The stronger copper-aluminium alloy is less widely used due to a complicated welding process. A variation of the alloy, type 2014, was used as the material for the cryogenic tanks of the Saturn rockets (Haselden, 1971).

Aluminium is easily ignitable in high pressure oxygen and it is recommended that aluminium lines and valves be avoided. Aluminium is also easily ignited through friction, as the frictional wear erodes the protective oxide layer. Furthermore, it is easily ignitable by particle impact and aluminium particulate in the flow provides an effective ignition source which is undesirable. If aluminium is a necessity, filters (materials such as bronze and Monel are suitable) are required in the flow to eliminate any aluminium particulate (NASA, 1996).

2.3.3 Material selection

Inconel 718 was selected as the design material of choice for the oxidiser pump impeller in this study, due to its excellent low temperature properties and extensive use by NASA in their oxidiser pump impellers (Furst, 1973). It possesses excellent welding characteristics, can be readily fabricated, is cost effective and the recent advent of Inconel 3D printing further supports its use. 3D printing is especially advantageous due to the complex geometry of the impeller. The properties of Inconel 718 at approximately 80 K are given in Table 2-3.

Table 2-3: Inconel 718 properties (Special Metals, 2017)

Property	**Value**
Tensile strength [MPa]	1634.05
Density [kg/m^3]	8199
Poisson's ratio	0.25
Young's modulus [GPa]	215.805

2.4 LOX pump design state of the art

The earliest example of liquid oxygen pumps in rocketry was the use of a LOX turbopump in the German V2 rocket during World War 2. From that time onwards, liquid oxygen has been the oxidiser of choice in liquid based aerospace applications (Scott, 1963). This section discusses three different LOX pump designs.

2.4.1 LE-5 LOX pump

The LE-5 engine was developed in 1981 for the medium payload launch vehicle designated H-1. The rocket utilised a liquid hydrogen and oxygen propellant combination and the LE-5 liquid oxygen pump was powered by a gas generator cycle impulse turbine. It consisted of a single-stage centrifugal pump with a swept back inducer. Aluminium alloys were used in the construction of both the pump impeller and the casing with Inconel 718 being used as the shaft material. Liquid oxygen was used to cool the ball bearings, and a face contact seal was used as the main shaft seal (Kamijo et al., 1982). The specifications of the LOX turbopump are given in Table 2-4. The locations of the seals for the pump are shown in Figure 2-5.

Table 2-4: LE-5 LOX pump specifications

Parameter	**LOX Turbopump**
Speed [rpm]	16 500
$NPSH_{required}$ [m]	7.5
Delivery pressure [bar]	53.2
Mass flow rate [kg/s]	19.4
Efficiency [%]	65.8

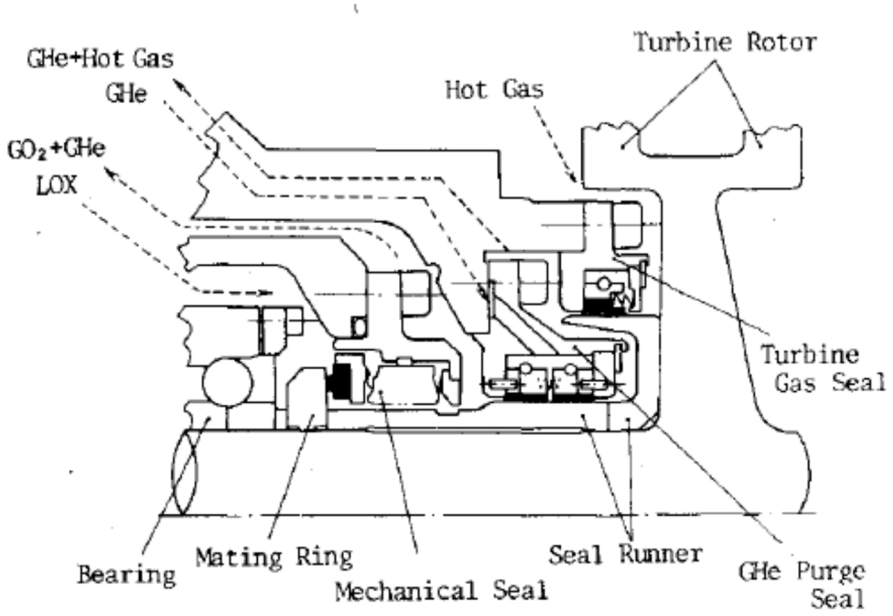

Figure 2-5: LOX turbopump shaft seal (Kamijo et al., 1982)

2.4.2 The Advanced Liquid Oxygen (ALO) turbopump

The ALO turbopump was developed by the Chemical Automatic Design Bureau (CADB) of Russia under the contract of Pratt and Whitney. The turbopump was designed for the upper stage of an expander cycle engine delivering 222 kN of thrust. The ALO was developed using a standardised design approach established from the development and design of prior turbopumps (Dimitrenko et al., 2000).

Tests were performed to determine the performance and cavitation of the pump, as well as the determination of thrust balance requirements and tests of the bearings and seals. Table 2-5 gives the results obtained from the subsequent tests.

Table 2-5: ALO testing results

Parameter	**Value**
Suction specific speed [-]	51.66
Head coefficient [-]	0.35
Pump efficiency [%]	69
Turbine efficiency [%]	75

2.4.3 Liquid oxygen pump design for the Dual Expander Aerospike Nozzle Engine

The DEAN engine LOX pump was designed for an upper stage dual expander cycle LOX/H_2 engine in support of the Integrated High Payoff Rocket Propulsion Technology (IHPRPT) program phase 3 goals (Strain, 2008). Strain (2008) was tasked with the design of the liquid oxygen pump for the engine as part of his masters thesis. He developed the one-dimensional design for the LOX pump using PUMPAL™, a one-dimensional mean-line design software developed by Concepts NREC. The design point for the pump was obtained using NASA's Numerical Propulsion Simulation System (NPSS) and is shown in Table 2-6 (Concepts NREC, 2016):

Table 2-6: DEAN pump design point

Parameter	**Value**
Pump inlet pressure [bar]	3.1
Pump outlet pressure [bar]	310
Mass flow rate [kg/s]	48.1
Shaft speed [rpm]	32 000

The design point values were used to develop a mean-line design in PUMPAL™. PUMPAL™ has two available modes; design and analysis. Design mode provides the pump parameters at the design point as prescribed by the user whereas analysis mode is used to determine the off-design performance of the pump (Strain, 2008). The final performance parameters of the pump are given in Table 2-7:

Table 2-7: DEAN pump performance parameters

Parameter	**Value**
Outlet pressure [bar]	319.6
Inlet blade number	7
Outlet blade number	14
Total-to-total (T – T) efficiency [%]	77.3
Non-dimensional specific speed [-]	0.32

2.5 Summary

Liquid oxygen pumps require special consideration due to their thermodynamic and chemical requirements. This includes the following:

1. Appropriate material selection to avoid incompatible materials or materials that may result in contamination and inadvertent combustion
2. Consideration of the operating conditions of the pump with respect to properties such as the density and vapour pressure of LOX
3. Appropriate bearing and seal selection is vital to reduce wear and increase lifetime performance
4. Use of conventional turbopump design procedures

Chapter 3. SAFFIRE Launch Vehicle and Pump Parameters

3.1 Introduction

This chapter outlines the launch capacity and performance of a vehicle designed using the proposed engine. This includes a brief survey of existing launch vehicles, a hypothetical vehicle and mission plan and the proposed engine and pump specifications.

3.2 Survey of current launch vehicles

The hypothetical launch vehicle for SAFFIRE is expected to compete in the small satellite launch vehicle market. To realistically configure a vehicle, a survey of similarly sized launch rockets was performed. These include vehicles developed by Rocket Lab (Electron), Firefly Space Systems (Firefly Alpha) and Vector Space Systems (Vector-R).

3.2.1 Rocket Lab Electron launch vehicle

Rocket Lab is a US owned but New Zealand based aerospace company primarily focused on the small satellite industry. They plan to provide cheaper access to space, promising payloads of up to 150 kg, deliverable to 500 km sun-synchronous orbits. Development of the Electron launch vehicle began in the late 2010 with funding provided through various US and New Zealand private companies. The engine, known as the Rutherford, is among the first to be 3D printed, with an expected print time of approximately 24 hours (Rocket Lab, 2017). The engine and the launch vehicle are shown in Figure 3-1.

(a) (b)

Figure 3-1: (a) Rutherford engine and (b) the Electron launch vehicle (Rocket Lab, 2017)

In 2015, Rocket Lab began the development of two launch sites for the Electron vehicle, with their main site located in Mahia, New Zealand. This site was completed and operational by the

end of 2016 and the first successful launch of the Electron vehicle took place on 25th May 2017. The completed launch facility and the subsequent launch are shown in Figure 3-2 and Figure 3-3 respectively (Rocket Lab, 2017).

Figure 3-2: Mahia launch site (Rocket Lab, 2017)

Figure 3-3: First launch of Electron (Rocket Lab, 2017)

Electron is two-stage rocket utilising nine Rutherford engines in its first stage and one vacuum optimised Rutherford engine in its second stage. The Rutherford engine uses a LOX/RP-1 propellant combination and is driven by two electric motors provided 37.29 kW at 40000 rpm. The electric motors are brushless DC motors and are powered using lithium polymer batteries.

The basic launch vehicle specifications for both the first and second stage are shown in Table 3-1 and the payload specifications are shown in Table 3-2 (Rocket Lab, 2017; Spaceflight 101, 2017).

Table 3-1: Electron launch vehicle specifications

Vehicle parameter	**First stage**	**Second stage**
Length [m]	12.1	2.4
Inert mass [kg]	950	250
Propellant mass [kg]	9250	2150
Thrust (sea-level) [kN]	152	-
Thrust (vacuum) [kN]	183	22
Specific impulse [s]	303 (sea-level)	333 (vacuum)
Burn time [s]	155	320

Table 3-2: Electron payload capacity

Fairing parameter	**Value**
Diameter [m]	1.2
Length [m]	2.5
Mass [kg]	50
Payload capacity [kg]	150

3.2.2 Firefly Alpha

Firefly Space Systems developed the Alpha launch vehicle primarily to compete in the small satellite market, with an expected payload capacity of 200 kg to a sun-synchronous orbit. The developed engine utilises pressure-fed system as opposed to conventional turbo pumps. The vehicle also makes use of one of the first commercial aerospike nozzles, to increase the efficiency of the nozzle throughout a range of external air pressures. The vehicle as well as the aerospike nozzle configuration are shown below in Figure 3-4.

(a) (b)

Figure 3-4: (a) Aerospike nozzle and (b) Alpha launch vehicle (Firefly Space Systems, 2017)

The specifications for the Firefly Alpha launch vehicle and the engine specifications are described in Table 3-3 (Firefly Space Systems, 2017).

Table 3-3: Firefly Alpha specifications

Vehicle parameter	**Stage 1**
Thrust (sea-level) [kN]	443
Isp (vacuum) [s]	299
Length [m]	16.7
Payload capacity [kg]	200

3.2.3 Vector-R rocket

Like Rocket Lab, Vector Space Systems also aims to provide affordable and reliable space access for low-cost micro satellites. They have developed two rockets (Vector-R and Vector-H) to aid in achieving these purposes. Currently, the Vector-R is the only version which has undergone a successful test and has the capability to place a 66 kg payload into orbit. Vector Space aims to provide 100 launches per year for the Vector-R version and plan to begin commercial flights in 2018 (Vector Space Systems, 2017).

The Vector-R utilises a pressurized gas propulsion system, utilising three first stage engines with a propellant mixture of LOX and propylene. The performance specifications for the Vector-R is given in Table 3-4 (Vector Space Systems, 2017).

Table 3-4: Vector-R performance specifications

Parameter	Value
Thrust (sea-level) [kN]	66.7
Payload capacity [kg]	66
Height [m]	12
Total mass [kg]	6000

The Vector-R underwent a successful low altitude flight test in August 2017 and is shown on the launch pad in Figure 3-5.

Figure 3-5: Vector-R rocket (Vector Space Systems, 2017)

The launch vehicle survey conducted in this study aided in forming a baseline for the first iteration of the SAFFIRE launch vehicle, which is required to possess similar launch capabilities to the vehicles mentioned previously.

3.3 Hypothetical launch vehicle and mission plan

The primary objective of the SAFFIRE engine, is to deliver a payload into orbit, and for this reason a hypothetical launch vehicle design is proposed along with a mission plan.

3.3.1 Hypothetical launch vehicle

The proposed launch vehicle is required to achieve a 500 km sun-synchronous orbit where a small payload (±75 kg) can be positioned. The payload capability of the launch vehicle was determined using Silverbird Astronautics Launch Vehicle Performance Calculator (Schilling, 2009). To utilise Silverbird, the launch vehicle parameters as well as the engine parameters are required. The launch vehicle was designed, with the parameters of the previous three surveyed commercial vehicles in mind, by the calculation of the "delta V" budget for the proposed launch requirement. The delta V budget allows for the calculation of the respective propellant and dry masses of the vehicle. This budget and the launch vehicle parameter calculations are described in greater detail by Chetty (2017). The parameters for the hypothetical launch vehicle drawn from his work are given in Table 3-5.

Table 3-5: Launch vehicle parameters

Parameter	**1st stage**	**2nd stage**
Dry mass [kg]	950	250
Final mass (m_f) [kg]	3380.9	375
Propellant mass (m_p) [kg]	9905.2	2055.9
Mass ratio (final/initial)	0.25	0.15
Delta V per stage [m/s]	3960.6	5940.8
Propellant mass fraction (m_p/m_i)	0.75	0.85

3.3.2 SAFFIRE parameters

The calculation of the engine parameters allows for the payload capacity of the launch vehicle to be determined and provides an initial design point for the oxidiser pump. The engine design is highly iterative and requires a few parameters to be assumed for the design and performance specifications to be determined. Two fixed parameters were chosen for the engine, namely the thrust output and the nozzle throat area.

NASA Chemical Equilibrium with Applications (CEA)™ software and the isentropic nozzle flow functions were utilised to determine the minimum required chamber pressure to maintain the prescribed thrust input. CEA™ provides the specific impulse (I_{sp}), chamber stagnation temperature (T_{0c}) and the specific heat ratio (γ) allowing for the chamber pressure to be calculated using the isentropic nozzle flow functions. The chamber pressure is required by CEA™ to determine the previously described parameters thus forming an iterative loop. The iterative loop was considered as converged once the inputs of the isentropic nozzle flow functions met the

outputs of CEA™. The final parameters of SAFFIRE, generated using the isentropic nozzle flow functions and CEA™, are given in Table 3-6. The iterative process for the design parameters of the engine is described in more detail by Chetty (2017). A rendering of the final engine configuration is shown in Table 3-6.

Table 3-6: SAFFIRE final engine parameters

SAFFIRE parameters	**Sea level conditions**	**Vacuum conditions**
Thrust [kN]	25	27.46
Chamber pressure [bar]	50	50
Mass flow rate of propellants [kg/s]	8.88	8.88
Specific impulse [s]	295	324

Figure 3-6: SAFFIRE configuration (Wunderlin et al., 2017)

For the prescribed performance to be achieved, the first stage of the launch vehicle must comprise a cluster of engines. This allows for the performance targets to be achieved while ensuring that SAFFIRE is a compact and small engine allowing for easier manufacturing and testing. The cluster configuration to be utilised is the SpaceX termed Octaweb design that has been successfully used on their Falcon series of rockets and more recently used by Rocket Lab, on their Electron launch vehicle. The cluster configuration is shown in Figure 3-7.

Figure 3-7: First stage SAFFIRE cluster configuration (Wunderlin et al., 2017)

3.3.3 Launch vehicle performance summary

The parameters determined in Sections 3.3.1 and 3.3.2, were utilised in Silverbird's Launch Vehicle Performance Calculator to provide the final payload capability of the launch vehicle. The overall launch vehicle performance is given in Table 3-7.

Table 3-7: Launch vehicle performance parameters

Parameter	**Value**
Take-off thrust-to-weight ratio	1.7
Payload [kg]	75
Fairing mass [kg]	50
First stage jettison time [s]	127.4
Total ascent time [s]	365.4

3.4 Oxidiser pump requirements

The engine parameters described in Section 3.3.2 can be used to determine the required output of the oxidiser electro-pump. The key output parameters derived are the delivery mass flow rate and working pressure of the oxidiser pump.

The calculation of the delivery pressure of the pump requires the pressure drop across the feedline to be determined. This includes losses due to friction in the pipes, fittings and entrances and the pressure drop across the injector. The injector is used to provide the correct oxidiser-to-fuel ratio for combustion at a constant pressure of 50 bar. Huzel and Huang (1992) recommend a 20% allowance for the pressure drop across the injector based upon the chamber pressure, which equates to a drop of 10 bar across the SAFFIRE injector and an inlet injector pressure of 60 bar.

The pressure drop in the feedline is dependent on the design of the plumbing connecting the propellant tanks with the inlet of the pump. A generic feedline layout developed by Chetty (2017) was utilised and losses due to pipe fittings and the friction in the pipes were calculated to be 2.8 bar. The calculations and data defining the feedline are shown in Table 3-8. This gives a final output pressure of 62.8 bar for the oxidiser pump.

Table 3-8: Pump feed system to combustion chamber

Parameter	**Value**
Effective pipe length	5
Number of bends	2
Friction factor	0.042
Injector loss [bar]	10
Internal pipe diameter [m]	0.032
Liquid oxygen density [kg/m^3]	1191.0
Combustion chamber pressure [bar]	50
Loss coefficients	
90-degree bends	1.5
Entrance loss	0.78
Pipe velocity	6.40
Calculations	
Head loss due to friction [m]	13.70
Minor head losses [m]	9.98
Required pump delivery pressure [Pa]	**6276640.4**
Required pump delivery pressure [bar]	**62.8**

The mass flow rate through the oxidiser pump is the next requirement to be determined through the engine analysis. The flow rate is calculated using the O/F ratio and the total propellant mass flow rate. The given propellant flow rate is 8.88 kg/s as stated in Section 3.3.2 and the O/F ratio

for SAFFIRE was calculated to be 2.45 during the engine performance analysis. This gives a mass flow rate for the oxidiser pump of 6.13 kg/s.

The liquid oxygen properties at the pump inlet must be considered so as to avoid two-phase flow and allow for the assumption of incompressible flow through the impeller for the analytical design. An inlet suction pressure of 3 bar was established through consideration of existing designs (Furst, 1973). Furthermore, an inlet fluid temperature of 80 K was selected as compared to the boiling point temperature of 90 K. This increases the density of the fluid from 1140 kg/m^3 to 1191.0 kg/m^3 allowing for a more compact vehicle geometry. The vapour pressure decreases, as shown in Figure 2-2, to 0.3 bar allowing for an increased suction performance at the inlet of the pump. Table 3-9 gives the properties of liquid oxygen at the pump inlet.

Table 3-9: LOX properties at pump inlet

Liquid Oxygen Properties	**Value**
Inlet pressure [bar]	3
Inlet temperature [K]	80
Density [kg/m^3]	1191.0
Vapour pressure [bar]	0.3

The temperature-entropy diagram shown in Figure 3-8 displays the common regimes for a multi-phase fluid, namely the liquid phase on the left, two-phase flow under the "dome" and the gaseous state on the right. An issue concerning liquid oxygen pumps is when the pumps operate above the critical point which may result in the flow being compressible (Japikse et al., 1997).

Typical pump operation occurs along a single line on the left-hand side of the temperature-entropy diagram describing an unsaturated, incompressible liquid. Assuming an adiabatic process, a state line can be drawn from the 3 to 62 bar line for the liquid oxygen pump operation, as shown in Figure 3-9.

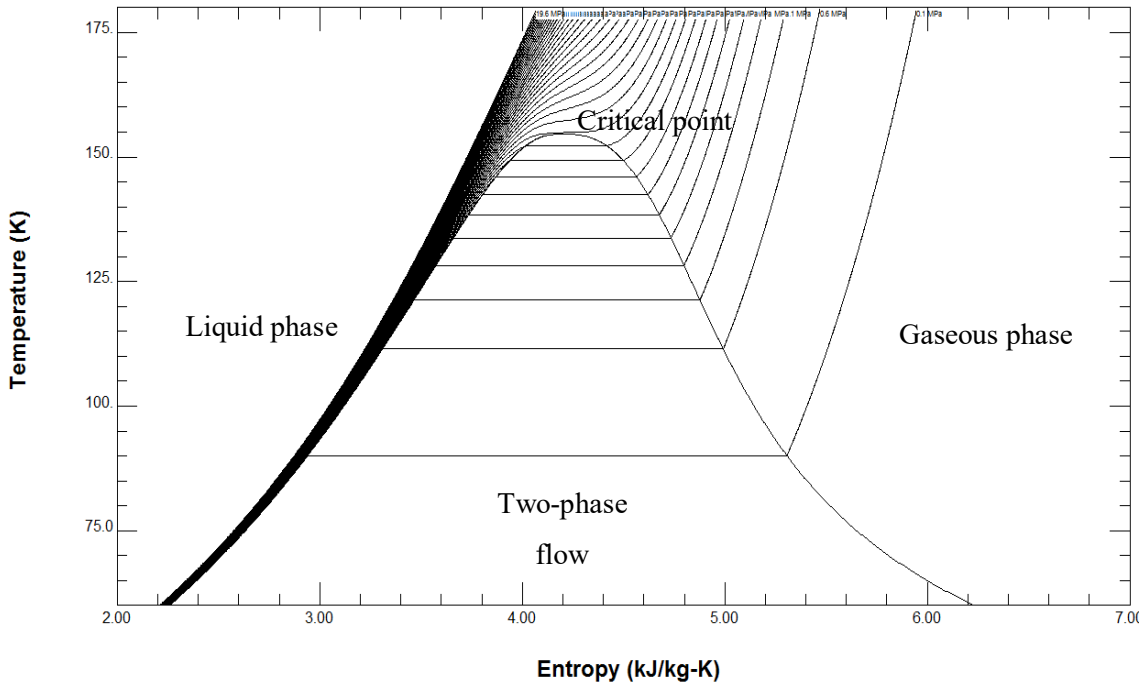

Figure 3-8: Temperature-entropy diagram for liquid oxygen

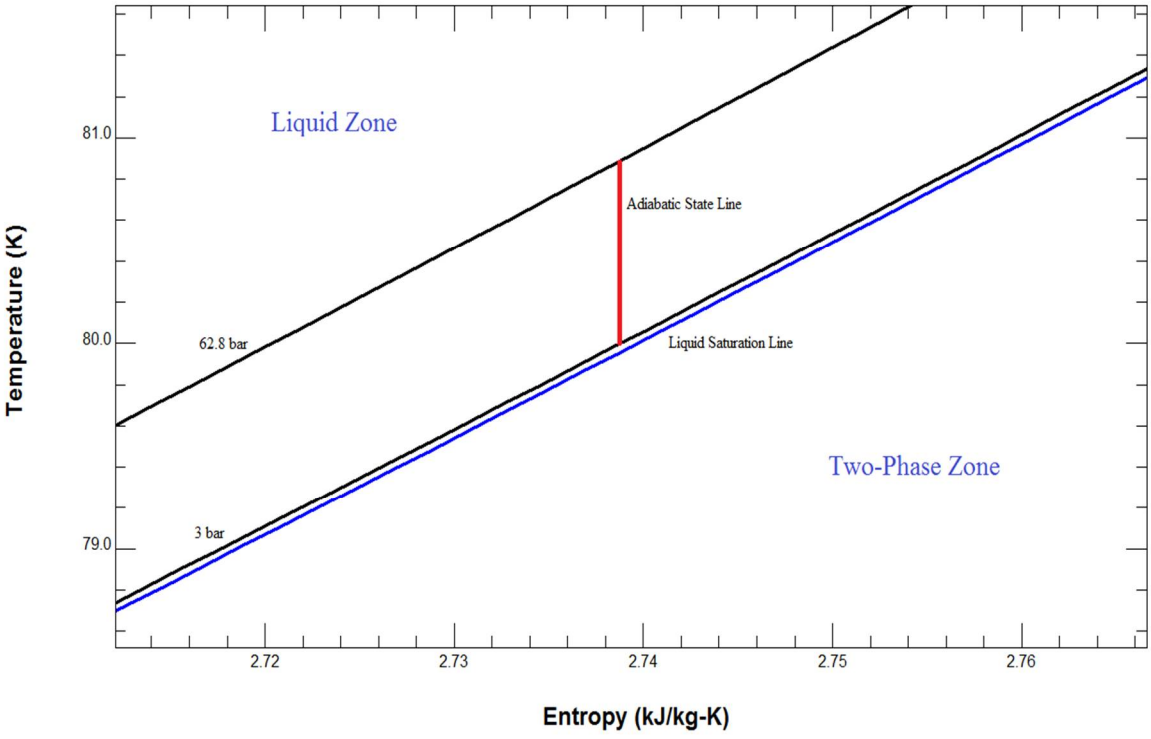

Figure 3-9: State-line for liquid oxygen pump

This shows that the operation of the LOX pump occurs on the left-hand side of the T-s diagram, indicating that the flow is incompressible. The final pump requirements as derived in this section are shown in Table 3-10.

Table 3-10: Summary of SAFFIRE LOX pump parameters

Pump parameters	**Value**
Tank pressure [bar]	3
Temperature [K]	80
Density [kg/m^3]	1190.98
Discharge pressure [bar]	62.8
Head rise [m]	511.54
Mass flow rate [kg/s]	6.13
Volumetric flow rate [m^3/s]	0.005147

Chapter 4. Hydrodynamic Design

4.1 Introduction

The one-dimensional analytical designs of the impeller, diffuser and volute are discussed in this chapter. The derived parameters in this chapter are required to form a design range in which the final one-dimensional pump design can be iterated in PUMPAL™.

4.2 Pump impeller design

The pump impeller is the most critical component in the design of the electro-pump. The design methodology for a liquid oxygen (cryogenic) centrifugal pump follows the same standards as conventional pumps as explained in Section 2.4 and a general design procedure is followed using design guides as prescribed by NASA (Furst, 1973), Huzel and Huang (1992) and Japikse et al. (1997).

The performance parameters for the LOX pump were established by the feed system design described in Section 3.4. The salient parameters are repeated in Table 4-1 as the starting point of the iteration.

Table 4-1: Pump performance parameters

Pump parameter	**Value**
Pump pressure rise [bar]	59.8
Head rise [m]	511.54
Mass flow rate [kg/s]	6.13
Volumetric flow rate [m^3/s]	0.005147

The analytical design for the oxidiser pump is an iterative process, with various key parameters requiring to be estimated to determine an appropriate design range. Calculations for the analytical design were performed at the inlet and outlet of the impeller. The iterative process for the analytical design is outlined in Figure 4-1.

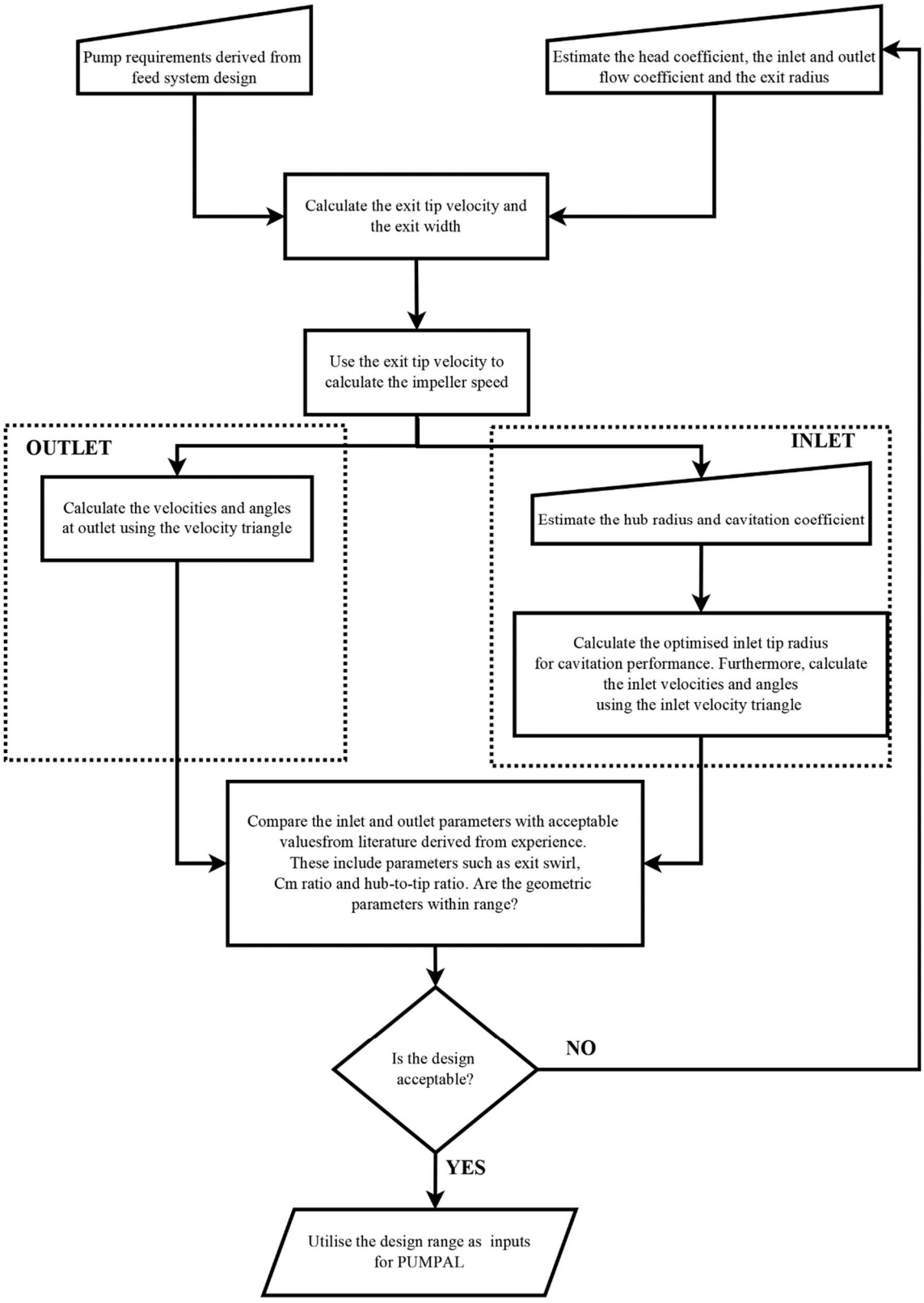

Figure 4-1: Methodology for analytical design

The key parameters for the analytical design are required to be estimated. The parameters used in the final analytical design are given in Table 4-2, along with the reasoning behind the choices.

Table 4-2: Fixed pump parameters

Parameter	**Value**	**Comment**
Head coefficient (ψ)	0.55	Moderate head coefficient value as recommended in literature (Furst, 1973; Huzel and Huang, 1992; Japikse et al., 1997).
Inlet flow coefficient (ϕ_1)	0.13	Chosen from a range of values (0.07 – 0.30) recommended in literature (Furst, 1973; Huzel and Huang, 1992)
Discharge flow coefficient (ϕ_2)	0.09	Chosen from a range of values (0.01 – 0.15) recommended in literature (Furst, 1973; Huzel and Huang, 1992)
Outlet impeller radius (r_2) [m]	0.04	Constrained by the geometry of the launch vehicle, and through iteration between the flow and head coefficient, provides the best compromise between speed and blade height.
Inlet hub radius (r_{1h}) [m]	0.01	Small hub radius selected to ensure a smaller hub-to-tip ratio (υ)
Inlet flow angle (α_1) [°]	90	Typical for radial blading

The analytical design utilises a one-dimensional mean-line modelling method. The mean-line method is used to determine the various geometric and performance characteristics of the pump at different points or stages by assuming the bulk flow conditions are represented by a point. This allows for rapid concept generation and evaluation and is commonly used in the early stages of design. Figure 4-2 gives the various components of the pump with a corresponding section number, beginning at the impeller leading edge (1) and ending at the pump discharge or volute exit (8).

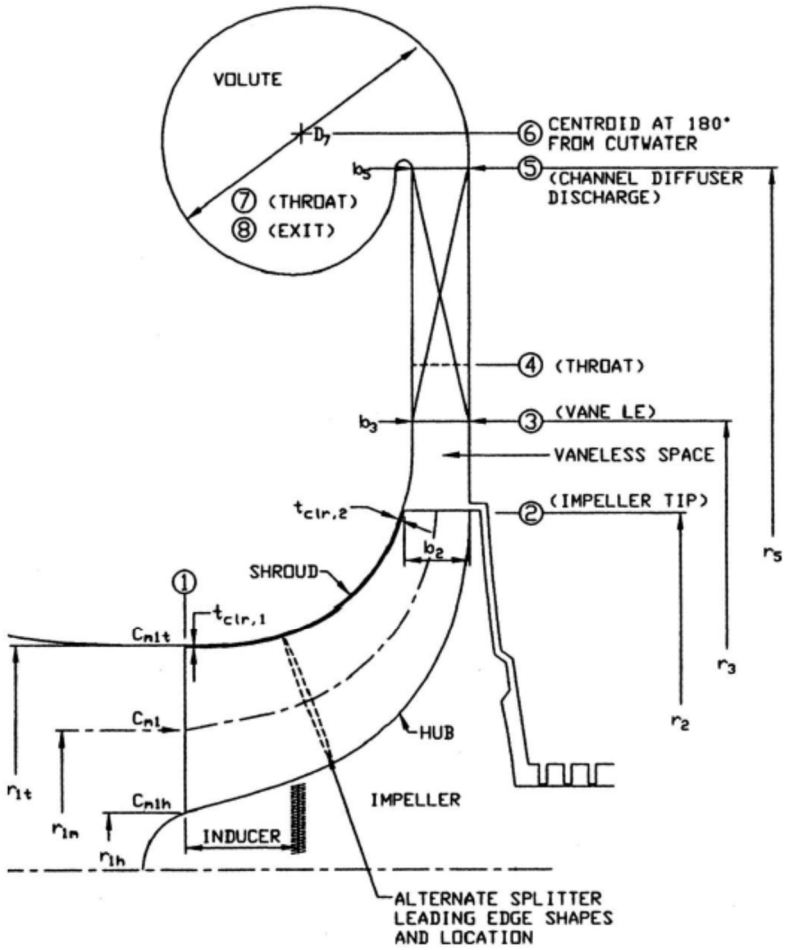

Figure 4-2: Meridional pump layout showing major mean-line stations (Japikse et al., 1997)

Using the head coefficient and discharge flow coefficient, the outlet parameters of the impeller were first calculated.

4.2.1 Impeller outlet

The head coefficient (ψ) of a pump impeller is defined by Equation 4.1:

$$\psi = \frac{gH}{{u_2}^2} \qquad [4.1]$$

where H is the head rise through the impeller in [m] and u_2 is the blade tip velocity at exit in [m/s]. Equation 4.1 allows for the blade tip velocity at the impeller exit to be determined. Using the estimated exit radius (r_2) and the newly calculated tip velocity, the rotational speed (N) of the impeller can be determined through Equations 4.2 and 4.3:

$$\omega = \frac{u_2}{r_2} \qquad [4.2]$$

$$N = \omega \times \frac{180}{\pi} \qquad [4.3]$$

where ω is the angular velocity of the impeller in [rad/s]. The specific speed (N_D) of a pump is an important characteristic used to classify pumps based upon their speed and head rise. The dimensionless units for specific speed are calculated using Equation 4.4:

$$N_D = \omega \frac{\sqrt{Q}}{(gH)^{0.75}} \qquad [4.4]$$

where Q is the volumetric flow rate in [m^3/s]. A dimensionless specific speed of 0.3 for the pump was determined. Figure 4-3 is a pump chart that is utilised to determine the type of pump impeller as well as the impeller blading used as per the specific speed (Brennen, 1994). The proposed pump impeller lies on the left of the chart, lying just within the centrifugal pump and radial blading zone. This trait is common amongst pumps which have a high pressure head as well as a low mass flow rate (Gulich, 2014).

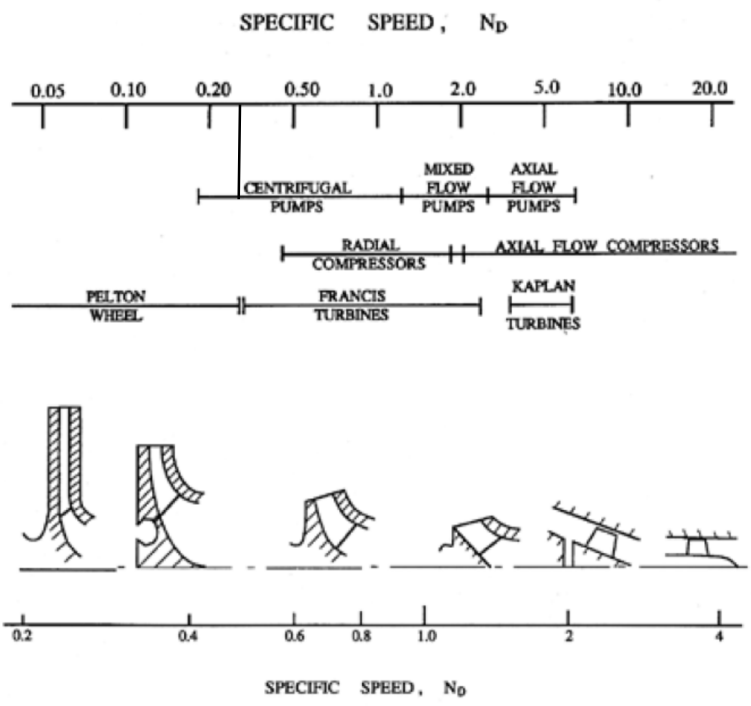

Figure 4-3: Specific speed chart (Brennen, 1994)

Ideal velocity diagrams for centrifugal pumps are utilised in one-dimensional analysis to determine the velocity profiles through the LOX pump impeller. The outlet velocity triangle (Figure 4-4) allows for the calculation of important quantities such as the impeller exit blade angle (β_2).

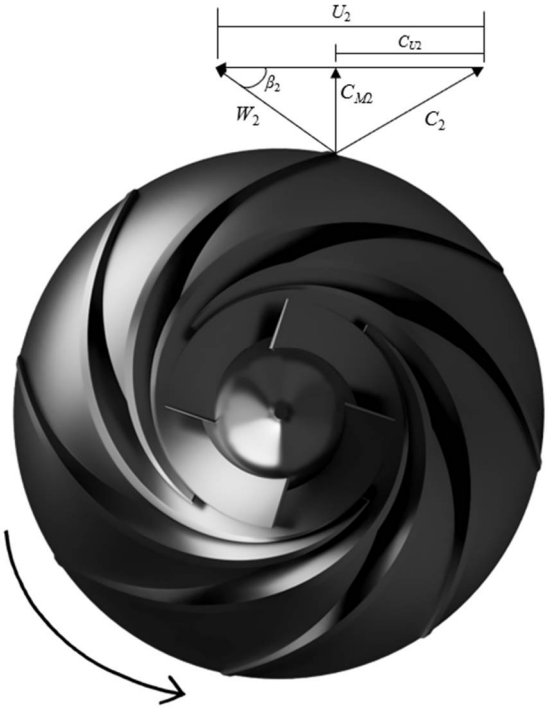

Figure 4-4: Outlet velocity triangle

The meridional velocity at the impeller outlet, (c_{m2}), is dependent upon the flow coefficient at discharge, ϕ_2, and the impeller tip speed. This is defined by Equation 4.5:

$$\emptyset_2 = \frac{c_{m2}}{u_2} \qquad [4.5]$$

The exit width, b_2, of the impeller can be calculated using the knowledge that the meridional flow velocity is related to the flow rate through the exit area of the impeller. The exit width is calculated using Equation 4.6.

$$b_2 = \frac{\dot{m}}{2\pi\rho r_2 u_2 \phi_2} \qquad [4.6]$$

where $\dot{m}$ is the mass flow rate in [kg/s] and ρ is the fluid density in [kg/m^3]. The circumferential component of the absolute velocity (c_{u2}) is determined by the measured head across the impeller (Gulich, 2014). By assuming the measured head is equal to the desired head, the theoretical circumferential velocity can be calculated and is determined by Equation 4.7. The impeller design assumes radial blading, thus negating the effect of inlet swirl (Gulich, 2014). Due to this effect, the circumferential velocity at the inlet (c_{u1}) is negligible.

$$c_{u2TH} = \frac{gH}{\eta_h u_2} + \frac{u_1 c_{u1}}{u_2} \quad [4.7]$$

In the above, η_h is the hydraulic efficiency of the pump. The outlet impeller blade angle is dependent upon the outlet meridional velocity, exit tip velocity and the outlet circumferential velocity. The relationship between these quantities is shown graphically in Figure 4-4 and the blade angle is calculated from Equation 4.8:

$$\beta_2 = \tan^{-1}\left(\frac{c_{m2}}{u_2 - c_{u2}}\right) \quad [4.8]$$

The required hydraulic power for the pump can be determined using the pump performance parameters in conjunction with the hydraulic efficiency. Gulich (2014) provides a performance parameter for the estimated hydraulic efficiency of a centrifugal pump as shown in Equation 4.9. The estimation utilises the specific speed (n_q) and the flow rate of the impeller and does not include other secondary flow effects that would naturally occur. The estimation is provided so as to form a basis to proceed in the design.

$$\eta_h = 1 - 0.055\left(\frac{Q_{ref}}{Q}\right)^m - 0.2\left(0.26 - \log\frac{n_q}{25}\right)^2\left(\frac{Q_{ref}}{Q}\right)^{0.1} \quad [4.9]$$

In the above, Q_{ref} is set to 1 m^3/s. From Equation 4.9, the hydraulic power (P_h) is determined using Equation 4.10:

$$P_h = \frac{\rho g Q H}{\eta_h} \quad [4.10]$$

4.2.2 Impeller inlet

The impeller inlet flow design space is determined through the definitions of the hub radius, cavitation coefficient, pump speed and the inlet flow coefficient. The tip radius is an important consideration in centrifugal pump designs, as a relatively high hub-to-tip ratio (greater than 0.75) leads to increasing efficiency losses (Huzel and Huang, 1992; Oh and Chung, 1999). A hub radius of 10 mm was selected in accordance with this consideration, along with a cavitation coefficient of 0.1 as recommended by Japikse et al. (1997). Furthermore, a zero-inlet swirl option was determined due to the omission of an inducer. The result of this simplification is an inlet angle (α_1) of 90°, in turn reducing c_{u1} to zero and the simplification of the original inlet velocity triangle as shown in Figure 4-5.

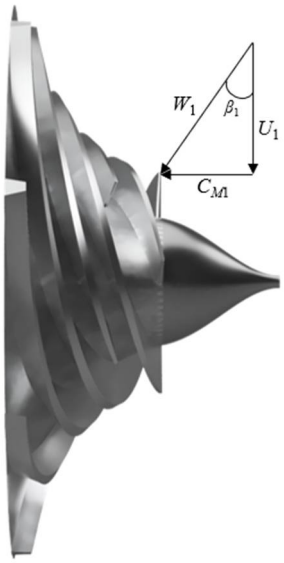

Figure 4-5: Inlet velocity triangle

For conventional liquid pumping systems, it is desirable to operate at the highest possible speed, with the only limiting factor being the occurrence of cavitation. Cavitation is a fluid phenomenon that occurs at the pump inlet when the local static pressure of the fluid drops below the vapour pressure of the fluid (Stripling and Acosta, 1962). This results in the formation of gas bubbles in the flow. The bubbles impinge on blade surfaces causing localized implosions which result in the wearing of the blades, reducing the performance of the pump. Extensive cavitation leads to appreciable mixing losses, distorting the flow field disrupting the power transmission to the flow (Stripling and Acosta, 1962).

The effect of cavitation in the eye of the pump impeller is an important concern with regards to the tip radius. Japikse et al. (1997) recommend a common optimisation strategy for the impeller inlet focussing on blade cavitation rather than optimizing the inlet for best efficiency. Flow entering the impeller, accelerates through the restricted area caused by blade blockage which creates a drop in local static pressure. The blade cavitation coefficient (σ_b) is used in the empirical approach to define the local pressure at the blade surface as shown in Equation 4.11. The coefficient represents the fraction of inlet kinetic energy involved in the local acceleration of the flow (Japikse et al., 1997).

$$p = p_{1t} - \sigma_b \left(\frac{1}{2}\rho w_{1t}^2\right) \qquad [4.11]$$

In the above, p is the static pressure at the blade surface in [Pa], p_{1t} is the static pressure at the tip of the inlet blades in [Pa] and w_{1t} is the relative velocity at the tip in [m/s].

Equation 4.12 is the optimized equation for an inlet radius (r_{1t}) of minimum $NPSH_r$, thus reducing the risk of cavitation, for a fixed hub radius and cavitation coefficient:

$$r_{1t}{}^2 = r_{1h}{}^2 + \left[\left(\frac{30}{\pi N}\right)^2 \frac{2Q^2}{\pi^2} \frac{1+\sigma_b}{\sigma_b}\right]^{\frac{1}{3}} \quad [4.12]$$

The inlet blade angle is dependent upon the inlet flow coefficient and the incidence angle (i) of the blading. This relationship is described by Equation 4.13:

$$\beta_1 = \beta_{F1} + i \quad [4.13]$$

$$= \tan^{-1} \emptyset_1 + i$$

The incidence angle for centrifugal pumps is advised to be at a minimum such that the suction specific speed at the inlet is maximised and is recommended to be in the region of 0 - 4° (Furst, 1973; Japikse et al., 1997). However, it is advised that incidence is non-zero, in order to increase the inlet blade angle such that local shock losses at the design flow rate are avoided (Ardizzon and Pavesi, 1998). An impeller inlet incidence angle of 2° was chosen as it lies within the recommended range of 0 – 4° and is non-zero to avoid shock losses mentioned above at inlet.

4.3 Vaneless diffuser and volute design

The vaneless diffuser and the volute design were not the primary focus of this work but were defined using empirical relationships defined through experience and testing. The vaneless diffuser [points 3 to 5 in Figure 4-2] is formed by the gap between the discharge of the impeller and the volute tongue. The diffuser acts a mixing zone for the discharge wakes of the impeller and diffuses the flow with an increase in flow passage area. The vaneless diffuser is inherently inexpensive and avoids complications such as blade fatigue failure in vaned diffusers (Japikse et al., 1997).

The exit radius and width of the diffuser is based upon the inlet diffuser parameters, which are the same as the exit from the impeller. Empirical ratios have been developed through extensive testing that relate the exit and inlet geometry of the diffuser and stipulate a range of values for which the design would perform most efficiently. The ranges given for the diffuser radius and width are shown in Equations 4.14 and 4.15 (Furst, 1973; Japikse et al., 1997; Gulich, 2014):

$$1.00 \leq \frac{r_{outlet}}{r_{inlet}} \leq 1.30 \quad [4.14]$$

$$1.10 \leq \frac{b_{outlet}}{b_{inlet}} \leq 1.50 \qquad [4.15]$$

Amirante et al. (2016) suggests minimising the ratio of the length of the diffusion passage to the width to below 4 in order to reduce passage losses and increase the performance and efficiency of the diffuser.

The volute is used to convert the kinetic energy in the flow to static pressure by leading the flow through a scroll which is increasing in area as it approaches the discharge pipe. The circular symmetrical scroll volute type is the most common in use as it shows the best performance and efficiency of the various volute types (Japikse et al., 1997). A schematic of the typical scroll volute is shown in Figure 4-6 :

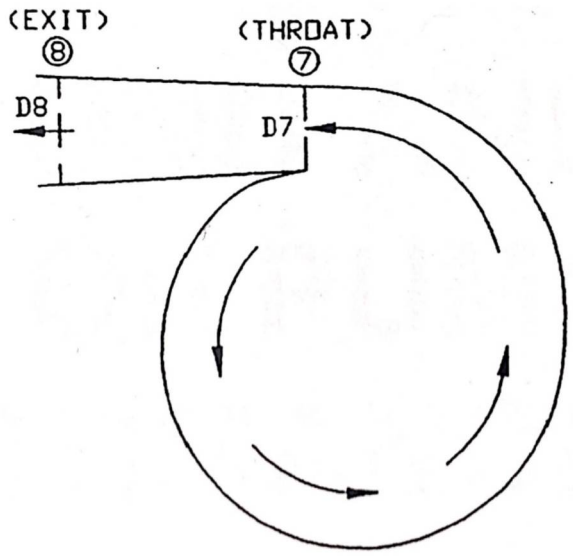

Figure 4-6: Schematic of typical scroll volute (Japikse et al., 1997)

The volute can be modelled using a geometric area ratio (AR) which relates the area at the throat (A_7) to the inlet area of the volute (A_5). The area ratio is described in Equation 4.16.

$$AR = \frac{A_7}{A_5} = \frac{\pi D_7^2}{8\pi r_5 b_5} \qquad [4.16]$$

where the area at the throat (A_7) may be calculated by dividing the volumetric flow rate through the throat (Q) by the absolute velocity (C_7), D_7 is the diameter at the throat in [m], r_5 is the radius at the volute inlet in [m] and b_5 is the width at volute inlet in [m]. C_7 is related to the tip velocity at the impeller outlet and can be determined as function of the US specific speed (785.76) of the pump using Figure 4-7:

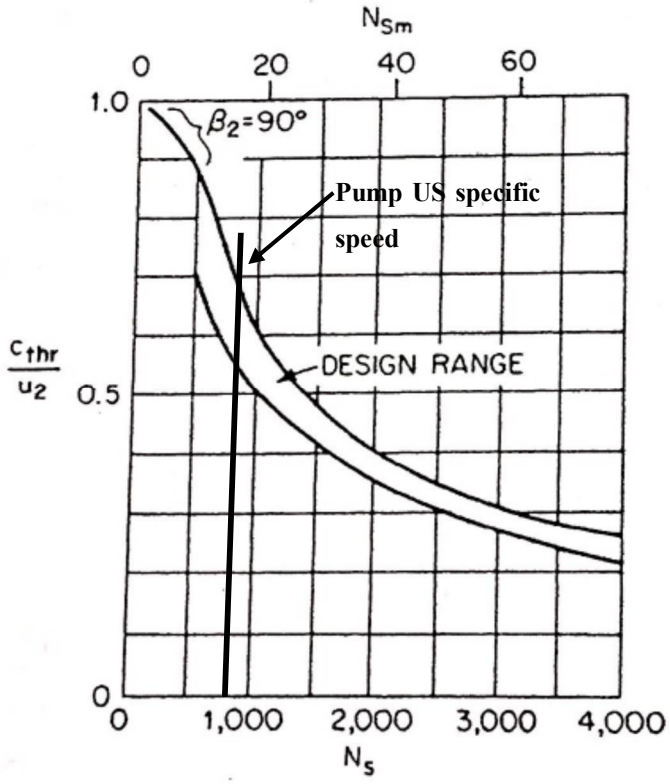

Figure 4-7: Volute throat velocity as a function of specifc speed (Karassik et al., 2001)

Using the calculated throat velocity, the area ratio is determined. The pressure recovery coefficient (C_p) of the volute can be calculated using the area ratio and the diffuser exit swirl parameter (λ). Assuming the flow diffuses through the volute, one can calculate the coefficient using Equation 4.17.

$$C_p = \frac{2\left(\lambda - \frac{1}{AR}\right)}{AR(1+\lambda^2)} \qquad [4.17]$$

4.4 Analytical design summary

Table 4-3 summarises the preliminary design determined by the mean-line analytical analysis. The pump delivers a mass flow rate of 6.13 kg/s at a rotational speed of 26061 rpm. It has an inlet tip diameter of 35.2 mm and an outlet diameter of 80 mm.

Table 4-3: Summary of analytical design

Upstream conditions	
Tank pressure [bar]	3
Inlet temperature [K]	80
Density [kg/m^3]	1191.0
Mass flow rate [kg/s]	6.13
Rotational speed [rpm]	26061
Impeller inlet	
Hub radius [mm]	10
Cavitation coefficient	0.1
Tip radius [mm]	17.6
Incidence angle [°]	2
Blade angle [°]	11.03
Tip velocity [m/s]	48.03
Impeller outlet	
Exit radius [mm]	40
Exit width [mm]	2.0
Blade angle [°]	19.3
Tip velocity [m/s]	109.2
Exit swirl	7.14
Specific speed [dimensionless]	0.30
Vaneless diffuser	
$\frac{r_{outlet}}{r_{inlet}}$	1.04
$\frac{b_{outlet}}{b_{inlet}}$	1.2
l/b ratio	3.9
Volute	
Exit diameter [mm]	32
Pressure recovery coefficient	0.1148

Chapter 5. Oxidiser Pump Analysis

5.1 Introduction

The preliminary design developed through Chapter 4 was further explored and refined using the commercial mean-line software PUMPAL™. PUMPAL™, developed by Concepts NREC, is a specialised pump design package that allows for mean-line design optimisation. It contains the necessary tools to design the pump stage, analyse and refine the performance and apply several performances models to model the machine (Concepts NREC, 2016b). PUMPAL™ allows for the generation of major centrifugal pump components (the impeller, vaneless diffuser and scroll volute) and has direct communication with AxCent™, also developed by Concepts NREC. The PUMPAL™ geometry is transferred to AxCent™ where detailed 3D blade design and geometric detailing can be performed. AxCent™ can further prototype the design using its rapid flow analysis multiple stream-tube (MST) analysis to provide more accurate performance characteristics as compared to PUMPAL™'s 1D mean-line code. Lastly, AxCent™ has a built-in computational fluid dynamics (CFD) solver which encompasses turbulence models and a full Navier-Stokes solver to provide a representation of the flow through the impeller and performance characteristics of the pump (Concepts NREC, 2016a). The process of obtaining the final pump design is described in the subsequent sections.

5.2 Methodology

The 3D design and analysis of the impeller is an iterative process between PUMPAL™ and AxCent™, specifically the MST solver. The 1D design developed from the analytical calculations were first refined using PUMPAL™. The PUMPAL™ design is more realistic than the analytical design as complex flow and loss models are built into the code but not included in the analytical design. The flow and loss models are discussed in further detail in Section 5.3.1. PUMPAL™ attempts to determine suitable outlet characteristics for the specified upstream conditions and inlet parameters of the pump. The design was refined by exploring the various parameters that could be controlled. This included varying inlet parameters such as the hub radius (r_{1h}) and outlet parameters such as the exit blade angle (β_2). PUMPAL™ allows for the exclusive refinement of a single parameter through two methods: design helper and analysis mode. Design helper generates a design space based upon a desired variable and a user defined independent variable. Using this method, one can optimise a certain parameter to attain the highest efficiency or geometrically constrain the pump such that a more compact design is achieved. Analysis mode fixes the geometry of the pump and allows for the user to vary a single parameter and explore how this affects the performance of the pump as compared to the original design output. Figure 5-1 describes the process utilised to obtain the final impeller design.

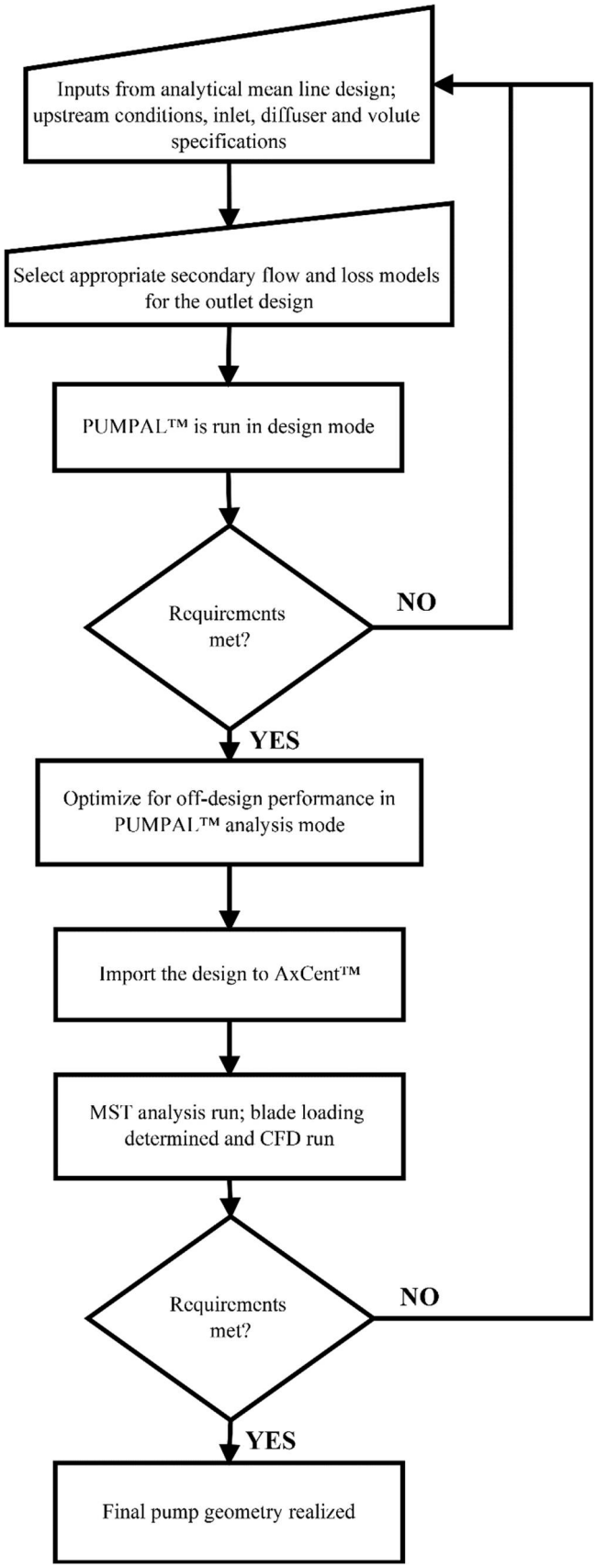

Figure 5-1: Design methodology for PUMPAL™ and AxCent™

5.3 PUMPAL™ and MST analysis

Concepts NREC PUMPAL™ has a built-in mean-line code that aids in one-dimensional design of the impeller. The software encompasses flow models for expected secondary flow losses and utilises a two-zone model, for one-dimensional design (Japikse et al., 1997). Values from the design space developed through the analytical design are used as inputs for the PUMPAL™ design. The design was then further refined using the MST analysis method in AxCent™. The flow and loss models utilised in PUMPAL™ are described in the subsequent section.

5.3.1 Flow and loss models

PUMPAL™ uses empirically derived models to simulate the flow through the impeller. This section covers the various models used by PUMPAL™ and other important flow phenomena.

5.3.1.1 Two-zone impeller models

The two-zone model was developed as an alternative to the conventional design process which involved modelling each source of loss separately. The conventional design led to challenges in finding correlations for each loss source at design. Detailed flow field analyses by Dean (1974) and Johnson and Moore (1980) determined that a jet-wake flow pattern occurs at impeller exit; the wake flow region encompassed most of the losses while the jet-region remained essentially loss free and isentropic in nature. This allows for the separation of the flow into two flow zones namely the primary (jet) and secondary (wake) regions (Gu et al., 2010). This approach allows for realistic numerical modelling of the impeller exit flow in the design stage.

The primary zone of the flow consists of an isentropic core flow with high velocities whereas the secondary zone is a low momentum, non-isentropic flow which encompasses all the losses. Both flow zones reach static pressure balance upon exit, resulting in mixed flow out as shown in Figure 5-2.

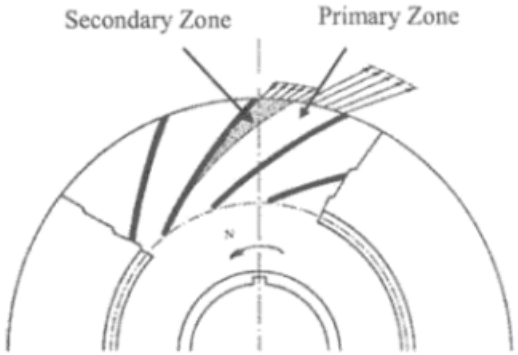

Figure 5-2: Two-zone model (Xu et al., 2010)

The two-zone model was further refined by Japikse (1985), who showed that the two-zone model provides better performance predictions as compared to the conventional single zone model. The two-zone model was completed through the addition of the variable, χ, which is the ratio of the mass flow of the secondary zone to the primary zone. The secondary zone ratio is a constant value in most two-zone models and generally lies between the values of 0.15 to 0.25 (Pelton, 2007). The assumption of a constant ratio was validated by Dean (1974), who proved that the performance prediction was not sensitive to the specified value of χ. PUMPAL™ has several two zone models available for the development of the 1D model. The models are described in Table 5-1 (Concepts NREC, 2016b):

Table 5-1: PUMPAL™ two zone models

Two-zone model	**Description**
User specified rotor efficiency	This is a simple single zone model which utilises Reynolds number in the calculations. This leads to non-realistic results
Frozen	Uses mass fraction of secondary flow to determine secondary zone parameters
Variable	Preliminary model, not suitable for industrial use
Msec/M (specific speed)	Uses specific speed to determine secondary flow mass fraction and data
Msec/M new correlation	Research model
NREC	Single zone model, not suitable for design use
Pelton-Japikse	Research model

In this work, the *Msec/M* model based on specific speed was preliminarily used in the PUMPAL™ design, as the secondary zone mass fraction was calculated iteratively in the PUMPAL™ code based upon the specific speed of the pump. The model was previously used successfully by Smyth (2014) in his analysis of the RP-1 impeller. However, the use of the model resulted in convergence failures of the solver as the specific speed was out of range of the empirical data. The frozen two-zone model was then employed with a user specified secondary zone ratio of 0.2 as recommended (Japikse et al., 1997; Concepts NREC, 2016b). This model was used successfully by Strain (2008) in the design of the DEAN oxidiser pump.

5.3.1.2 Diffusion

The diffusion process relates to the increase in static head through the impeller passage. To model this process in a 1D design space, the impeller passage is considered as a rotating diffuser and is split into two elements. The first element occurs between the inlet portion of the blades and the 'throat' of the impeller passage. The first element can function as either a nozzle or diffuser depending on the flow rate and the angle of incidence (Japikse et al., 1997). The second element extends from the 'throat' to the exit of the impeller and typically acts as a diffuser. This method is encompassed in the Two Elements In Series (TEIS) model utilised in PUMPAL™ and Figure 5-3 shows the model being applied to an impellers.

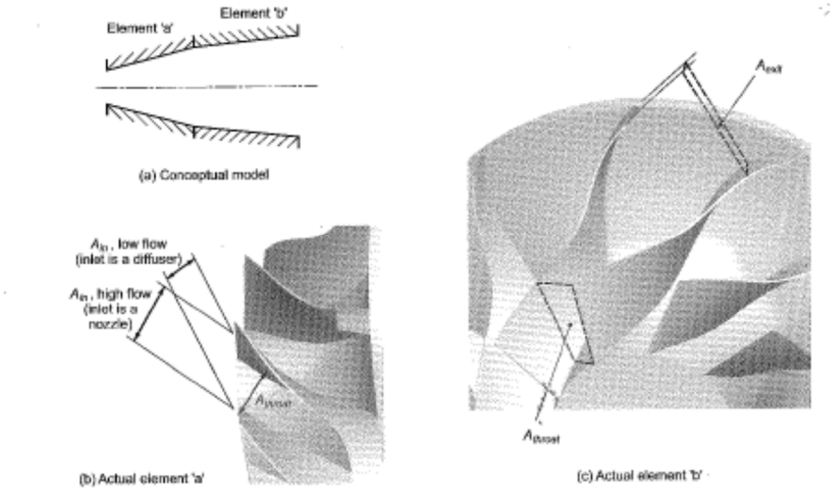

Figure 5-3: Two Elements in Series (TEIS) model (Japikse et al., 1997)

To relate the TEIS model to the impeller exit, the diffusion through the second element is calculated using the diffusion ratio (DR_2), which is the ratio of the relative velocity at the inlet tip (w_{1t}) and the exit primary zone (w_{2p}).

$$DR_2 = \frac{w_{1t}}{w_{2p}} \qquad [5.1]$$

where $DR_2 < 1$ indicates net acceleration through the impeller passage and $DR_2 > 1$ indicates net diffusion though the impeller passage.

Rodgers (1978) deduced that a relatively high diffusion factor, while advantageous, can be linked to impeller stall and that typical impellers have a diffusion relative velocity ratio limit ranging from 1.5 – 1.7. For PUMPAL™, Japikse et al. (1997) recommends values of DR_2 between 1.1 to 1.4 for impellers with diameters less than 101.6 mm for the TEIS model.

5.3.1.3 Blade tip clearance

The blade tip clearance is an important design factor that affects both the efficiency and the cost of the pump and there are three major flow phenomena losses associated with it. These are, 1) the secondary flows that occur due to pressure gradients across the flow passages, 2) the leakage flow past the tip clearance and 3) the boundary layer scraping effect, that occurs between the flow boundary layer and the blades. These effects are shown in Figure 5-4 (Hoshide and Nielsen, 1973).

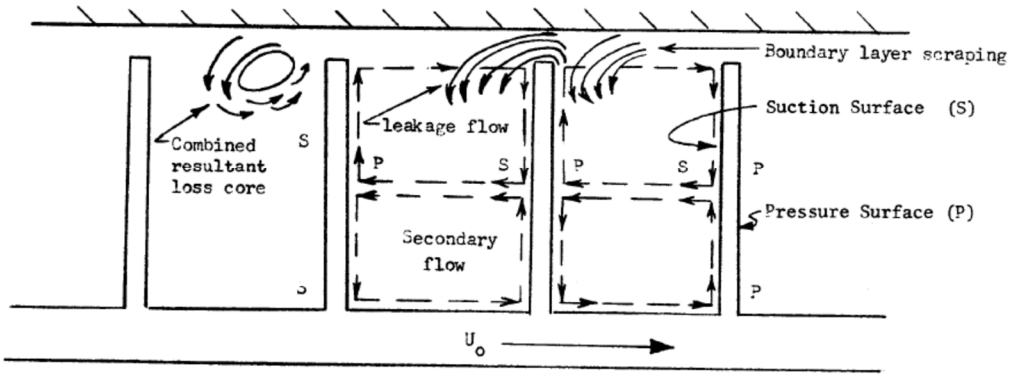

Figure 5-4: Tip clearance flow losses (Hoshide and Nielsen, 1973)

Independent studies on the effects of blade tip clearance (t_{cler}) performed by Wood et al. (1965) and Hoshide and Nielsen (1972), determine a suitable range of blade tip clearance to exit blade height ratios. These are:

$$0.01 \leq \frac{t_{cler}}{b_2} \leq 0.1 \qquad [5.2]$$

A value of 0.07 is commonly used in most pump configurations, but a smaller tip clearance is desired as this will allow for a greater efficiency to be obtained for the unshrouded pump design (Wood et al., 1965). However, oxidiser pumps do require a larger clearance in order to avoid

rubbing effects between components which can result in explosions (Furst, 1973). A conservative ratio of 0.1 was chosen for the present design.

5.3.1.4 Impeller tip width model

Stepanoff's capacity constant (*km2*) correlation is one of the models available in PUMPAL™ to determine the tip width of the impeller exit. The model makes use of design charts and empirical data to determine the impeller tip width and meridional velocities. The design chart is developed using experimental values of *km2* that are plotted against values of specific speed (Stepanoff, 1949). This leads to the constraint of one specific speed value for every design. This adds consistency of design but hinders design flexibility.

The second option for impeller tip width design, is the specification of the exit swirl parameter, λ. This is the ratio of the tangential exit velocity (c_{u2}) to the meridional velocity (c_{m2}) at exit. The value of the exit swirl is important as it directly sets the relationship in the velocity triangle at exit, hence directly affecting the exit width value. The stability of the outlet flow is also affected by the exit width design. Very high exit swirl ratios increase the width at exit but lead to unstable outlet flows and can affect the diffusion performance through the pump. Figure 5-5 is an experienced-based guide for exit swirl ratio based upon the specific speed of the pump. Using the specific speed derived from the analytical calculations, a range of values are provided that can be utilised in PUMPAL™. Figure 5-5 uses specific speed in terms of United States (US) units. A dimensionless specific speed of 0.3 corresponds to a US specific speed of 785.76.

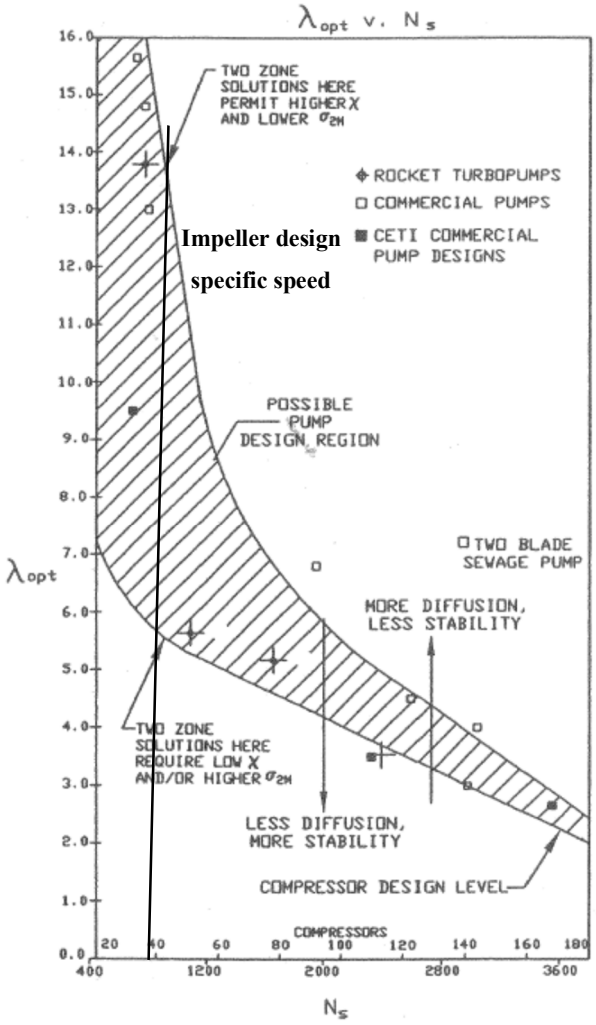

Figure 5-5: Experienced based model for exit swirl (Japikse et al., 1997)

5.3.1.5 Disk friction model

Disk friction accounts for a high proportion of the total loss in a radial pump, heavily affecting the overall efficiency of the machine. Disk friction is caused through the contact between the fluid flow in the impeller gap and the casing wall as shown in Figure 5-6 (Mikhail, 2001). This includes disk friction torque, power loss, heat transfer related to the circulation of flow and secondary flows that are induced by enclosed rotating elements. Induced flows are dependent upon element geometry as well as the enclosure of the element. Daily and Nece (1960) were among the first to investigate the relationship between the geometry of the disk and the disk friction losses. They performed extensive tests, using elements of varying geometries and at differing speeds, by taking disk friction torque measurements in the liquid filled spaces surrounding the disk. These tests formed the basis for the empirical relationship used by PUMPAL™ in the Daily and Nece disk friction model. Equation 5.3 and Equation 5.4 are used to determine the disk friction loss (Concepts NREC, 2016b).

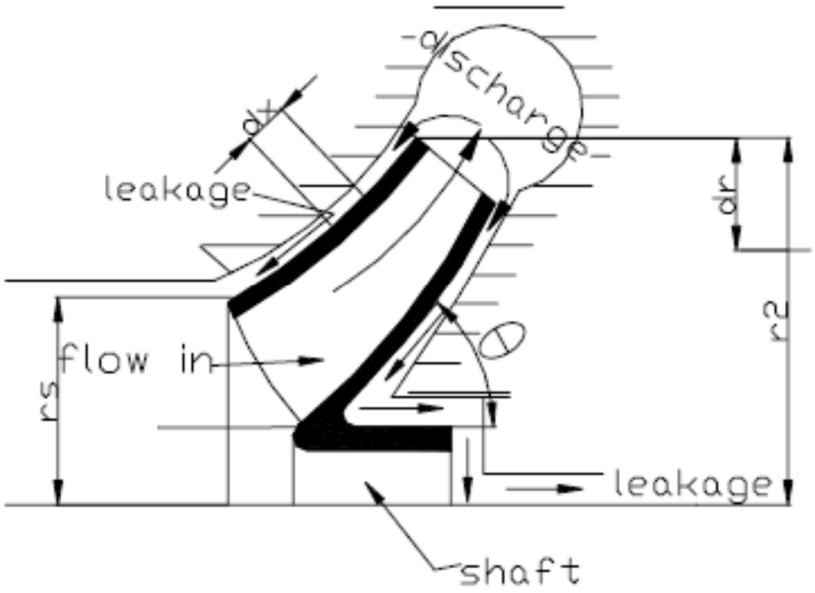

Figure 5-6: Disk friction loss in centrifugal pumps (Mikhail et al., 2001)

$$P_{df} = \frac{1}{2} k {u_2}^3 {r_2}^2 \quad [5.3]$$

$$k = \frac{0.0402}{Re^{\frac{1}{5}}} \quad [5.4]$$

where P_{df} is the power loss due to disk friction in [W], k is the disk friction coefficient and Re is the Reynolds number of the flow through the pump.

5.3.1.6 Slip

Slip is the deviation of the flow at the impeller exit that results in a change of the angle at which the flow leaves the impeller as compared to the ideal case. This results in the decrease of theoretical value, determined by Euler's turbomachinery equation, of tangential velocity, subsequently reducing the efficiency of the pump (Hawash et al., 2015). PUMPAL™ contains several models that can be used to determine the slip factor and the slip at impeller exit, with each model having its unique strengths and weaknesses.

This work uses the slip factor correlations, developed by Busemann in 1928 and adapted by Wiesner in 1967, known as the Wiesner-Busemann model. The model is commonly used in impeller design and is generally the most accurate slip factor correlation with results typically within ±5% of experimental values (Wiesner, 1967).

5.3.2 Results of PUMPAL™ analysis

The PUMPAL™ analysis is based upon the analytical design and the flow models discussed in Section 5.3.1. The PUMPAL™ analysis was split into two sections focussing on the suction performance of the impeller at inlet and the flow at exit. National Institute of Standards and Technology (NIST) data tables for liquid oxygen are included in PUMPAL™ and all properties for the analysis were derived from them. The NIST data tables were formed from the same analyses that provided the data included in Section 2.2.

5.3.2.1 Inlet suction performance

The inlet duct upstream of the impeller affects the suction performance of the inlet eye. PUMPAL™ provides several inlet duct profiles each with corresponding factors that affect the flow at inlet, improving the accuracy of the analysis. The inlet blockage factor (*BLK1*) account for the aerodynamic blockage that occurs at the impeller inlet. This is caused by the boundary layers on the inlet walls causing local flow acceleration. The ratio of the tip to mean meridional velocity (*AK*) determines the velocity distribution at inlet. This is used to determine the optimal radial curvature of the blade passage. Lastly, the inlet loss coefficient (*LC1*) is used to determine the total pressure loss in the inlet duct. These parameters were set in order to match the values set for high performance inlets described by Japikse et al. (1997) and in the PUMPAL™ design guide: *BLK1* = 0.02; *AK* = 1.03 and *LC1* = 0.01 (Concepts NREC, 2016b).

PUMPAL™ utilises two regimes to optimise the inlet tip radius. Either the tip radius can be optimised to output the minimum tip relative velocity, which corresponds to the maximum efficiency, or the impeller eye can be optimised to minimise the Net Positive Suction Head required (NPSHr) of the impeller based upon a corresponding hub radius and blade cavitation coefficient as cavitation is likely to be the limiting design parameter. Since the impeller operates at high speed, the optimisation scheme which minimises the NPSHr was chosen for this study. Using analysis mode, the hub radius was varied as to compare the suction performance of the inlet. The results are shown in Table 5-2.

Table 5-2: Hub radii performance

Hub radius [mm]	NPSHr [m]	Hub-to-tip ratio [-]	Efficiency [%]
10	13.74	0.56	83.8
12.5	15.55	0.65	83.2
15	17.77	0.72	82.4

A final hub radius of 10 mm was used, as it provides the best overall suction performance at inlet, at the highest efficiency.

5.3.2.2 Outlet specification

PUMPAL™ determines the outlet geometry of the impeller based upon the selected flow models (specified in Section 5.3.1) and the user specified operating conditions of the pump. For this work, PUMPAL™ was designated to calculate the minimum exit radius (r_2) for the specified head rise and the exit width (b_2) depending on the exit swirl. The exit radius is dependent on the speed and the required head rise. The higher the speed of the pump, the smaller the exit radius. This relationship is beneficial for a rocket electro-pump as it allows the design of a compact, light-weight unit. This relationship is displayed in Figure 5-7a and b. However, the impeller speed is limited by the inlet design to avoid excess cavitation. A final impeller speed of 23000 rpm was used in the PUMPAL™ analysis as a compromise between efficiency and cavitation prevention.

Different blade angles were studied in PUMPAL™, to improve the efficiency and hydraulic performance of the pump. Bacharoudis et al. (2008) showed that at a constant speed, the head rise of the pump increases with increasing blade angle with the trade-off being that the efficiency of the pump decreases, past the point of maximum efficiency, as the angle is increased. For this work, the effects of the blade angle at the design point speed on the head rise were investigated. The blade angle was varied from 10° to 45° and Figure 5-8 displays the results.

The head rise shows a sharp increase in (a) from 10° to approximately 20°, whereafter a steady increase is observed. Stepanoff (1949) recommends a value of 22.5° as the angle for the best efficiency at impeller exit. The final design uses the exit blade angle of 22.5° as an appropriate compromise between efficiency and head rise.

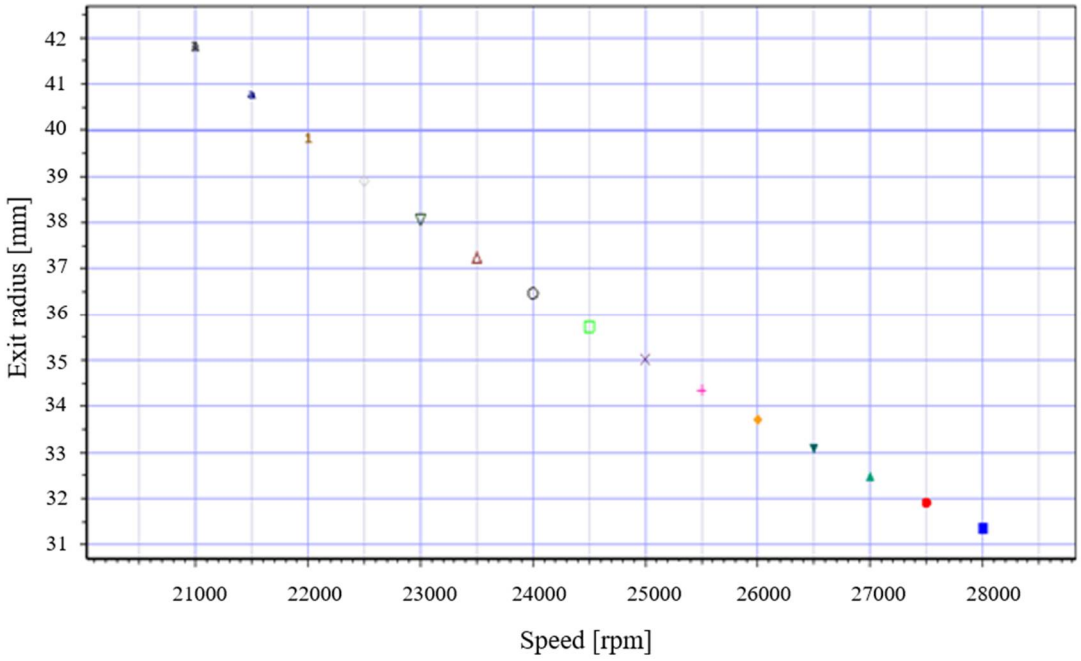

(a)

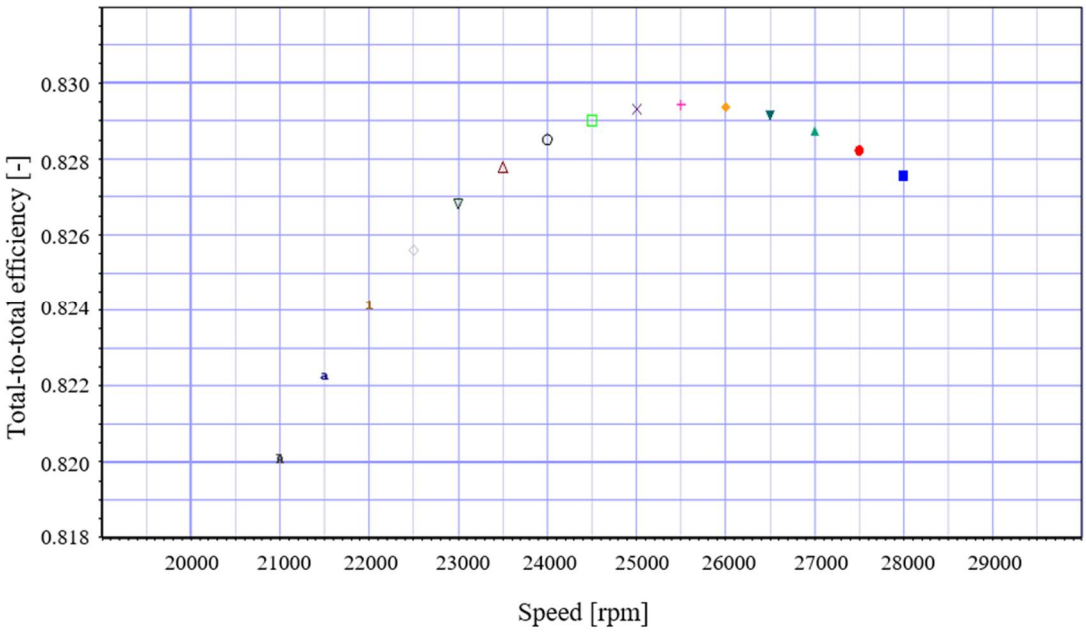

(b)

Figure 5-7: (a) The impact of speed on impeller exit radius (b) Total-to-total efficiency of impeller at different speeds for different values of r_2 at a constant head rise

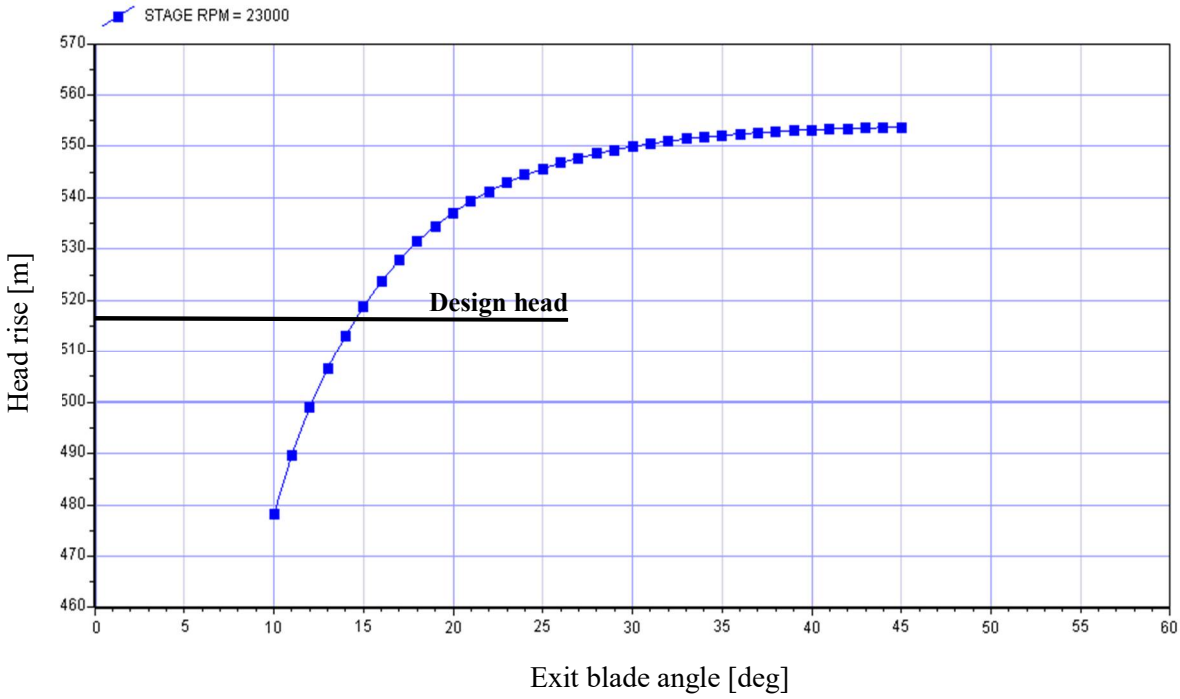

Figure 5-8: Effect of exit blade angle (β_2) on the outlet dynamic head rise of the impeller at a fixed speed

The design methodology employed by PUMPAL™ uses the dimensionless exit swirl parameter (λ) to determine the size of the exit width (b_2) of the impeller by controlling the flow angle. Since the exit swirl parameter affects the outlet area, it plays a role in controlling the diffusion through the passage. Hence, the exit swirl parameter is required to be controlled such that stalled flow is avoided. Figure 5-5 provides a range of acceptable exit swirl values that can be utilised in PUMPAL™. The swirl parameter is varied from 6 to 14, and the effect on the efficiency, diffusion ratio and the value of b_2 is investigated. The results of the investigation are shown in Figure 5-9. An exit width of 4 mm was chosen, corresponding to an exit swirl ratio of 12.5. The ratio falls within acceptable design range guidelines, and the approximate 4 mm outlet width allows for increased diffusion through the impeller passage. The diffusion ratio of 1.29 falls within the acceptable limit mentioned previously in Section 5.3.1.2.

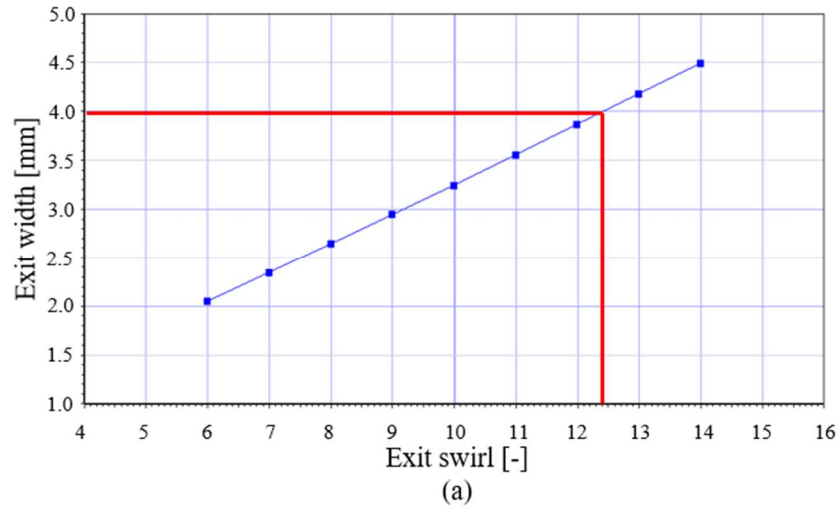

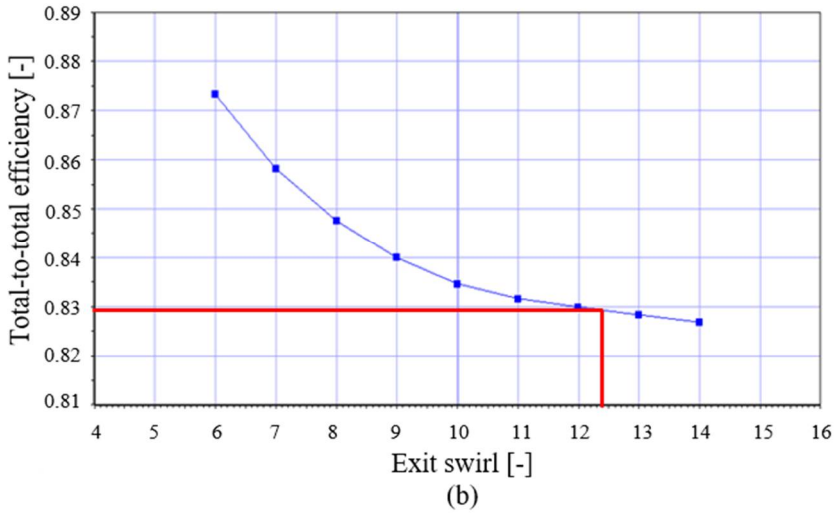

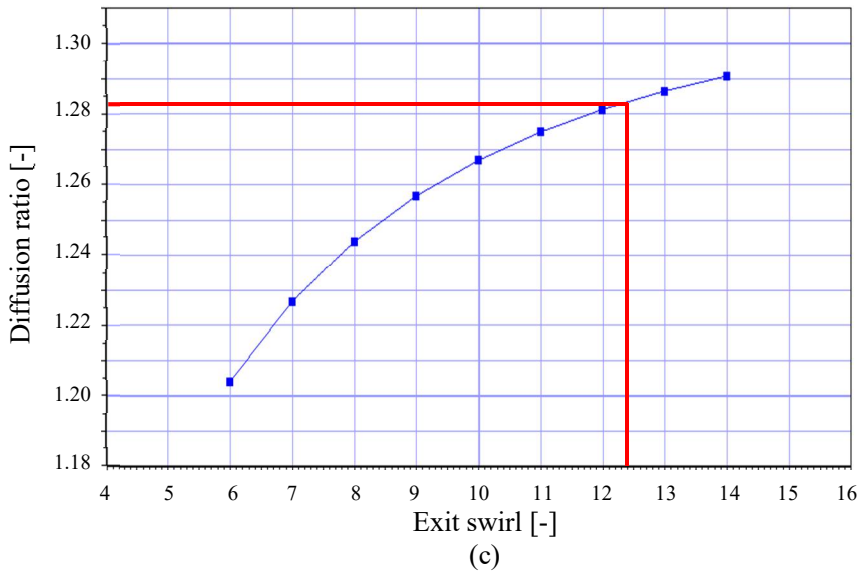

Figure 5-9: Impeller exit swirl study (a) Effect of swirl on exit width (b) Effect of swirl on Total-to-total efficiency (c) Effect b of swirl on diffusion ratio

A summary of the preliminary PUMPAL™ analysis is shown in Table 5-3. The full PUMPAL™ output is given in Appendix B.

Table 5-3: Summary of PUMPAL™ design

Impeller inlet	
Tip radius [mm]	18.04
Blade angle [°]	11.97
Impeller outlet	
Exit radius [mm]	37.39
Exit width [mm]	4.23
Blade angle [°]	22.5
Exit swirl [-]	12.5
Specific speed [dimensionless]	0.288
Static head rise [m]	513.82
Rotational speed [rpm]	23000
Total-to-total efficiency [%]	83.1

PUMPAL™'s analysis mode is used to determine the off-design performance of the pump. Figure 5-10 is the specified pump curve of the mean-line design for the oxidiser impeller.

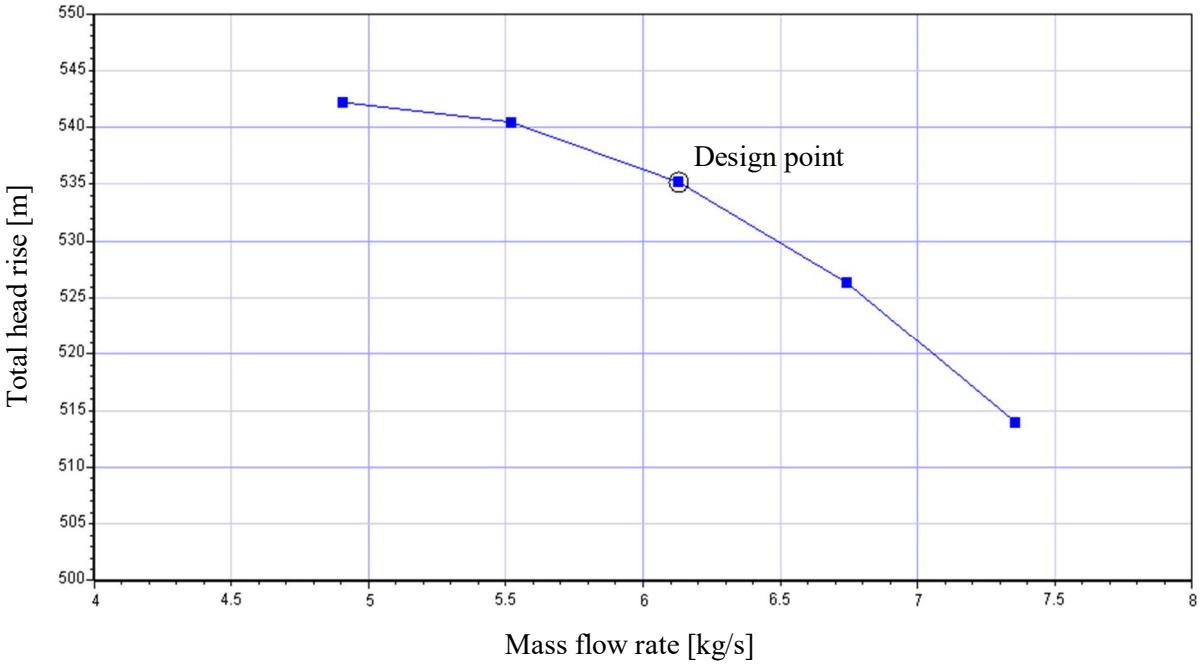

Figure 5-10: Oxidiser impeller pump curve

5.3.3 MST analysis

The Multiple Stream-Tubes or MST solver resolves the flow by dividing it into several stream tubes in the hub-to-shroud direction. This allows for a more detailed analysis using streamline curvature calculations in the hub-to-shroud direction than the conventional mean-line solver in PUMPAL™. The mass flow through the impeller is equally distributed by the number of stream tubes, and the algorithm attempts to locate the boundaries of the stream tubes and solve the flow conditions throughout the stream tubes. MST calculates the flow field along the stream tube by moving from quasi-orthogonal to quasi-orthogonal. Quasi-orthogonals are straight lines drawn across the flow passage (from the hub to the shroud) that are usually normal to the streamlines. This method discretises the impeller passage and allows for refined analysis of the through-blade flow (Concepts NREC, 2016a). The location of the quasi-orthogonals used in the final MST analysis is shown in Figure 5-11.

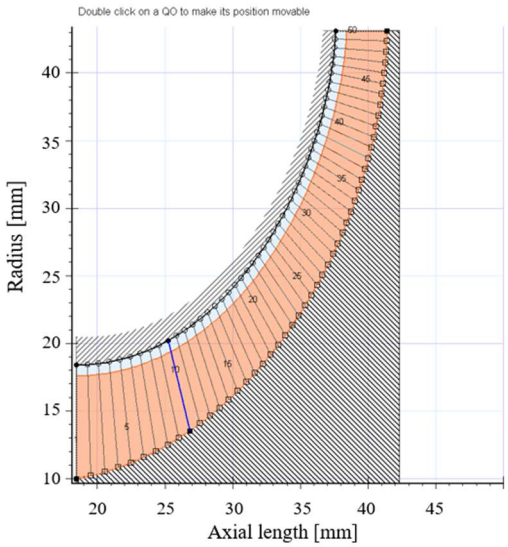

Figure 5-11: Location of quasi-orthogonals for MST analysis

The MST solver performs the following tasks when attempting a solution (Concepts NREC, 2016a):

1. Estimate the position of the stream tubes based upon a user entered number (default is 11 stream tubes)
2. Determine geometric properties of stream tubes (areas, blade angles)
3. Calculate flow field based on geometry from 2
4. Use flow field to determine location of equal mass flow stream tubes
5. Determine if solution convergence has been reached, if not the solver returns to 2.

Due to the estimation of the initial location of the stream tubes, the MST solver is an iterative process. The number of iterations required by the solver varies depends on the complexity of the solution, with average solutions requiring 15 or fewer iterations. The final convergence graph for the oxidiser impeller MST analysis is shown in Figure 5-12.

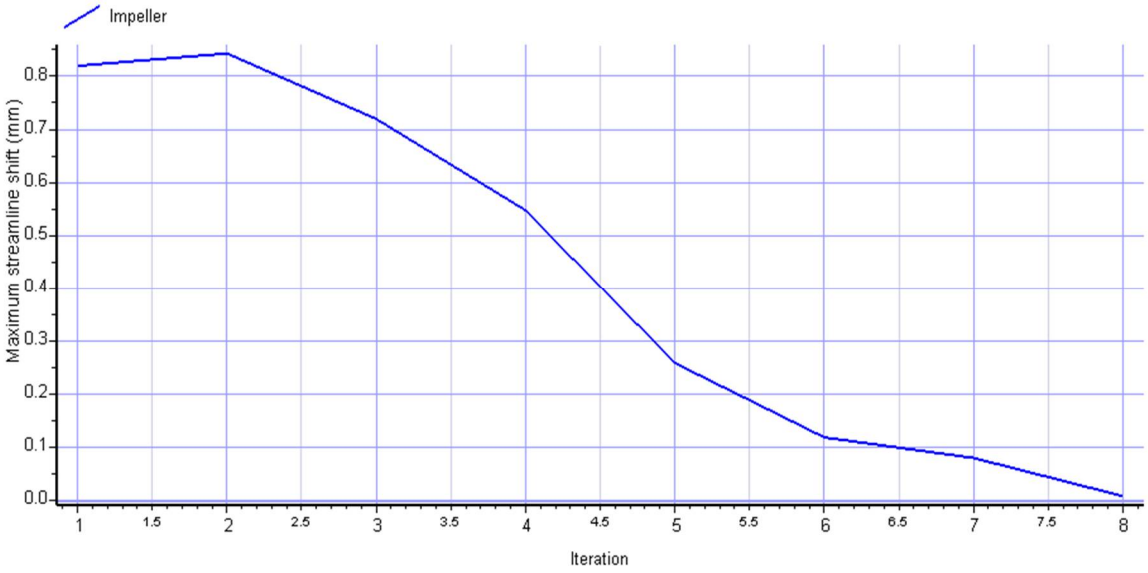

Figure 5-12: MST solver convergence

AxCent™ requires the fluid data for liquid oxygen to be manually entered as the data properties were built-in to the software as in PUMPAL™. The software utilised the parameters in Table 5-4 to determine the state of the flow through the impeller.

Table 5-4: AxCent™ fluid properties

Parameter	**Value**
Density [kg/m^3]	1190.98
Dynamic viscosity [Pa.s]	2.1988 x 10^{-7}
Speed of sound [m/s]	988.46
Specific heat capacity [J/kg.K]	1608.7
Temperature [K]	80
Pressure [bar]	3

The MST analysis was used to characterise the streamline curvature of the impeller and to determine the appropriate blading requirements. The analysis also provides more realistic flow conditions and performance than the mean-line design.

5.3.3.1 Blade number and design

The number of blades at both the impeller inlet and exit has significant effect on the performance of the pump and the development of the flow. The blading at outlet, if properly specified, can aid in the reduction of pressure pulsations and hence reduce excitation forces at exit. Furthermore, the number of blades is required to be in an optimum range such that the hydrodynamic blade loading is not too low or high. Blade-to-blade loading ($B - B$) is the distribution of relative velocities and pressure along the surface of the blade and is defined by Equation 5.5, where w_s is the relative velocity at suction side of the blade in [m/s] and w_p is the relative velocity at the pressure side of the blade in [m/s]. Low blade loading can result in high friction losses whereas a high loading creates turbulent dissipation losses due to the uneven flow field (Furst, 1973; Gulich, 2014).

$$B - B = \frac{(w_s - w_p)}{\left(\frac{w_s + w_p}{2}\right)} \qquad [5.5]$$

Gulich (2014) and Furst (1973) recommend a blade number of 5 – 8. Fewer than 5 blades are not recommended as the outlet flow will become non-uniform due to the large spaces between the blades leading to pressure pulsations and vibrations. Blade numbers higher than 8 cause instability with the *Q-H* curve since increasing the aerodynamic blockage at the inlet decreases the suction performance at inlet (Gulich, 2014).

The first design iteration utilised an impeller of 5 inlet and outlet blades as shown in Figure 5-13a. The MST analysis showed relatively high blade loading at the exit of the impeller peaking above 1.3 indicated by the yellow and red region in Figure 5-13b. This is well above the recommended threshold of 0.7 prescribed by Japikse et al. (1997), indicating excess diffusion at outlet which may lead to adverse effects such as impeller stall and excess secondary losses in the blade passages. Furthermore, the large passage areas at exit may promote recirculation in the passages.

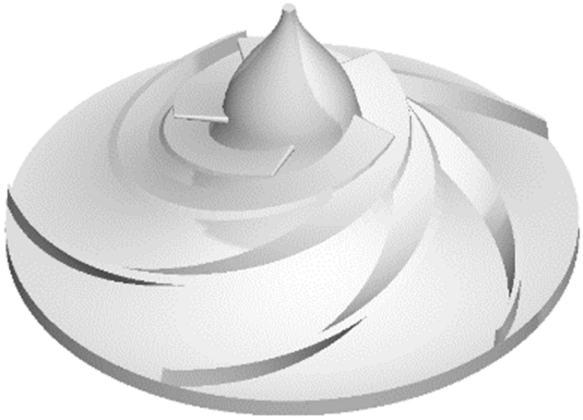

(a)

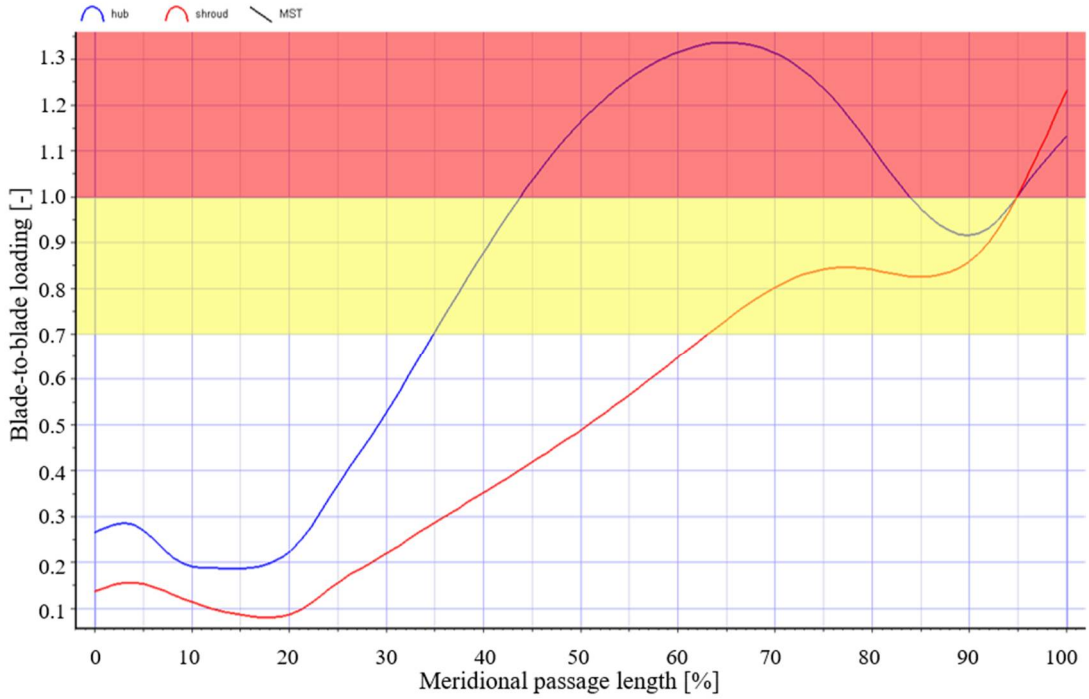

(b)

Figure 5-13: 5 blade impeller configuration (a) 3D model of 5 blade impeller (b) Blade-to-blade loading for 5 blades across the meridional plane

A configuration of 8 blades (Figure 5-14a) was tested as an attempt to solve the high blade loading at exit by increasing the solidity. Figure 5-14b is the blade loading graph for the 8-blade impeller arrangement. The 8-bladed impeller showed excellent loading characteristics as shown in Figure 5-14b but at a significant performance cost, delivering flow at a total pressure of 29.5 bar and an efficiency of 49.3%. The blockage at inlet was attributed to the performance deficit due to the

high blade number. The high blockage would have resulted in increased local acceleration and static pressure drops causing excess cavitation at inlet.

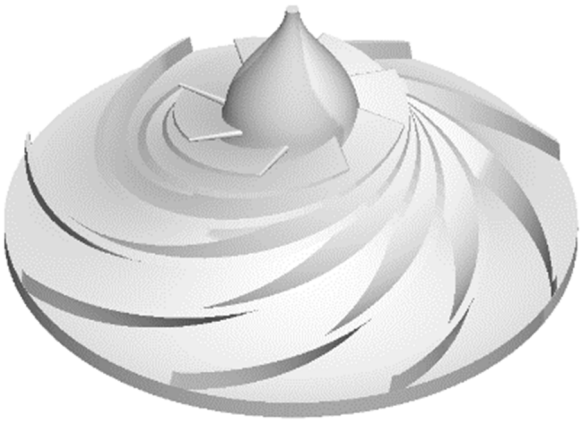

(a)

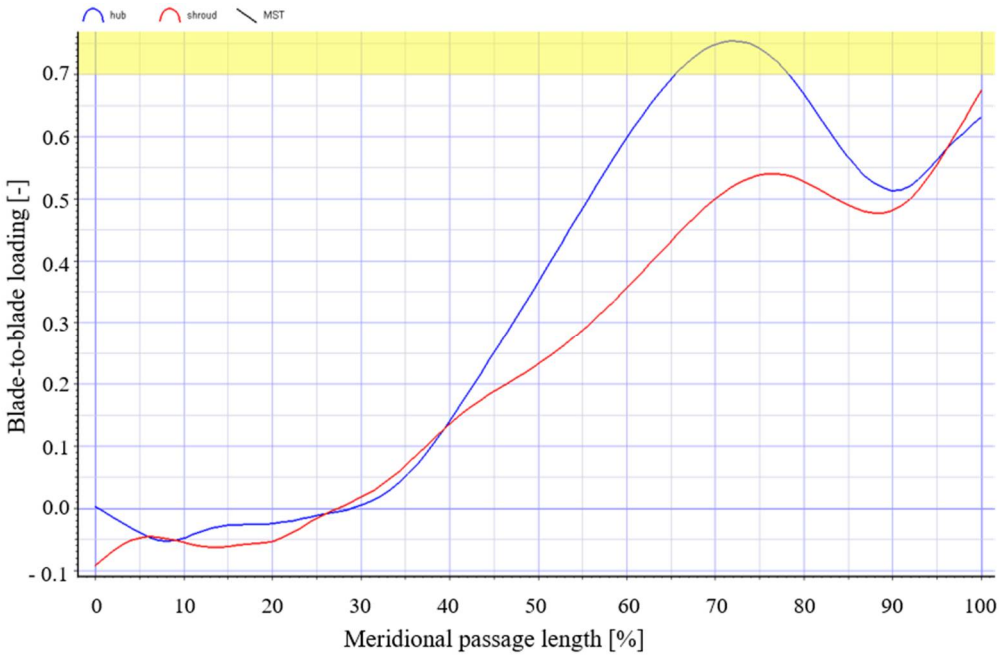

(b)

Figure 5-14: 8 blade impeller configuration (a) 3D model of 8 blade impeller (b) Blade-to-blade loading for 8 blades across the meridional plane

The use of splitter blades in the oxidiser impeller was investigated to improve the blockage at inlet. Splitter blades (running from 30% blade position to 100%) reduce the blade blockage at inlet resulting in increased hydraulic performances, reduced pressure fluctuations and extended operational range (Kergourlay et al., 2007). The reduced blockage at inlet improves the suction performance of the pump, reducing the impact of cavitation. Pavesi et al. (2014) performed a CFD

analysis showing the reduction in vapour development, as a result of cavitation, at the inlet of a splitter blade impeller versus a traditional impeller. In this work, a splitter blade impeller configuration consisting of 4 inlet blades and 8 outlet blades (Figure 5-15a) was analysed. The blade-to-blade loading experienced by the splitter configuration is shown in Figure 5-15b. The splitter configuration displays improved blade loading characteristics, and is characterised by a sharp spike at the splitter inlet. The spike is immediately followed by a large drop in blade loading indicating a decrease in flow area and acceleration of the flow, which is expected at the splitter inlet.

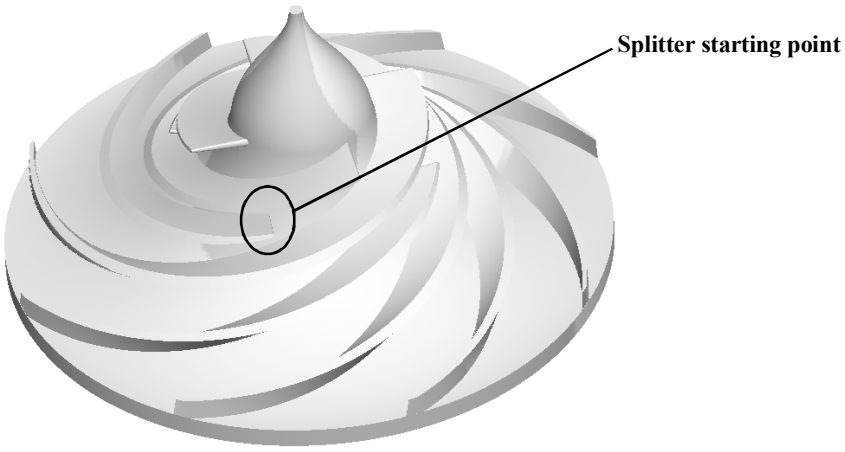

(a)

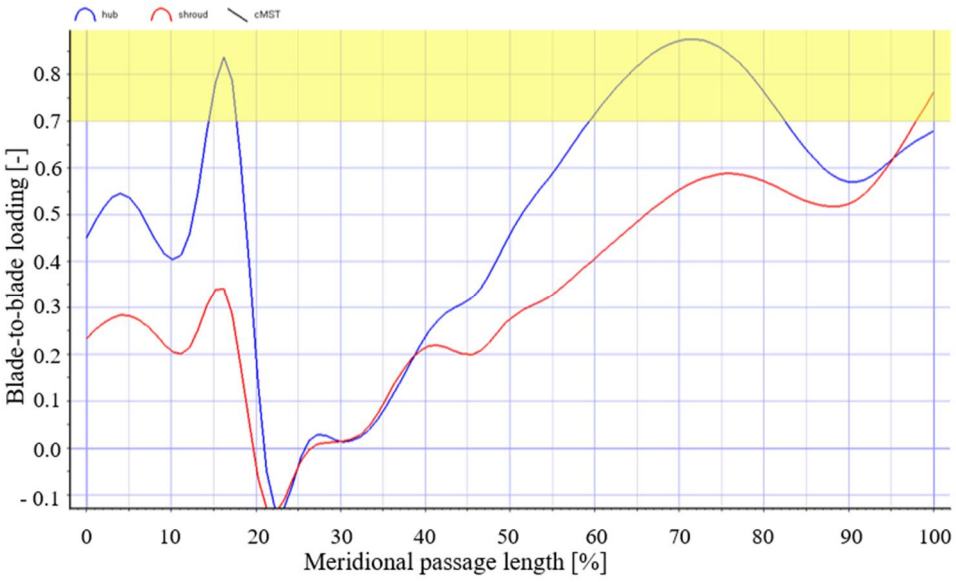

(b)

Figure 5-15: 4-8 blade impeller configuration (a) 3D model of 4-8 blade impeller (b) Blade-to-blade loading for splitter configuration across the meridional plane

A CFD analysis was performed on these configurations, using AxCent™'s built-in Pushbutton CFD™ package, to determine the efficiency and hydraulic performance of the blade arrangements. The results of the CFDs are shown in Table 5-5. The splitter configuration possesses the greatest efficiency and performance and was chosen as the final configuration for the oxidiser impeller.

Table 5-5: Summary of blade configurations

Blade arrangement	Outlet total pressure [bar]	Efficiency [%]
5	59.4	68.1
8	29.5	49.3
4 – 8	61.8	73.9

The blade thickness is dependent upon the mechanical strength requirements of the blade. Through empirical analysis, the blade nominal thickness (e) is commonly expressed as a ratio of $\frac{e}{D_2}$ with an acceptable range of 0.016 – 0.022. The upper limit of the range is generally used for high head flows (600 m+) and the lower limit for low head and specific speed. Gulich (2014) provides an empirically developed relationship for the blade thickness with respect to exit tip velocity and exit diameter. This is shown in Equation 5.6:

$$e = 0.02\left(\frac{u_2}{u_{ref}}\right)^{0.2} D_2 \qquad [5.6]$$

where u_{ref} is the reference tip velocity of 100 m/s.

The leading-edge profile of the blade is an important consideration as an unfavourable profile can lead to local excess velocities and low-pressure zones affecting cavitation behaviour and pump efficiency (Gulich, 2014). Using the standard, semi-circular profile provided by PUMPAL™, the leading-edge thickness was determined to be 0.8 mm.

The trailing edge of the blade is typically tapered to approximately half of the calculated nominal blade thickness from Equation 4.13. This will aid in reducing the width of the wake flow at exit along with the decrease in pressure pulsations and turbulent dissipation losses (Gulich, 2014).

5.3.3.2 MST results

The MST analysis was used to optimise and analyse the mean-line impeller design. The main design aspects analysed in the MST is the hydrodynamic fluid loading and the static pressure development through the impeller. Figure 5-15 showed the level of blade-to-blade loading in the final design configuration and as explained previously, the loading level was acceptable. The hub-

to-shroud loading provides an indication of the relative velocity field through the impeller. It is recommended by Japikse et al. (1997) to keep the loading value below 0.9 so as to avoid large velocity gradients that can result in high structural loading and instabilities.

Figure 5-16 shows the hub-to-shroud loading in the impeller, which is kept below 0.9 throughout as recommended. Figure 5-17 and Figure 5-18 show the static pressure development through the pump meridional section. The static plot drops into the red region (cavitation risk) of Figure 5-17 approximately where the splitter blades begin, suggesting a large low-pressure region. This is highlighted in the contour plot of the meridional flow passage, indicated by the dark blue region. These observations suggest the presence of cavitation at the pump inlet. Further analysis through full CFD software is required to determine the extent and effect of the low-pressure regions.

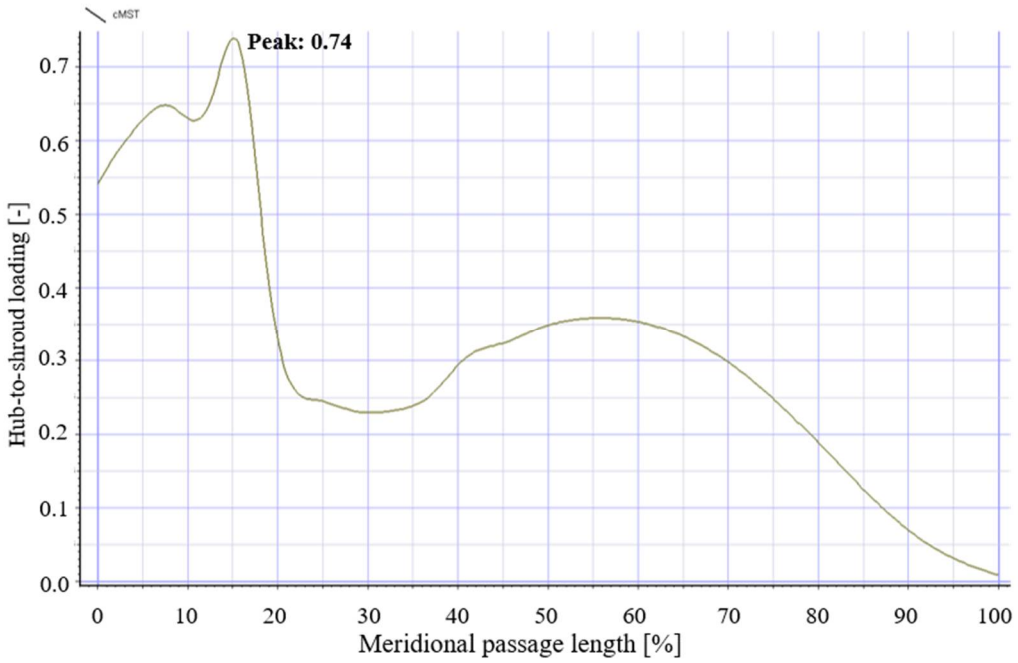

Figure 5-16: Hub-to-shroud loading across the meridional plane of the splitter impeller

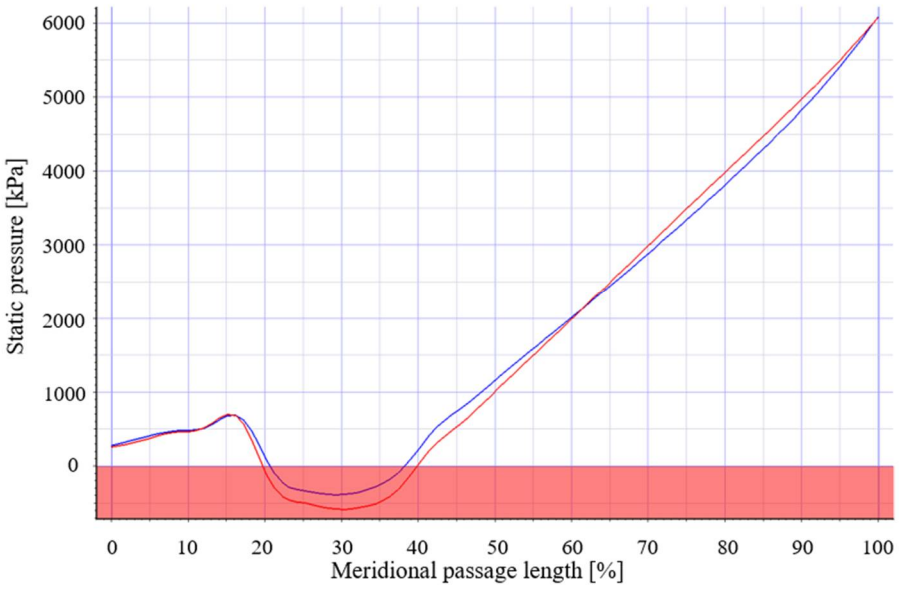

Figure 5-17: Static pressure along the length of the meridional passage of the splitter impeller

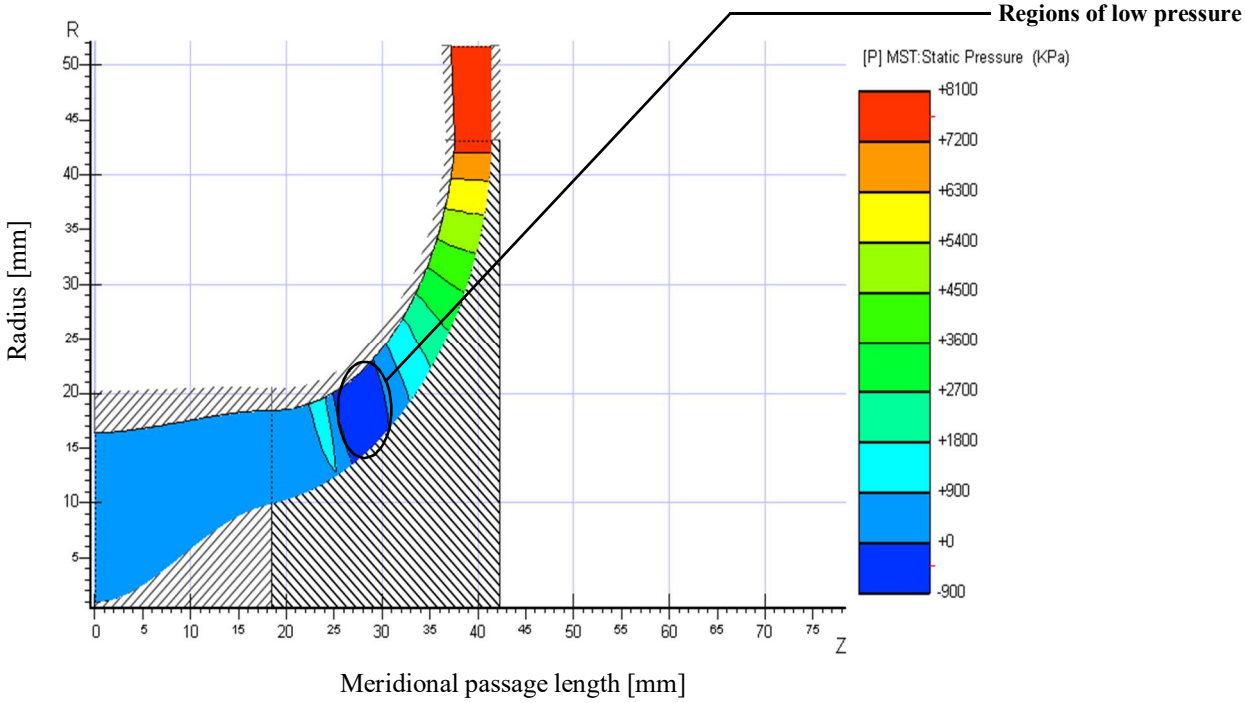

Figure 5-18: Static pressure development through the meridional plane of the splitter impeller

5.4 AxCent™ CFD analysis

AxCent™ includes a Pushbutton CFD™ capability that can perform quick CFD analyses on a design iteration. The software provides a full three-dimensional analysis of the design and incorporates a full Navier-Stokes solver. The boundary and other input conditions are carried over from the MST and mean-line analysis, with the CFD results forming the end-point of the design process. All grid meshing and solver settings are handled by the Pushbutton CFD™ program

(Concepts NREC, 2016a). CFD is useful in determining the flow conditions through the impeller and locating areas of interest such as reversed or separated flow. This section will discuss the development of the CFD grid, the computational model setup and the results of the CFD analysis.

5.4.1 Grid development and solver models

The computational domain used by the Pushbutton CFD™ program follows a single flow passage through the impeller, due to the symmetry present in the impeller design. A single flow path for the final analysis is shown in Figure 5-19. The use of symmetry reduces the computational cost of the simulation and allows for the results to be determined faster.

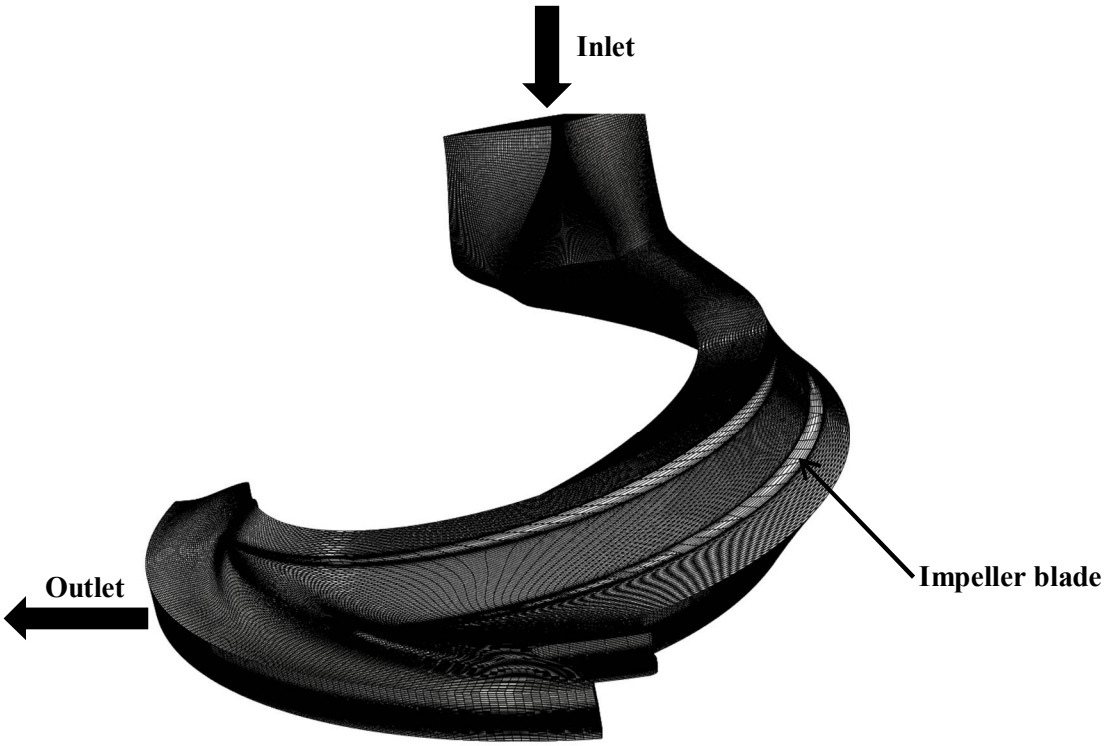

Figure 5-19: Computational flow domain

The computational domain of the model is solved numerically through the discretised representation or mesh. Three different grid element strategies may be used to mesh the computational domain. These are the O-type, C-type and H-type grids and representations of the H and O-type grid are shown in Figure 5-20. The O-type grid is the preferred grid type for axial machines and for the area in the immediate vicinity of the blade. The scheme provides significant grid improvements at blade leading edges compared to other strategies. The H-type grid is suitable for meshing regions in the flow passages as it is a classic sheared grid type. Proximity to blades and high curvatures result in skewness of the cells and high aspect ratios which result in inaccurate solutions. The C-type grid is a hybrid of the O and H type grids forming either OC or OH-C type

grids. In this scheme the O-type grid is generated around the leading and trailing edges of the blade to capture the flow accurately at these points. C-type grid variations are commonly used in radial machines and were chosen as the meshing scheme for this work (Concepts NREC, 2016a; Fitzgerald, 2016).

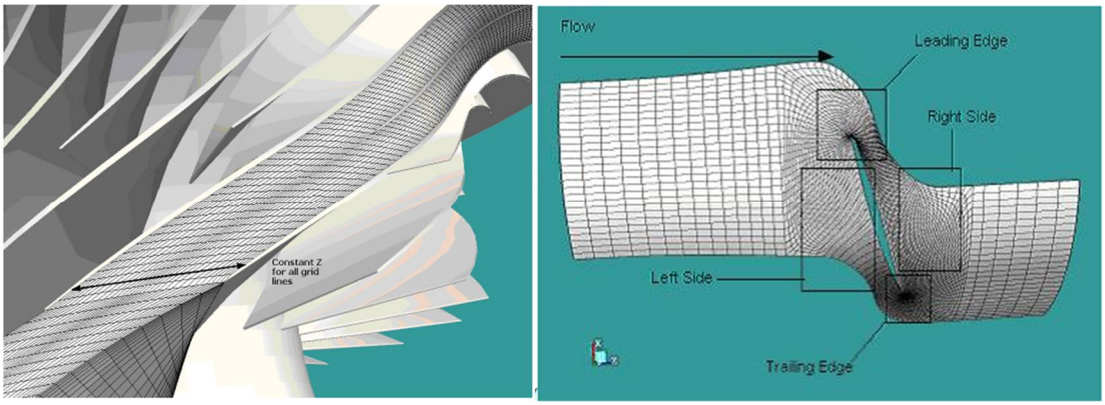

(a) (b)

Figure 5-20: Representations of the (a) H-type grid and (b) O-type grid (Concepts NREC, 2016a)

The near wall viscous effects are captured using clearance cells, that sub-divided the near wall surfaces into thin layers such that a fine grid is formed at the wall surface as illustrated in Figure 5-21. The fine grid at the wall allows for the accurate capturing of the boundary layer.

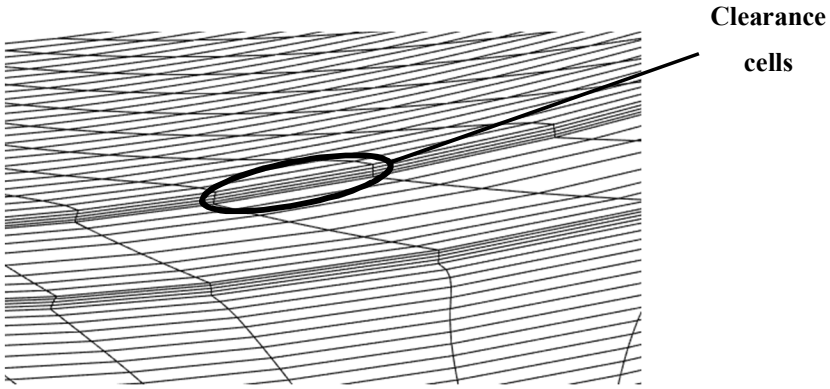

Figure 5-21: Clearance cells located at the blade surface

The number of clearance cells and the thickness of the clearance cell layer are dependent on the wall treatment and turbulence model that is utilised. The accuracy of the boundary layer can be further gauged using the dimensionless $y+$ value determined during the simulation. A low $y+$ (< 1) solution indicates the first clearance cell lies in the viscous sublayer and directly captures the viscous flow effects. AxCent Pushbutton CFD™ recommends the use of the Spalart-Allmaras turbulence model as the optimal model for the solver, which utilises the log-law wall function. The log-law wall function is valid for a high $y+$ mesh, with values ranging from 15 – 500

(Concepts NREC, 2016a). The final mesh for the CFD analysis had an average $y+$ value 85 for the blade surfaces and 358 for the hub-to-shroud region.

The number of cells in the grid influences the computational cost with respect to the solution time of the simulation. A mesh independence study was performed to ensure that mesh had no significant influence on the accuracy of the simulation along with ensuring that the simulation is not excessively time intensive for minor gains in accuracy. Five simulations were run with increasing cell counts from 500 000 to 3 500 000 cells. For the results to be compared, all settings were kept constant throughout the study. These included a clearance cell count of 8, and OH-C type mesh and all simulations were run for 500 iterations, which included 100 pre-steps. The number of cells in the mesh was controlled by varying the grid nodes in the hub-to-shroud direction and the grid nodes from blade-to-blade. The results of the mesh independence study are shown in Figure 5-22. The percentage difference in results of the fourth and fifth mesh was 0.15%. Therefore, mesh 4 was used as the best compromise between computational time and results accuracy. The final mesh consisted of 2 648 148 cells. Had the mesh utilised the full impeller computational domain instead of the slice as shown in Figure 5-19, the total number of cells would have been 10 592 592 cells.

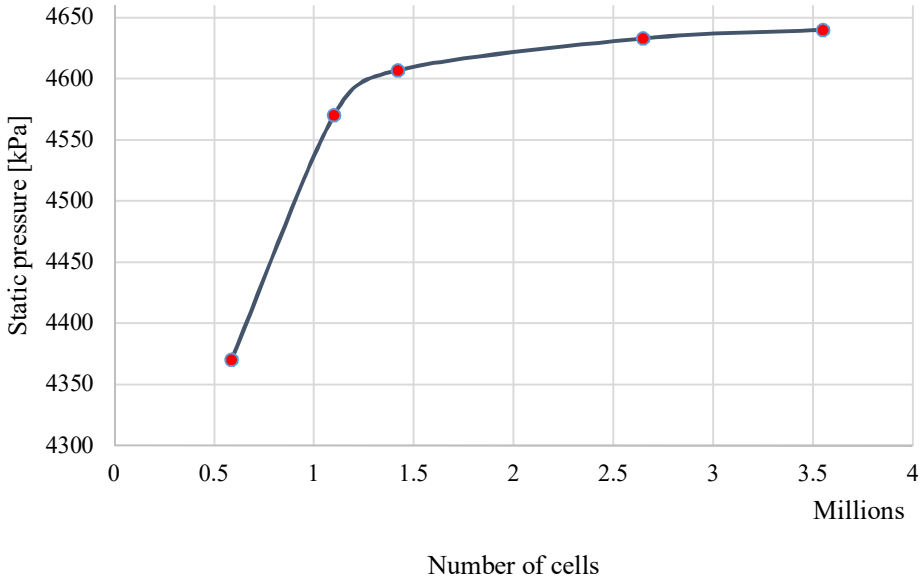

Figure 5-22: Grid independence study of the final impeller geometry

AxCent™ utilises three built-in CFD solvers, namely the Dawes solver, the Multi-block solver and the Denton solver. The Dawes solver uses the Reynolds-Averaged-Navier-Stokes (RANS) equations and only supports the H-type shear grid for meshing, which limits the size of the grid. Due to the limitations of the solver, it was not used in the CFD analysis of the oxidiser pump. The Denton solver is a research based solver and is not suitable for the analysis of radial machines.

The Multi-block solver was used for the CFD study as it can handle any number of cells in the grid and supports the full RANS equations and commercially used one- and two-equation turbulence models. Furthermore, all solution types and grid types are supported. The solver settings used to obtain the CFD solution are shown in Table 5-6.

Table 5-6: Summary of solver settings

Solver	Multi-block
Turbulence model	Spalart-Allmaras 1-equation model
Wall treatment	Log/law hub/case shear stress
Solver scheme	Implicit
Multiblock scheme	Incompressible
Pre-steps	100
Number of iterations	1000

5.4.2 CFD results

The simulation was run using the solver settings described in Section 5.4.1. The simulation ran for 1000 iterations, including 100 pre-steps. Pre-steps are used to initialise the solution by solving the simulation using a coarse grid hence decreasing computational time and aiding the convergence of the solution. The convergence of the solution is shown by the residual plot in Figure 5-23. The instability at approximately 450 iterations is believed to be caused by numerical solution errors and did not affect the results or convergence of the result.

The static pressure development through the impeller is shown in Figure 5-24. As expected, there was a large static pressure recovery in the vaneless space diffuser, increasing the static pressure to 52.4 bar. The volute was not included in the simulation as it required the full computational domain, and it was decided to analyse the performance of the volute using a more complex CFD package (Star-CCM+™).

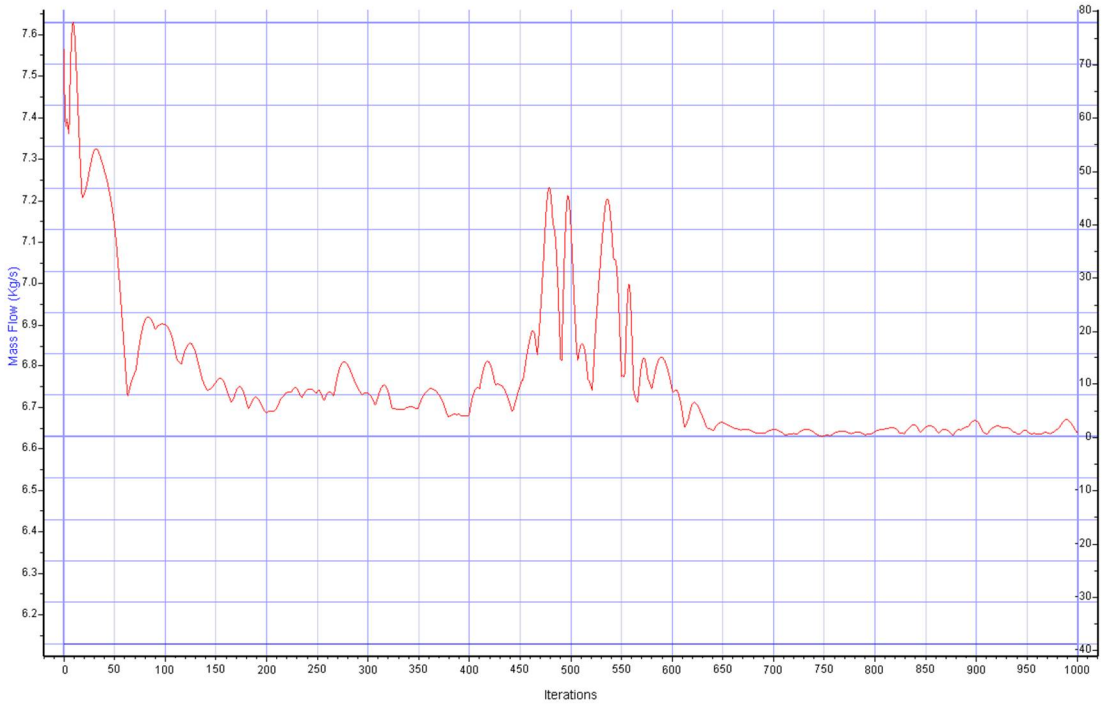

Figure 5-23: AxCent™ CFD residual plot

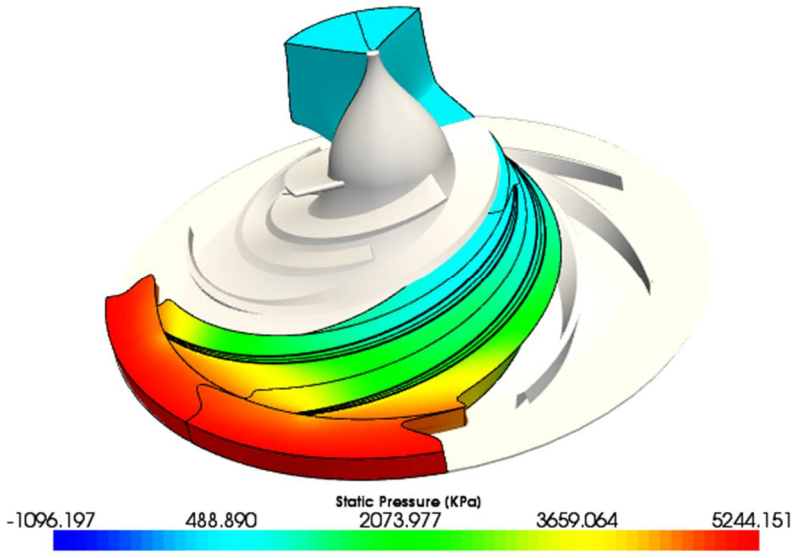

Figure 5-24: Static pressure development through impeller and vaneless diffuser

Preliminary Star-CCM+™ analyses were run to determine if the required outlet pressure was attained. Subsequent analyses determined that the impeller was not meeting the performance requirements, and a refinement of the design was required. The relationships between the head rise, speed and outlet radius were revisited and using PUMPAL™'s analysis mode and Figure 5-7a and b, the speed and outlet radius were changed and tested in AxCent™ and Star-CCM+™

until the required head rise was obtained. This resulted in a new outlet radius of 43 mm and a new rotational speed of 26000 rpm. All other geometric parameters remained the same. The reason the performance requirement could not be obtained in the first design iteration could be due to several factors. Firstly, PUMPAL™ does not include 3D flow effects in the mean-line calculations and is described as a rapid prototyping software that will produce a resultant geometry for any set of inputs. It was clear that the preliminary design's performance was overpredicted by the mean-line software and did not produce a realistic working geometry. Secondly, the design point for the oxidiser pump lies on the far left extreme of the centrifugal design pump specific speed regime (Figure 4-3), which is an uncommon design point. Therefore, there may not have been enough empirical data for PUMPAL™ to accurately determine working conditions of the pump. A pump with a better set of operating conditions, such as the impeller designed by Smyth (2014), showed results that correlate between the mean-line and CFD analysis (Richings, 2015).

The new impeller design was simulated in AxCent™ and the static pressure outlet from the vanless diffuser is shown by Figure 5-25.

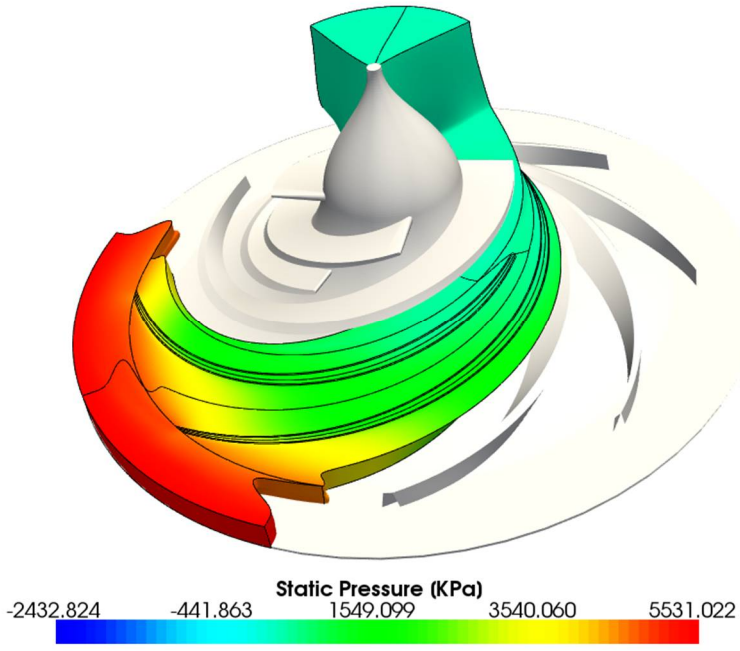

Figure 5-25: Final impeller design static pressure

Examining the leading-edge of the blades, one notices areas of low-pressure (Figure 5-26). Theoretically, these are possible indications of cavitation inception. The areas of low-pressure were further analysed in an unsteady cavitation analysis performed in Star-CCM+™.

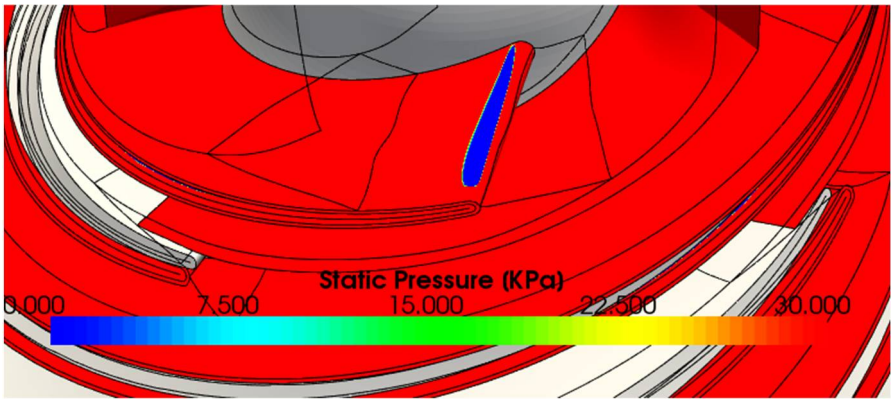

Figure 5-26: Region of low-pressure on leading-edge

5.5 Summary

The preliminary impeller design developed in PUMPAL™ and using MST solver was required to be re-designed due to it not meeting the performance requirements. The results of the CFD analysis using the re-designed impeller are given in Table 5-7.

Table 5-7: AxCent™ CFD final results

Parameter	**Final impeller design**	**Initial impeller design**
Total pressure outlet (impeller) [bar]	77.39	72.51
Static pressure outlet (impeller) [bar]	46.33	43.70
Efficiency [%]	68.7	71.4
Power [kW]	44.53	40.86
Mass flow inlet [kg/s]	6.14	6.14
Exit radius [mm]	43	37.39
Speed [rpm]	26000	23000

Chapter 6. Star CCM+™ CFD Analysis

6.1 Introduction

A more robust analysis of the low-pressure zone identified within the AxCent™ simulation flow field was warranted. This was necessary given the lack of fluid physics models to detect cavitation effects.

Two analyses were performed in Star CCM+™, namely a steady-state flow analysis and transient multiphase flow analysis. The transient analysis allows for the effect of the leading-edge cavitation to be observed. These analyses are based upon the work of Richings (2015) who dealt with the cavitation in a fuel pump impeller.

6.2 CAD preparation and computational domain

The 3D impeller geometry generated in AxCent™ consists of the hub, blades and shroud (with included tip gap) as shown in Figure 6-1. The vaneless diffuser and the volute are also included.

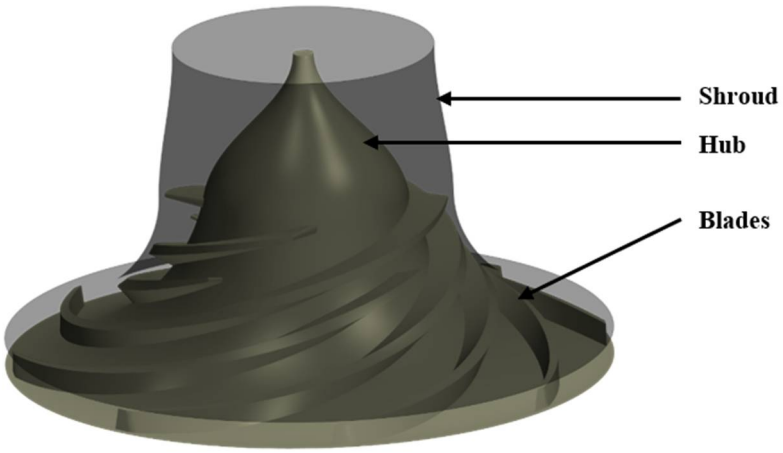

Figure 6-1: Impeller geometry including hub, shroud and blades

The computational analysis in Star-CCM+™ requires that the fluid flow through the impeller be represented as a solid fluid region with the actual impeller body being represented as open space. This essentially forms a negative of the solid impeller body. The solid fluid region was created using Autodesk Inventor and imported into Star-CCM+™. Figure 6-2 represents the computational domain for the simulation and includes the fluid regions through the impeller, vaneless diffuser and volute. The analysis requires the impeller region to be defined as rotating to simulate a working pump model. Consequently, the domain was separated into three regions: the inlet duct, the rotating impeller and the outlet region consisting of the vaneless diffuser and the volute.

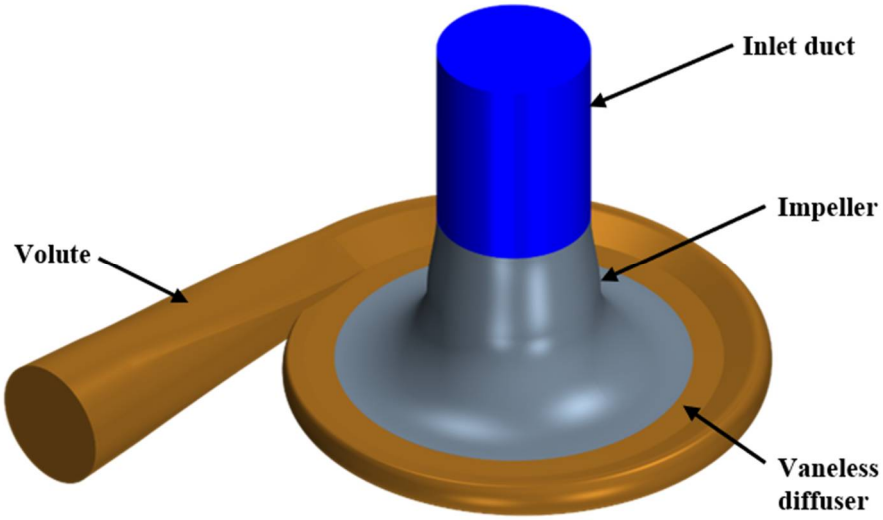

Figure 6-2: Computational domain including impeller, vaneless diffuser and volute

The inlet duct (blue) was added to the fluid region to simulate flow entering the impeller from the plumbing. Furthermore, the duct was elongated to ensure that no reversed flow would occur at the inlet surface, thereby affecting the accuracy of the solution. The impeller region (grey) is fluid in the blade passages and the tip gap clearance. This region is designated as rotating. The outlet region (bronze) consists of the vaneless diffuser and the volute fluid flow regions.

6.3 Mesh generation

The mesh is the discretised representation of the solid computational flow domain, to which physics models are applied to provide a numerical solution. Before the imported impeller geometry was meshed, the geometry surface and features were inspected and geometrical defects or 'bad CAD' were eliminated. This ensures that the surface forms a watertight outer boundary to the computational domain and mesh generation will occur (CD-Adapco, 2017).

The first step in the meshing process is the development of the surface mesh to provide the base upon which a final volume mesh is built. A dense volume mesh requires a suitably fine surface mesh. The surface remesher model was used to improve the overall quality of the imported geometry by retriangulating the surface based upon a user specified base size. A fine surface mesh allows for the curvature of the blades and hub profiles to be captured accurately (CD-Adapco, 2017). The section of the remeshed surface of the impeller is shown in Figure 6-3.

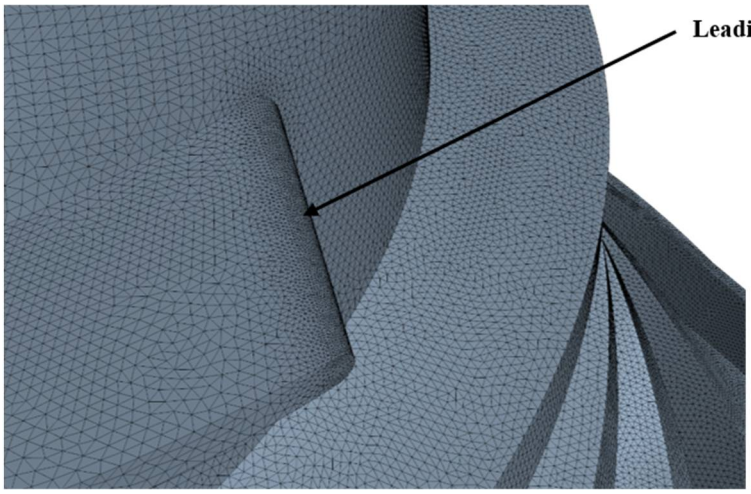

Figure 6-3: Remeshed surface showing refined curvature at leading edge

Star-CCM+™ provides several volume mesh models, each with their own unique advantage and characteristics. The tetrahedral mesher forms the core mesh using a tetrahedral cell shape based upon the triangulation of the surface mesh. The tetrahedral meshing model has the fastest per cell solution time, with the drawback that the model generates meshes with high cell counts. The polyhedral mesher utilises cells of an arbitrary polyhedral shape (averaging 14 faces) to build the core mesh. Polyhedral meshes are generally easy and efficient to generate and contain five times fewer cells than the tetrahedral mesher (CD-Adapco, 2017). These allows for faster solution times and lower computational cost. The trimmed mesher generates a core mesh using hexahedral cells with minimal cell skewness. The trimmed mesher is generally used for external aerodynamic flows and is exceptionally useful for refining the cells in the wake region of a moving body. The prism layer mesher is used in conjunction with one of the core mesh models to generate orthogonal cells at wall surfaces or boundaries. The prism layer cells improve the accuracy of the flow solution by resolving the conditions at the fluid wall accurately (CD-Adapco, 2017). This allows for the capture of various flow phenomena such separation and cavitation.

The polyhedral and prism layer model were used in this study. The polyhedral model allows for an accurate solution at a reduced computational cost and the prism layer model will aid in the accurate capture of the boundary layer. Figure 6-4 details a section of the final mesh showing the prism layers along the shroud wall and blades and the polyhedral cells in the blade passages and tip gap.

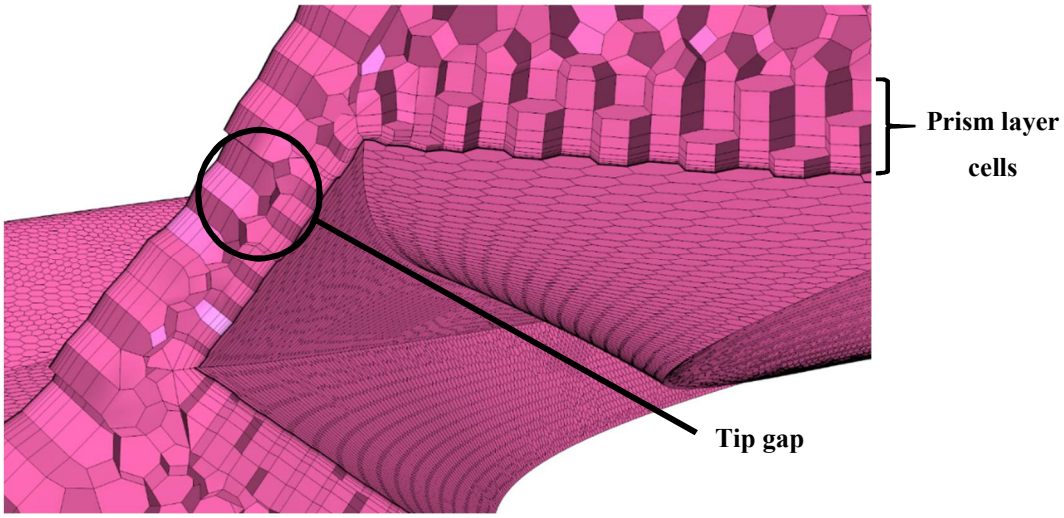

Figure 6-4: Impeller mesh showing the tip gap

Similarly to the AxCent™ CFD analysis, a mesh independence study was performed to determine the suitable cell base sizes for the impeller mesh. The mesh independence study involves reducing the base cell size, in turn increasing the cell count, until the change in the pressure outlet is negligible from one mesh to the next. This renders the solution independent from the final mesh cell count. Nine meshes were generated in total for the mesh independence study, the results of which are displayed in Table 6-1 and Figure 6-5.

Table 6-1: Mesh independence study results

Mesh	Cell count	Pressure outlet [bar]	Mass flow inlet [kg/s]	Iteration time per core [s]	Percentage difference [%]
1	100000	61.66	6.13033	2.28	N/A
2	175000	60.78	6.13005	2.82	-1.44
3	300000	60.85	6.13000	4.78	0.12
4	750000	61.28	6.12830	11.2	0.70
5	1500000	61.80	6.12783	26.3	0.84
6	3000000	61.90	6.13025	44.78	0.16
7	4500000	61.80	6.12791	69.65	-0.16
8	7000000	61.70	6.13000	110	-0.16
9	13000000	61.67	6.13032	206	-0.05

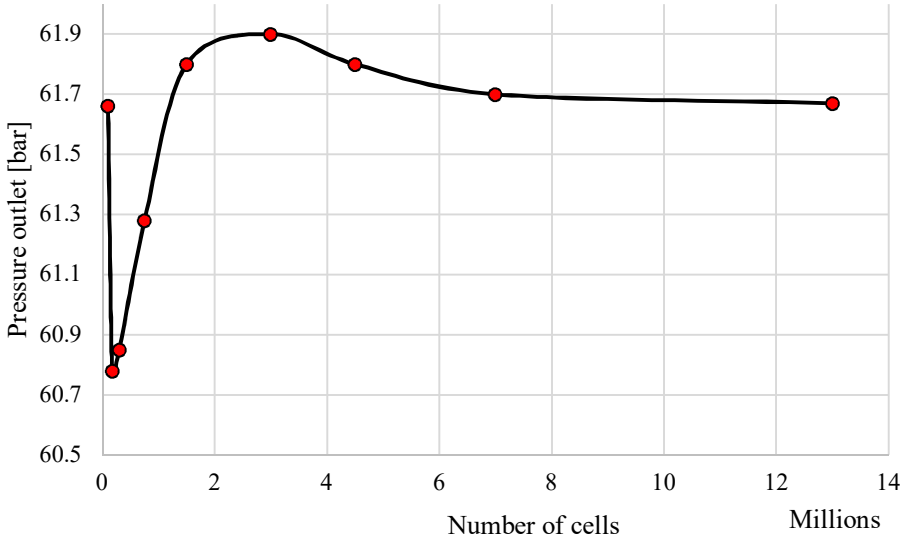

Figure 6-5: Mesh independence study relating pressure at outlet to cell count

The percentage difference from mesh 8 to 9 was -0.05%, and was deemed as an acceptable value at which the mesh can be assumed to have no impact on the outcome of the results of the simulation. This corresponded to a mesh base size of 1 mm.

The prism layer mesh model is used to resolve the flow conditions at the wall. The thickness and number of prism layers used determine the dimensionless $y+$ value at the wall surfaces and in turn dictates the wall treatment model that is used. For this work, a low $y+$ regime was utilised to properly resolve the viscous sublayer. To achieve a $y+$ of below 1, the distance to the first cell centroid (y) was calculated and manually controlled. The process to determine the correct first cell required the wall shear stress (τ_w) which was determined through steady-state simulations. Using Equation 6.1 and the average wall shear stress, the shear stress velocity, u^*, was calculated.

$$u^* = \sqrt{\frac{\tau_w}{\rho}} \qquad [6.1]$$

This allowed the size of the first cell to be calculated using Equation 6.2.

$$y^+ = \frac{u^* y}{\upsilon} \qquad [6.2]$$

where v is the kinematic viscosity of liquid oxygen in [m^2/s]. The values were iterated until acceptable $y+$ values were obtained and the scalar scene of the $y+$ values can be seen in Figure 6-6. It was deemed acceptable to use $y+$ values up to 4 for the leading and trailing edges, due to convergence issues encountered during simulations caused by the aspect ratio being extremely

high. This was caused by the extremely thin but long first prism cell. The Star-CCM+™ user guide recommends a $y+$ value of below 1 for a low $y+$ treatment but $y+$ values up to 4 are acceptable (CD-Adapco, 2017).

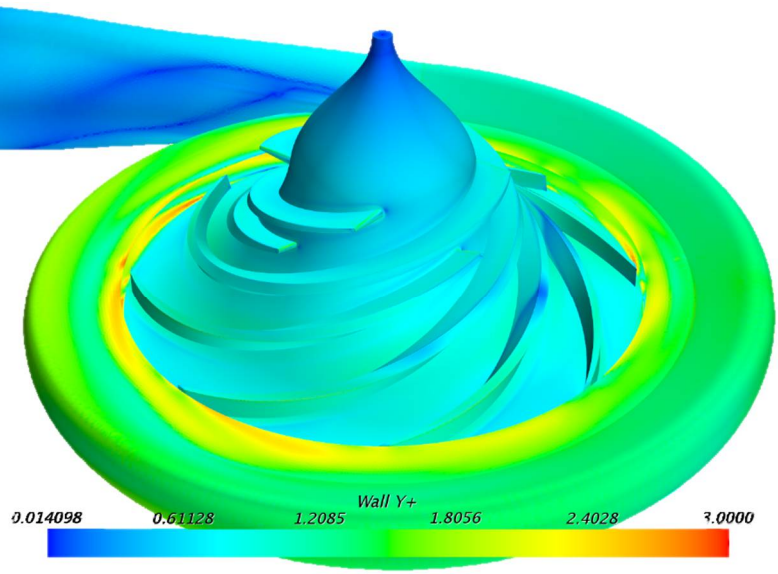

Figure 6-6: Wall $y+$ of the impeller and volute

The cell skewness angle can be used to determine the quality of the final mesh. The skewness angle is the measure of the orientation of between cell faces. The angle is determined using two vectors as are illustrated in Figure 6-7.

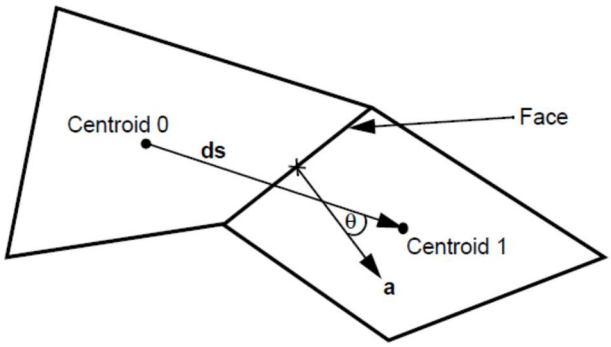

Figure 6-7: Determining the skewness angle (CD-Adapco, 2017)

A cell skewness angle of 0° indicates an orthogonal mesh whereas an angle above 90° is an indication of concave cells, typically resulting in solver convergence problems and floating-point errors. The distribution of the cell skewness angle of the final mesh is shown by the scalar scene in Figure 6-8. The scene shows that the majority of the cells in the impeller have a low skewness

angle, with the angle increasing at the blade edges and tip gap. All values remained below the threshold of 90°.

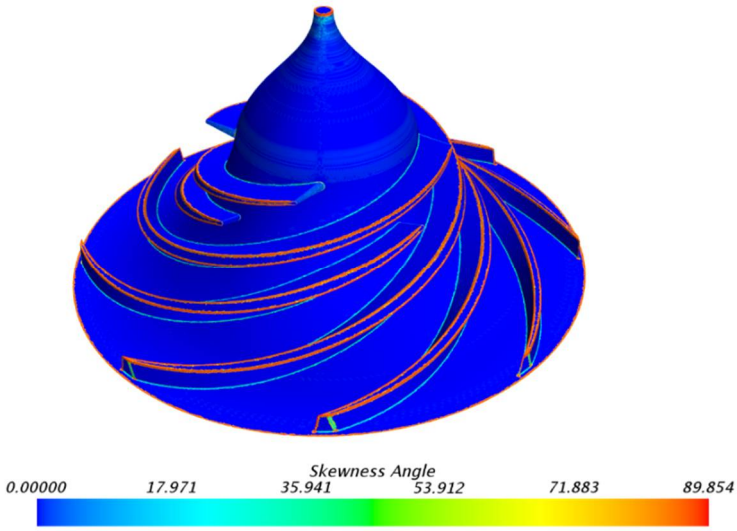

Figure 6-8: Cell skewness angle distribution

The settings used in the final mesh are dispalyed in Table 6-2.

Table 6-2: Final mesh settings

Global settings		Base size [mm]	1
		Surface growth rate	1.15
		Surface size [%]	Min: 5 Max: 100
		Number of prism layers	15
		Prism layer thickness [mm]	0.5
		Prism layer stretching	1.58
Local settings	Blades & hub	Number of prism layers	16
		Prism layer stretching	1.63
		Surface size [%]	Min: 1 Max: 25
	Leading edge	Number of prism layers	16
		Prism layer stretching	1.63
		Surface size [%]	Min: 1 Max: 15
	Diffuser & scroll	Surface size [%]	Min: 5 Max: 50

6.4 Physics models

Star-CCM+™ solves physical models that are representative of the conditions defined in the simulation using numerical methods. The steady-state and transient physics models used in this work are described in the proceeding sections.

6.4.1 Steady-state models

Star-CCM+™ does not include liquid oxygen in its material library and this was required to be manually entered into the material database. Table 6-3 displays the properties of liquid oxygen used in the Star-CCM+™ simulations.

Table 6-3: LOX properties at 80 K

Properties	**Value**
Density [kg/m^3]	1190.98
Dynamic viscosity [Pa.s]	1.956 x 10^{-4}
Vapour pressure [bar]	0.3

Turbulence models are used to provide an approximate representation of the physical phenomena of turbulence. The choice of model depends on the type of simulation being performed and the nature of the expected flow. The most commonly used turbulence models in Star-CCM+™ are the RANS models which are less computationally expensive than resolving the turbulence equation exactly. There are four RANS models used by Star-CCM+™: k-epsilon, k-omega, Spalart-Allmaras and the Reynolds stress transport (RST) model.

In this study, the shear-stress transport (SST) k-omega turbulence model was selected for both the steady and transient simulations. It is a derivative of the standard k-omega model but the transport equation is replaced by the k-epsilon equation to better cope with internal flows than the standard model (Wilcox, 2008). Gulich (2014) determined that the k-epsilon model was not useful for centrifugal pump simulations as it could not accurately cope with rotating flows. Furthermore, the RST model is computationally expensive as compared to the k-omega model, making it unpopular in the turbomachinery industry. The RST model is typically used for vortex flows. Spalart-Allmaras is exclusively used for external flows and is commonly only used for production level centrifugal pump simulations. AxCent™'s CFD tool uses the Spalart-Allmaras model. Other methods of calculating the boundary layer and turbulence phenomena involves using Large Eddy simulation (LES) models and direct numerical simulation (DNS). These methods, although the most accurate, were not used due to their high computational cost.

Wall treatment models are used to accurately predict the flow and turbulence parameters across the wall boundary layer. The wall treatment used is dependent upon the $y+$ value of the mesh which is used to define the extents of the boundary sublayers. The low $y+$ wall treatment resolves the viscous sublayer by assuming the near wall cell occurs in the viscous sublayer. This requires an extremely fine near wall mesh with a $y+$ below 1. The high $y+$ treatment assumes the near-wall cell occurs in the log-law sublayer and requires $y+$ values greater than 30 (CD-Adapco, 2017). For this work, the 'All $y+$' wall treatment was used comprises a hybrid of the low and high treatment regimes. The treatment applies the low $y+$ approach at the fine mesh zones and applies the high $y+$ treatment for coarse meshes. In areas where the near-wall centroid falls in the buffer zone ($1 < y+ < 30$), a blending function is used to calculate the turbulence quantities (CD-Adapco, 2017). Figure 6-9 illustrates how the mesh density and position of the near-wall cell centroid affect the treatment used in the All $y+$ wall treatment.

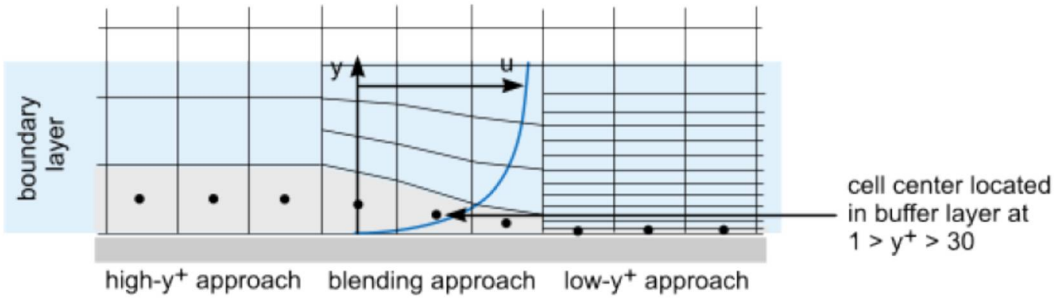

Figure 6-9: All $y+$ wall treatment (CD-Adapco, 2017)

At the inlet boundary, a stagnation inlet condition was defined, allowing for the total pressure of 3 bar to be defined. A mass flow outlet boundary condition was prescribed at the exit of the volute and was set to the design flow rate of 6.13 kg/s.

To simulate the rotation of the impeller, the moving reference frame (MRF) method is used. MRF is only applicable for steady-state simulations and provides realistic results if the flow is axisymmetric. The simulation was performed using the frozen rotor type MRF in which a rotating reference is applied to the region of the mesh containing the impeller (grey region in Figure 6-2) and the remainder of the regions remain static. The relative positions of the cell vertices do not change using this method. The shroud wall does not move, thus the reference frame for this surface was redefined as 'lab frame'.

A summary of the physics models used in the steady-state simulation is given in Table 6-4.

Table 6-4: CFD steady-state physics models

Parameter	**Model**
Turbulence model	SST k-omega
Wall treatment model	All $y+$ wall treatment
Inlet boundary	Stagnation inlet
Outlet boundary	Mass flow inlet (prescribed in outlet direction)
Rotation	Moving reference frame (MRF)
Time model	Steady
Material	Liquid
Flow model	Segregated

6.4.2 Transient models

Modelling the cavitation of the impeller required several additional physics models to be used. First, the steady-state solver was replaced with the implicit unsteady solver to perform a transient analysis. Then, multiphase models were incorporated to capture the two phase that occurs during cavitation. Lastly, the rotational motion of the impeller was required to be redefined as MRF is not supported for transient cases. The models used for turbulence and wall treatments remained constant across both simulations.

The single-phase liquid model was replaced with a multiphase fluid to emulate the interaction of the gaseous oxygen in the flow. The volume of fluid (VOF) model was used due to its numerical efficiency and its capability to resolve interfaces between the different phases of the mixture. Upon defining the two-phase mixture, the cavitation model can be selected. There are three cavitation models present in Star-CCM+™: The full Rayleigh-Plesset model, Schnerr-Sauer model and the Homogenous Relaxation model. The Homogeneous Relaxation model was deemed unsuitable for this work as it is typically used for phenomena such as flash boiling. The Schnerr-Sauer model is based on a reduced Rayleigh-Plesset equation and neglects the effect of bubble growth acceleration, viscous effects and surface tension effects. The Rayleigh-Plesset model was used in the simulation as it captures the effects of bubble growth acceleration, viscous effects and surface tension as compared to the Schnerr-Sauer model (CD-Adapco, 2017). The inlet and outlet boundaries were defined to allow only liquid oxygen to pass by setting the volume fraction of gaseous oxygen at the boundary to zero. To aid the convergence of the simulation, the domain was initialised as containing only liquid oxygen.

Rigid body motion is used in transient analyses and involves the real-time displacement of mesh vertices. A rotational motion is imposed upon the impeller region using the prescribed rotational

rate. The shroud wall was imposed with a local tangential acceleration in the opposite direction ensuring that the relative velocity at the wall was zero, as recommended by the Star-CCM+™ user and tutorial guides (CD-Adapco, 2017). The implicit unsteady model is the only transient model that can be used with the segregated flow fluid energy model. The 'new time' model requires new parameters to be set such as the time step (Δt) value and the number of inner iterations. The determination of the time step size is important in unsteady simulations, as only proper temporal resolution will result in the accurate capturing of time varying effects. The time step can be determined using the rotational speed of the impeller. Star-CCM+™ recommends that the impeller rotates by 1° per time step as an acceptable time step size. Using the recommendation, the time step can be calculated using Equation 6.3.

$$\Delta t = \frac{60\ s}{26000\ RPM * 360°} = 6.41\ \times\ 10^{-6}\ s \qquad [6.3]$$

The time step size is related to the convective Courant number (CFL), given in Equation 6.4, is a helpful indicator for validating the selected time step. The convective Courant number should average 1 on the surface of interest, indicating that the fluid moves by approximately one cell per time step. Using the time step calculated in Equation 6.3, the convective Courant number is shown in Figure 6-10. This does not rise above 1 and the calculated time step is deemed acceptable for the transient analysis.

$$CFL = \frac{v\Delta t}{\Delta x} \qquad [6.4]$$

In the above, v is the magnitude of the velocity relative to the mesh in [m/s] and Δx is the length internal in [m]. The final summary of the physics models used in the unsteady analysis is shown in Table 6-5.

Table 6-5: Summary of transient physics models

Parameter	**Model**
Multiphase model	VOF
Cavitation model	Rayleigh-Plesset
Time step [s]	6.41 x 10^{-6}
Rotation	Rigid body motion (rotational)
Solver	Implicit unsteady solver
Fluid phase	Multiphase material

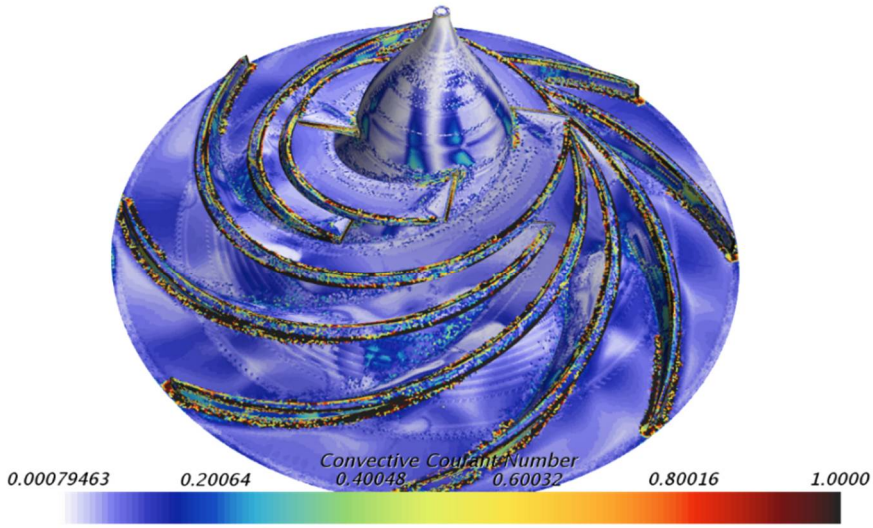

Figure 6-10: Convective Courant number

6.5 Steady-state results

As mentioned previously in Section 5.4, the initial pump design was simulated in Star-CCM+™ to determine the performance at volute exit and that the pump requirements were not met. The results from this study are included in Appendix C. This section will address the redesigned impeller.

The steady-state simulation was run using the settings in Section 6.4.1. The pressure at volute exit and the mass flow at the inlet were monitored using surface averaged pressure reports and mass flow reports respectively. The data from the reports were added to plots to monitor the stability and convergence of the solution. Convergence is the general indicator that a final solution point has been determined and the results can be accepted. Convergence does not dictate that the solution is correct, as CFD is only an approximation of the real-life solution. The convergence of the simulation was considered acceptable based upon the residual and mass flow plots. The residual plot (Figure 6-11) shows that the residuals have decreased by four orders of magnitude, while mass flow inlet (Figure 6-12) plot stabilises after approximately 300 iterations which is an indication that the solution is steady and converged. The spikes in residuals as observed in Figure 6-11 denote positions at which the simulation was restarted, with the initial conditions being retained as to promote solution convergence. Iterations onwards from 12000 are the residuals of the final simulation.

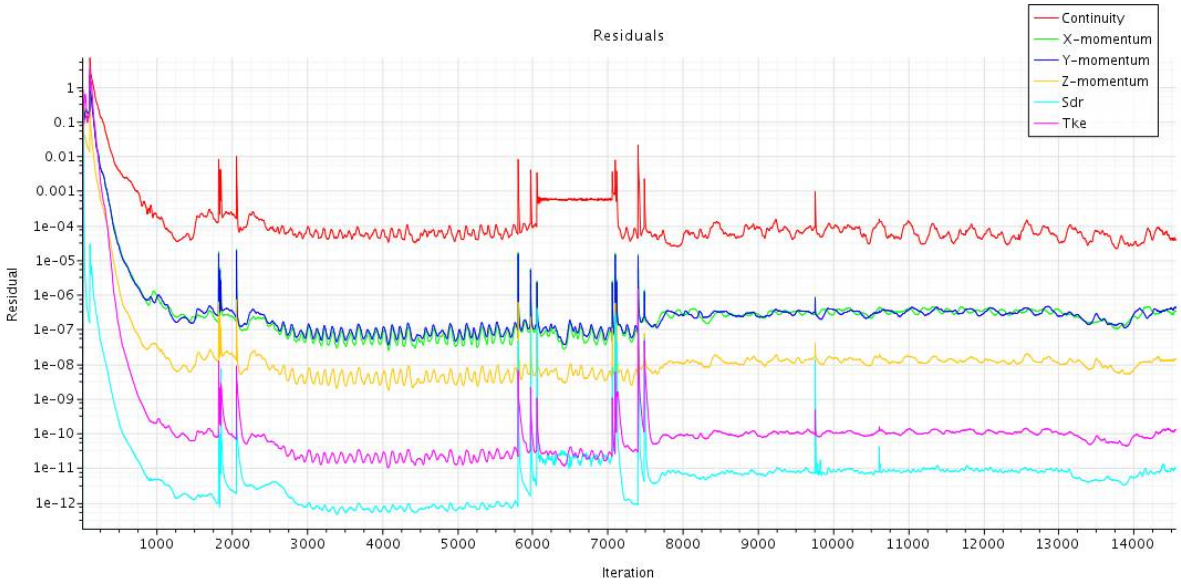

Figure 6-11: Residual plot

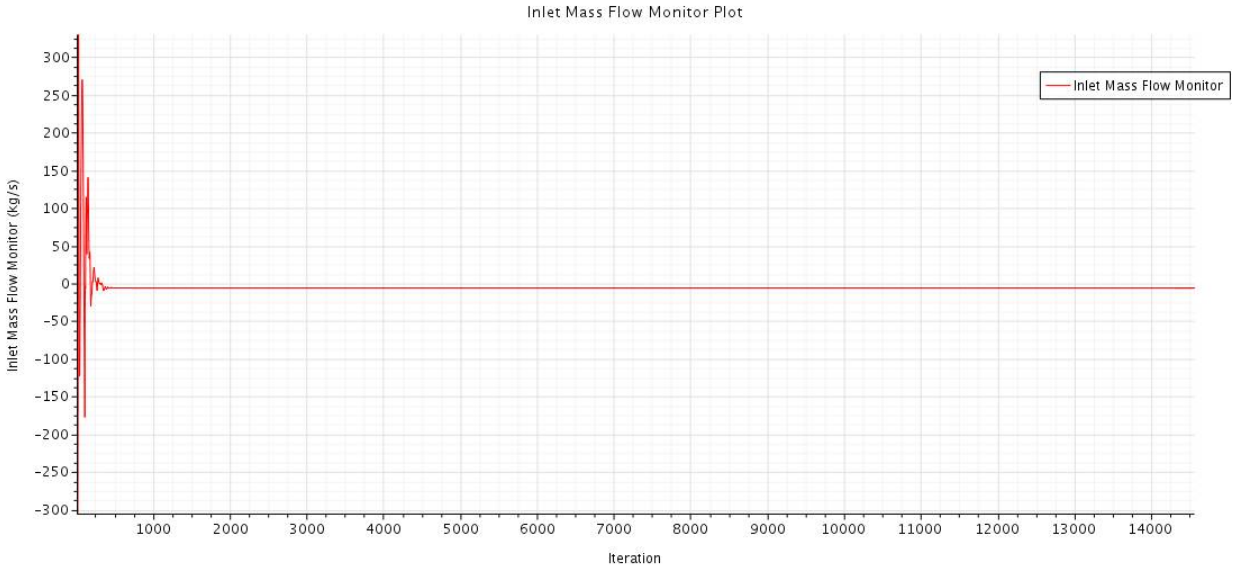

Figure 6-12: Mass flow inlet plot

The development of the pressure and velocity fields was monitored using an X-Y plane. Figure 6-13 is the cell relative velocity through the impeller. The velocity field flow is relatively even throughout the pump except for slight accelerations in the flow caused by the tongue of the volute. A slight zone of recirculation is also observed in the conical diffuser section of the volute. The static pressure scalar scene (Figure 6-14) indicates the development of the static pressure through the pump. Most of the pressure recovery that occurs in the pump, happens in the volute which is to be expected. A slight zone of increased pressure is observed at the volute tongue.

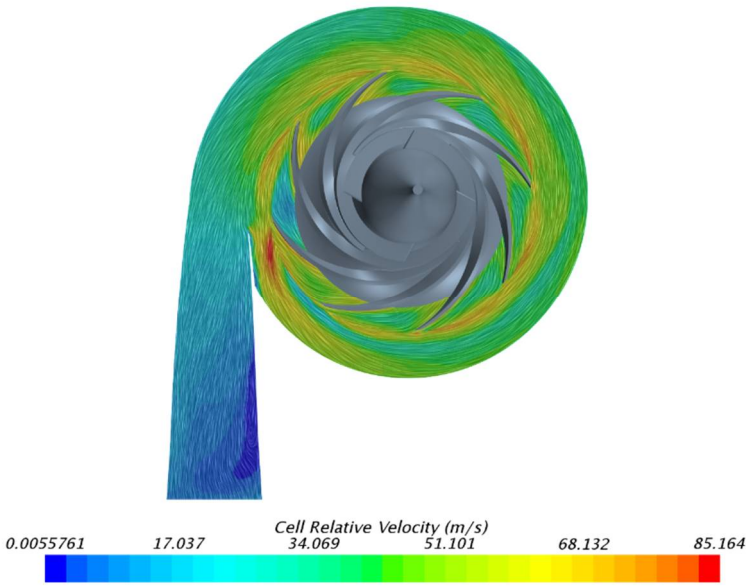

Figure 6-13: Relative cell velocity

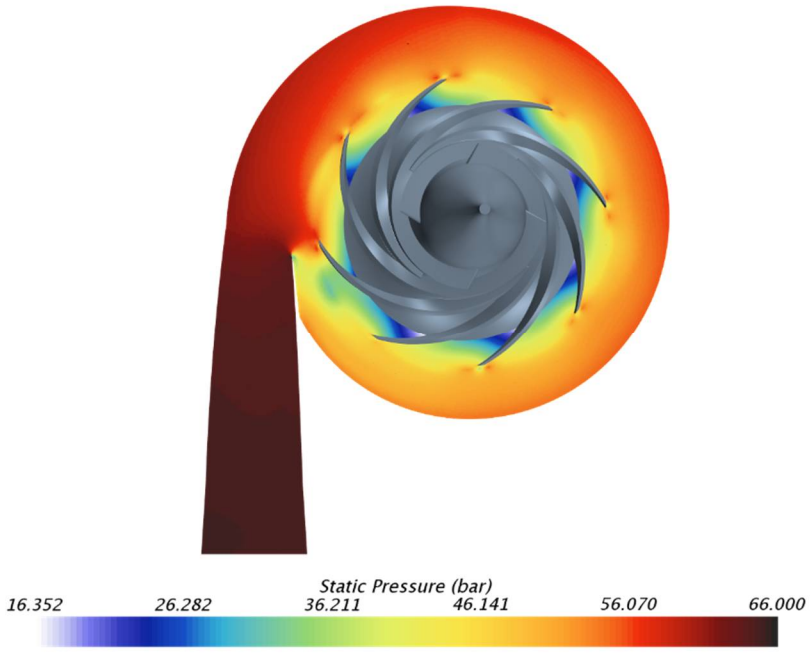

Figure 6-14: Static pressure scene

The static pressure at the exit of the impeller was determined using the interface between the impeller and volute regions. This pressure was used to compare the results obtained in the AxCent™ CFD analysis and from the mean-line design.

Table 6-6 summarises the results obtained in the steady-state analysis and compares the impeller exit pressure to the AxCent™ analysis.

Table 6-6: Summary of steady-state results

Parameter	**Steady**	**AxCent**
Static pressure outlet (volute) [bar]	64.97	-
Static pressure outlet (impeller) [bar]	46.65	46.33
Efficiency [%]	60.47	68.7
Power [kW]	52.76	44.53
Mass flow inlet [kg/s]	6.13	6.14
Solver iteration CPU time [s]	274.86	-

Theoretically, cavitating flow can be observed in the steady-state analysis by observing areas of low-pressure. Figure 6-15 is a static pressure scalar scene that has been limited to display regions of pressure that are lower than the vapour pressure of LOX. It can be observed that regions of low-pressure occur at the leading-edges of the blades indication possible cavitation inception. However, the development of the low-pressure region is not circumferentially even which may lead to unstable pressure fields when the cavitation models are incorporated and pressure fluctuates.

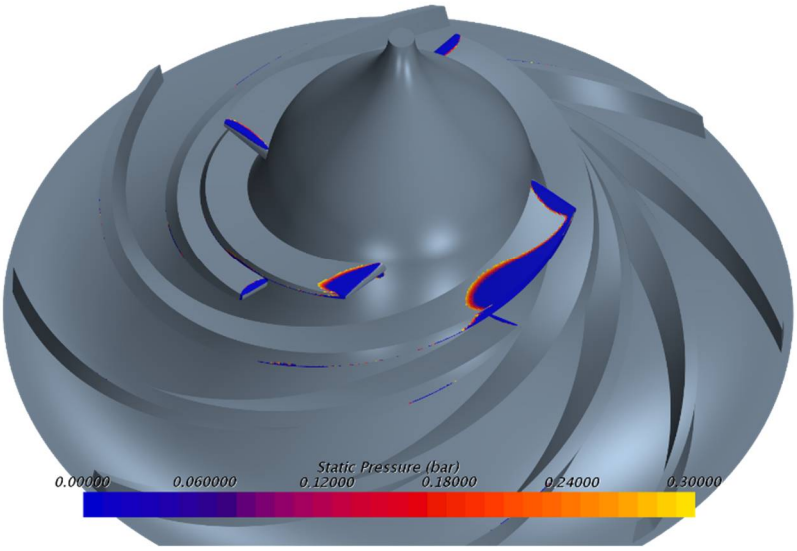

Figure 6-15: Low-pressure regions of steady-state analysis

The design was altered by changing the single exit volute into a twin exit volute in order to conteract the uneven pressure distribution. The twin exit volute promotes the circumferential

distribution of even velocity and pressure fields and provides radial thrust balancing due to the volute exits (Kang and Li, 2015).

6.5.1 Twin volute steady-state analysis

The twin volute geometry was developed using AxCent™'s volute designer. This allows for the generation of a second volute and accurately determines the dimensions such that the hydraulic performance at the outlet of the twin volutes is the same as the single volute. The computational domain for the twin volute model was developed similarly to the single volute design and is shown in Figure 6-16. The use of two volutes will not significantly affect the complexity of the plumbing for the SAFFIRE engine.

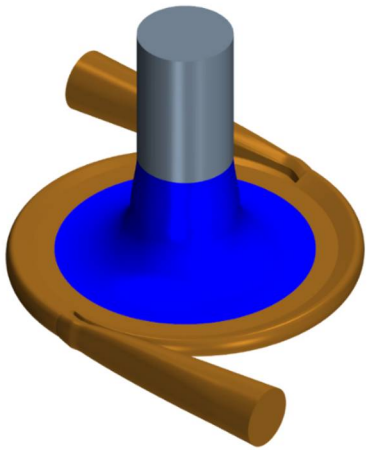

Figure 6-16: Twin volute computational domain

The domain was meshed using the settings obtained during the mesh independence and $y+$ study. The new $y+$ values were observed using the scalar scene shown in Figure 6-17.

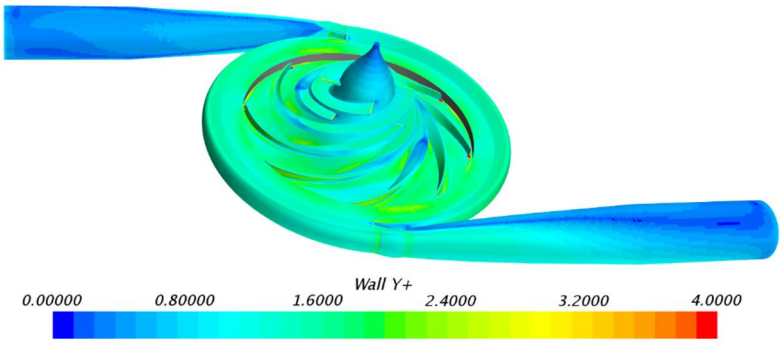

Figure 6-17: Wall $y+$ of the twin volute mesh

Convergence of the simulation was monitored using the residual and monitor plots similarly to the single volute steady-state analysis. The pressure and velocity field (Figure 6-18 and Figure 6-19 respectively) were monitored using planes through the X-Y plane of the computational domain. The static pressure field developed more evenly as compared to the single volute design. However, the double volute design has a large zone of separation and recirculation in the conical diffuser section of the volute. This is caused by the reduced flow through the volute section imposed by the twin volute design. The reduced flow decreases the meridional velocity of the flow, increasing the swirl which in turn promotes recirculation.

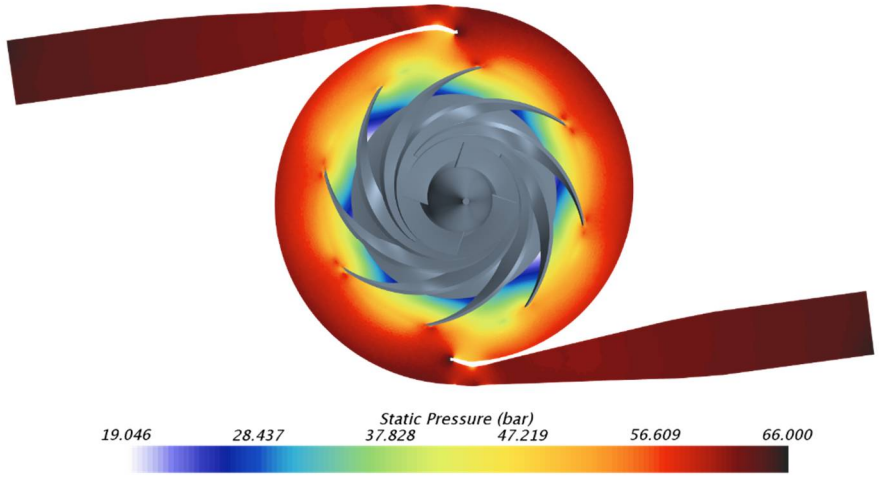

Figure 6-18: Static pressure scalar scene of the twin volute

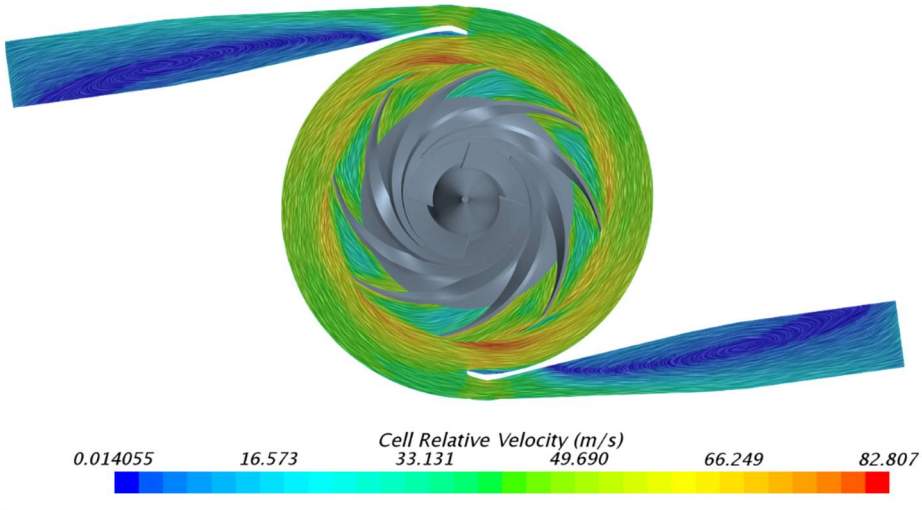

Figure 6-19: Cell relative velocity scene of the twin volute

The twin volute design change had the desired effect on the circumferential evenness of the low-pressure regions. Figure 6-20 displays the regions of low-pressure that occur similarly to the single volute design. It can be seen that the twin volute low-pressure regions are significantly smaller than the single volute design, and the regions are distributed axisymmetrically.

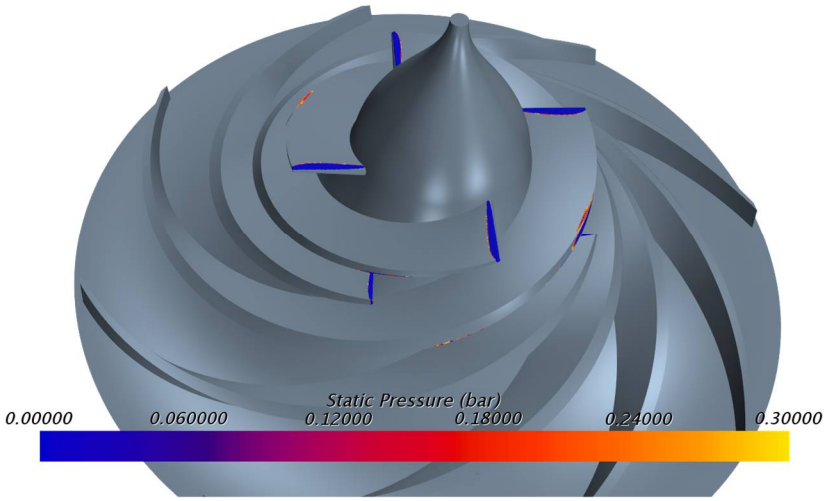

Figure 6-20: Low-pressure regions of twin volute

The results from the twin volute and single volute steady-state analysis were compared and the results are displayed in Table 6-7.

Table 6-7: Comparison of twin and single volute designs

Parameter	**Single volute**	**Twin volute**
Static pressure outlet (volute) [bar]	64.97	64.9
Static pressure outlet (impeller) [bar]	46.65	50.56
Efficiency [%]	60.47	63.03
Power [kW]	52.76	51.62
Mass flow inlet [kg/s]	6.13	6.13
Solver iteration CPU time [s]	274.86	284.45

The twin volute design possessed better overall performance compared to the single volute design, therefore the unsteady cavitation analysis was restricted to the twin volute design.

6.5.2 Other steady-state analyses

Three other simulation studies were performed using the twin volute simulation, to investigate the off-design performance of the pump, the effects of using sub-cooled LOX and the influence of using Jet A-1 as the fuel instead of RP-1.

6.5.2.1 Off-design performance

The off-design performance of the pump is important when considering SAFFIRE engine throttling. The steady-state simulation mass flow rate was varied, to determine the effect of the changing flow rate on the head rise of the pump. This allowed the development of a pump curve for the oxidiser pump at the design speed of 26000 rpm (Figure 6-21). The steady-state simulation was used to develop the pump curve to avoid the high computational cost of running multiple transient simulations at varying flow rates.

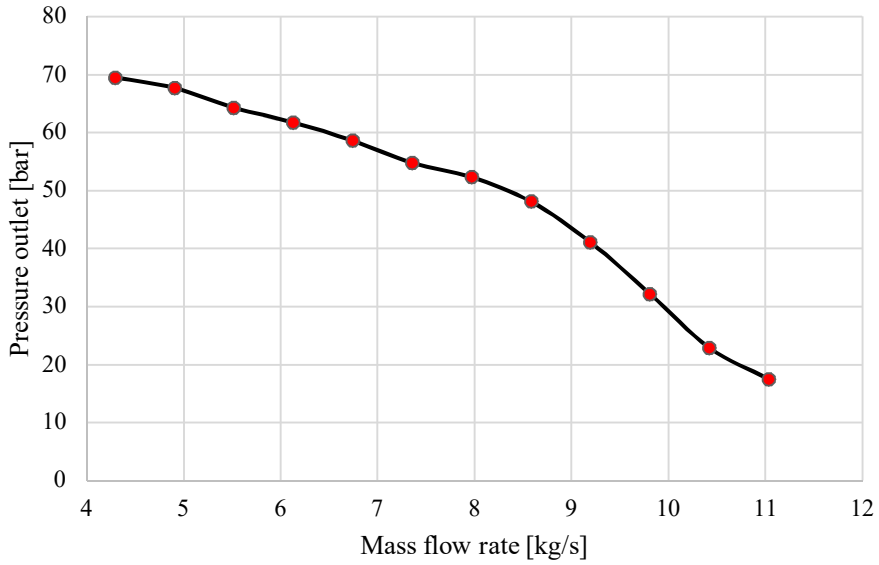

Figure 6-21: Oxidiser pump curve for 26000 rpm

6.5.2.2 Super-cooled liquid oxygen analysis

SpaceX recently began using chilled liquid oxygen (at 66 K) as opposed to LOX at the normal operating temperatures of 80 – 90 K. Their reasoning is that the density of the fluid can be increased, allowing the storage of the same amount of LOX as previously but with a smaller volume tank (Fernholz, 2016). For the purpose of the present study, a steady-state analysis was performed to determine the performance benefits, if any, from using super-cooled liquid oxygen. The properties of LOX at the prescribed temperature are given in Table 6-8 and were calculated using REFPROP™ and Equation 2.2.

Table 6-8: LOX properties at 66 K (Stewart and Jacobsen, 1991)

Properties	**Value**
Density [kg/m^3]	1255.6
Dynamic viscosity [Pa.s]	439.49 x 10^{-6}
Vapour pressure [Pa]	2881.92

Results were obtained using similar methods to the main steady-state analysis and a comparison of the main performance parameters are shown in Table 6-9.

Table 6-9: Comparison between super-cooled LOX and LOX used in analysis

Parameter	**80 K**	**66 K**
Static pressure outlet (volute) [bar]	64.9	69.28
Static pressure outlet (impeller) [bar]	50.56	54.42
Efficiency [%]	63.03	66.4
Hydraulic power [kW]	51.62	52.3
Mass flow inlet [kg/s]	6.13	6.13
Solver iteration CPU time [s]	284.45	310.15

The results show positive performance increases using super-cooled LOX. This is due to the increased density of the fluid, which translates to an increase in the hydraulic power of the pump (Equation 4.10). The viscosity of the fluid increases slightly which results in a pressure drop due to the higher liquid shear generated. However, the shear resistance is not great enough to offset the increase in pressure derived from the increase in density.

The vapour pressure of LOX drops significantly at 66 K from 0.3 bar to 0.028 bar. This may reduce the size of the low-pressure regions and increase the cavitation performance of the impeller. A scalar scene of the low-pressure regions is shown in Figure 6-22.

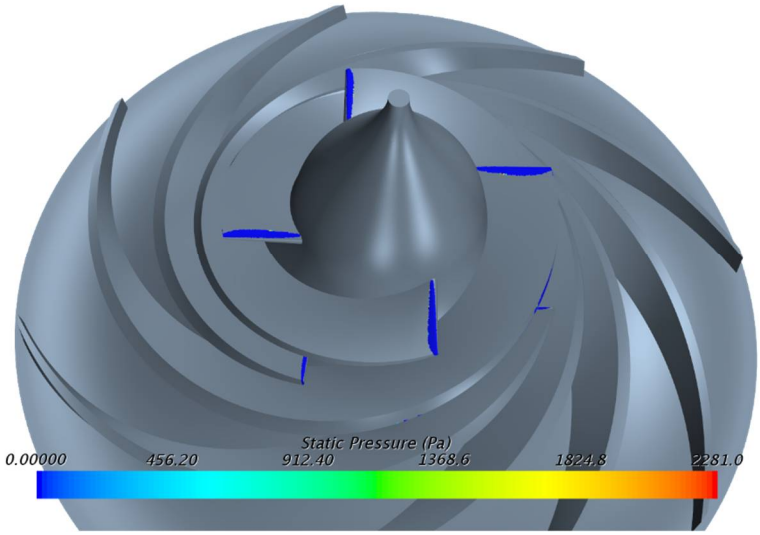

Figure 6-22: Low-pressure regions

The disadvantage of using super-cooled LOX is in the handling and safety measures that are required. Due to the low temperature, the LOX can only be stored in the propellant tanks close to take-off and super-cooled LOX will warm as a liquid over time, causing it to expand and increase the tank pressure. Normally, LOX would vapourise and the excess pressure vented off. In this case, excess liquid would require to be 'vented' to avoid over-pressurisation of the tank.

6.5.2.3 Jet A-1 analysis

The SAFFIRE engine is intended to operate on LOX and highly refined kerosene (RP-1). However, given the availability of RP-1 and that the chamber is ablatively cooled there is less concern with coking of the cooling channels, as occurs in regeneratively cooled engines (Wunderlin et al., 2017). For this reason, a study was performed to assess the pump performance when RP-1 is replaced with the less refined, more easily accessible and cheaper fuel, Jet A-1. A combustion analysis performed by Wunderlin et al. (2017) determined that the LOX/Jet-A combination had a lower O/F ratio as compared to LOX/RP-1 resulting in a decrease in the oxidiser mass flow rate. Using the new flow rate of 5.79 kg/s an analysis was performed to determine the performance of the oxidiser pump using this propellant combination. The results of study are shown in Table 6-10.

Table 6-10: Comparison between propellant combinations

Parameter	LOX/RP-1	LOX/Jet-A
Static pressure outlet [volute]	64.9	63.3
Static pressure outlet [impeller]	50.56	49.55
Efficiency [%]	63.03	62.87
Power [kW]	51.62	46.68
Mass flow inlet [kg/s]	6.13	5.79
Solver iteration CPU time [s]	284.45	144.474

The change of fuel does not affect the oxidiser performance greatly, and still meets the pump requirements without the need for any redesign.

6.6 Unsteady cavitation analysis results (LOX/RP-1)

An unsteady analysis was performed using the results from the steady analysis as the initial conditions. This aided the convergence and reduced the time required to obtain the final result. Convergence in the unsteady simulation differs from the steady as the residuals cannot be used as validation. This is because that the residuals in the unsteady simulation spike after each time step due to the moving mesh, as seen in Figure 6-23. Therefore, convergence is determined through observing the inner iterations of each time step. The inner iterations were observed for the mass flow inlet monitor and it was noted that the mass flow converged at each time step as shown in Figure 6-24. The steps are still decreasing in Figure 6-24 due to solution still converging.

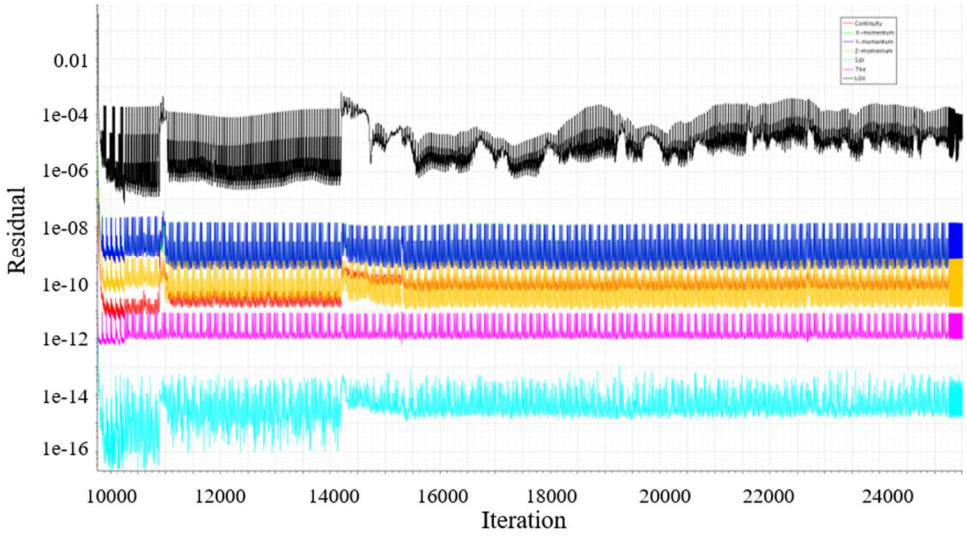

Figure 6-23: Residuals for the unsteady analysis

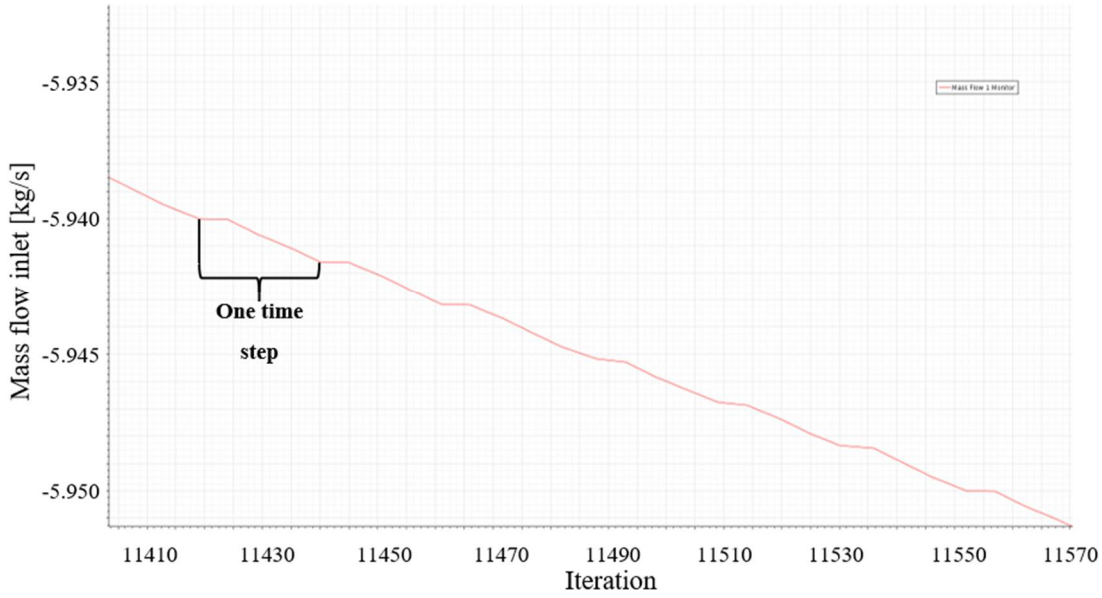

Figure 6-24: Inlet mass flow monitor for the unsteady analysis

The simulation ran for three impeller rotations which is deemed appropriate for turbomachinery simulations by Star-CCM+™. The outlet pressure oscillates between 66 and 62 bar at the extremes, averaging approximately 64 bar. The pressure fluctuations are caused by the cavitating flow and the flow blockages it causes at the inlet. Cavitation inception and development on the impeller leading edge was observed using a scalar scene of the volume fraction of liquid oxygen. An iso-surface displaying the volume fraction of gaseous oxygen was used to observe the cavitation. The cavitation was observed to form at the suction side of the leading-edge of the blade where the static pressure due to the centrifugal force and local acceleration effects was at its greatest. A snapshot of the scenes was taken at each time step. The cavitation levels at the peak and minimum outlet pressures were observed. The cavitation levels at the peak pressure of 65.7 bar are shown in Figure 6-25. It was noted that at the peak pressure, the efficiency of the pump was the lowest and it drew the highest power at 54.18 kW.

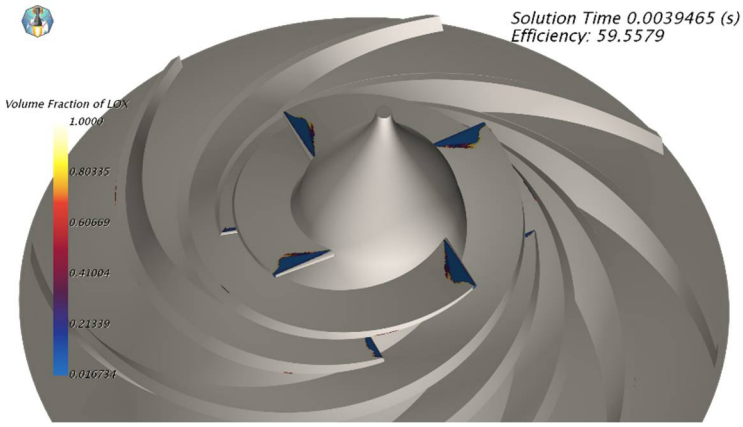

(a)

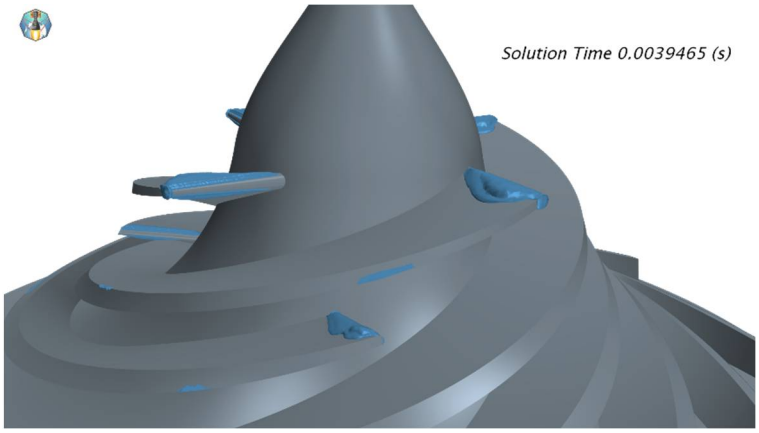

(b)

Figure 6-25: The (a) volume fraction of LOX and (b) the iso-surface of cavitation at the peak outlet pressure of 65.7 bar

The cavitation levels at the lowest pressure point, of 62.03 bar, is shown in Figure 6-26. The two-phase flow has developed further along the blade at the minimum pressure indicating a larger low-pressure zone and more cavitation. This explains the why the lowest pressure in the system is obtained at this point.

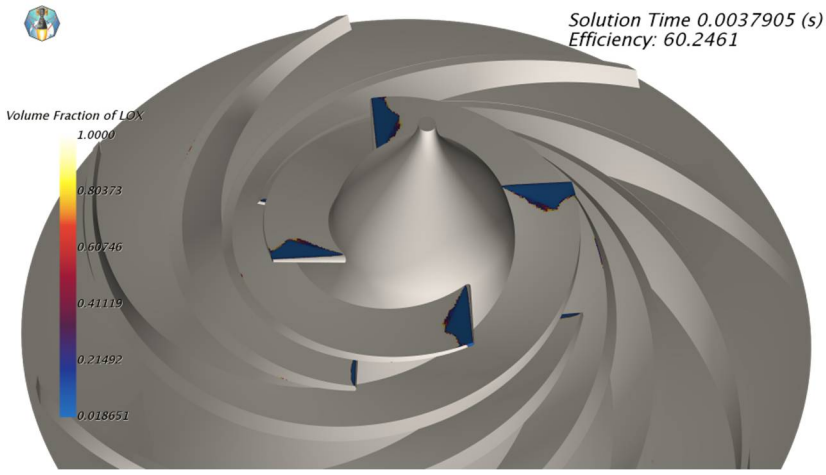

(a)

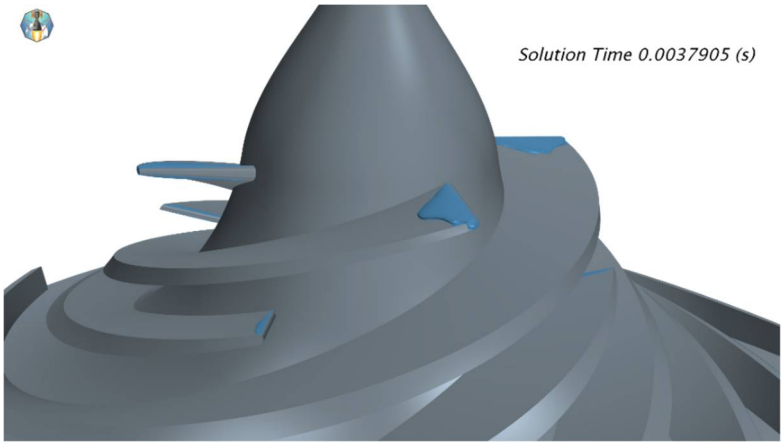

(b)

Figure 6-26: The (a) volume of LOX and (b) iso-surface at the lowest static outlet pressure of 62.03 bar

Due to the oscillating nature of the unsteady simulation, it was difficult to quantify the results as a singular performance output. Table 6-11 summarises the performance of the oxidiser pump after three full rotations and compares these results to the steady-state and AxCent™ CFD.

Table 6-11: Final unsteady simulation results

Parameter	**Unsteady**	**Steady**	**AxCent**
Static pressure outlet (volute) [bar]	64.17	64.9	-
Static pressure outlet (impeller) [bar]	49.54	50.56	46.33
Efficiency [%]	60.76	63.03	68.7
Power [kW]	51.96	51.62	44.53
Mass flow inlet [kg/s]	6.13	6.13	6.14
Solver iteration CPU time [s]	1355.2 per time step	284.45	-

Because of cavitation, the unsteady simulation had the lowest outlet pressure decreasing by approximately 1 bar from the steady-state simulation. The oxidiser pump meets the pump volute outlet requirements set out by the system analysis in Section 3.4. The scalar scenes for the velocity and pressure field after three rotations are displayed in Figure 6-27 and Figure 6-28 respectively. Recirculation zones can be seen in the volute of the velocity vector scene like the results obtained in the steady-state analysis, with the reasoning explained in Section 6.5.1. Solutions to combat the recirculation is discussed are Section 7.2. The level of cavitation at the end of the third rotation is displayed in Figure 6-29. The simulation ran for approximately 135 hours to obtain the solution after three full rotations.

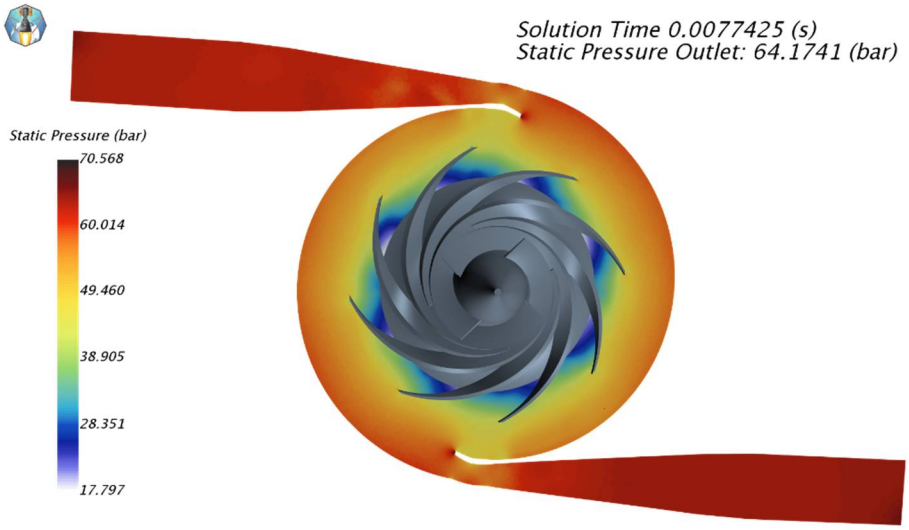

Figure 6-27: Slice showing the static pressure development after three revolutions

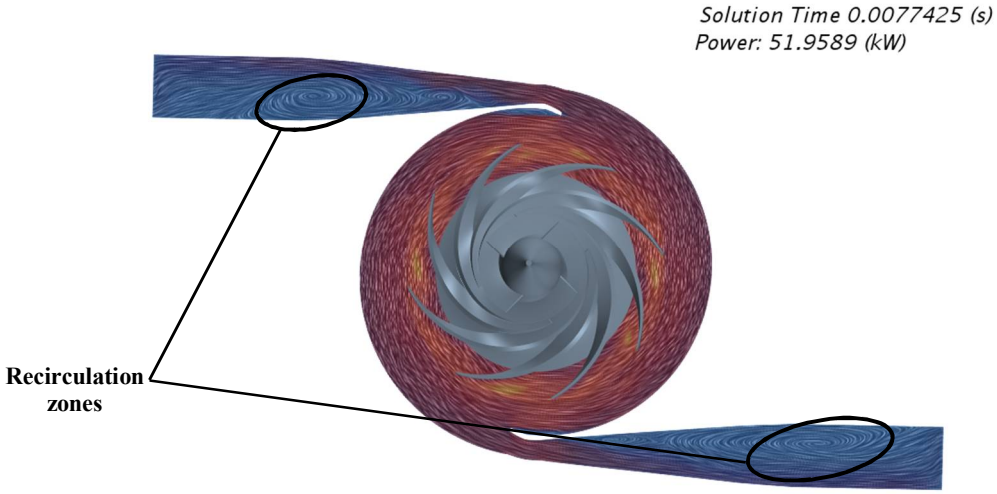

Figure 6-28: The velocity field in the pump after three revolutions

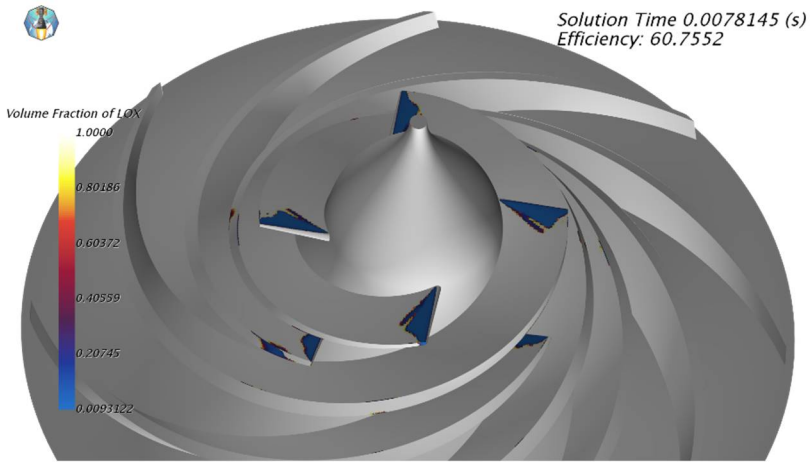

Figure 6-29: Volume fraction of LOX

6.7 Summary

A steady-state analysis was performed in Star-CCM+™ using the imported design developed using PUMPAL™ and AxCent™. The pressure field was observed to be circumferentially uneven and decision was made to use a twin volute design. The twin volute design produced an axisymmetric pressure field with greater performance, in terms of efficiency and power requirements, than the conventional design. The unsteady cavitation analysis determined that cavitation inception occurs on the suction side of the leading-edge of the blade and that a cavitation pocket develops at the blade inlet. The hydraulic performance of the pump was hampered by the cavitation, but nevertheless still met the prescribed pump requirements for the engine. A rendering of the final impeller is shown in Figure 6-30.

Figure 6-30: Final pump rendering

Chapter 7. Conclusion and Recommendations

The main objective of this work was to design a liquid oxygen pump impeller that can be incorporated into an electro-pump system for SAFFIRE. SAFFIRE is proposed for use in a South African small-sat launch vehicle to provide space access for the growing CubeSat markets in South Africa and the rest of the world. The oxidiser pump was required to deliver an outlet pressure of 62.8 bar at a mass flow rate of 6.13 kg/s. To appropriately conclude this work, the achievement of the study's objectives is discussed:

1. The development of the analytical and mean-line design (PUMPAL™)
2. CFD analysis using AxCent™ and Star-CCM+™
3. The final working design

Recommendations to improve the impeller design and analysis and possible future work required involving the oxidiser pump are also addressed in the subsequent sections.

7.1 Conclusion

The three main design components are discussed in the following sections.

7.1.1 Mean-line design

The analytical design process utilised accepted centrifugal pump design techniques developed by various authors. LOX was assumed as an incompressible fluid and conventional hydrodynamic one-dimensional design techniques were used to develop a working design range for the impeller geometry. The analytical design was constrained by empirically derived relationships and recommendations from experienced turbomachinery guides (Furst, 1973; Huzel and Huang, 1992; Japikse et al., 1997). The analytical design was iterated using these constraints and the established pump requirements to develop a suitable pump geometry that could be further analysed in PUMPAL™.

PUMPAL™ allows for the rapid generation of pump geometry and analysis using the mean-line solver method. This allowed for the performance analysis of various impeller parameters such as the exit swirl and blade angle, to optimise the analytical design. An optimised impeller geometry was developed in PUMPAL™ yielding an efficiency of 82.7% when operating at a speed of 23000 rpm. Further quasi-3D and CFD analysis were performed in AxCent™, a sister product of PUMPAL™, to identify any through-flow and 3D flow problems.

The Multiple Streamtube solver was used to refine the mean-line design developed in PUMPAL™. MST is a quasi-3D technique that is used to analysis the impeller's through-blade

performance and hydrodynamic blade loading. Three different blade number configurations were tested and a 4 – 8 splitter blade combination was used as it possessed the best performance and blade loading characteristics from the three arrangements. A CFD analysis was then performed on the mean-line design.

7.1.2 CFD analysis

The CFD analysis was completed using AxCent™'s built-in Pushbutton CFD™ software. The AxCent™ along with a preliminary Star-CCM+™ CFD analysis showed that the pump did not achieve the required outlet pressure as prescribed by the system analysis. The problem was resolved through a re-design of the impeller, by increasing the outer radius by 5 mm to 43 mm and increasing the speed to 26000 rpm. The new geometry increased the hydraulic performance of the impeller and formed the final iteration of the pump impeller. The CFD analysis showed low-pressure regions on the leading-edges of the impeller blades. To analyse the low-pressure regions and possible cavitation a high-level CFD analysis was performed using Star-CCM+™.

Two analyses were performed in Star-CCM+™; a steady-state and an unsteady cavitation analysis. The steady-state analysis was conducted to ensure the pump achieved the desired performance outputs and to analyse the velocity and pressure development through the machine. The volute design was switched from a single to a twin outlet design to mitigate the effects of the throat of the volute on evenness of the flow distribution. Subsequent analyses proved that the design change has the desired effect.

The unsteady cavitation analysis allowed for the inception and development of cavitation along the blades to be observed during three pump rotations. Cavitation along the blade leading-edges is common in high speed pumping applications (Huzel and Huang, 1992) and is defined as incipient cavitation. The cavitation levels were deemed to be acceptable as the bubble formation did not extend severely along the blade chord and the performance of the pump was still acceptable as the requirements set out at the beginning of the study was met.

7.1.3 Final design

The final design performance of the pump as predicted by the unsteady analysis is an exit static pressure of 64.17 bar at a mass flow rate of 6.13 kg/s with an efficiency of 60.76%. The final impeller has an exit diameter of 86 mm and operates at a speed of 26000 rpm. It is worth noting that a CFD analysis is just an approximation as to the performance of the pump and the true performance can only be gauged through testing. Lastly, the efficiency of impeller corresponds well with literature for low specific speed centrifugal pumps and using NASA guidelines for

specific speed and efficiency, the impeller is approximately 3% below the maximum achievable efficiency according to experience and testing (Huzel and Huang, 1992).

7.2 Design recommendations

The results of the CFD analyses revealed possible areas whereby the design could be improved such that a higher efficiency and better performance could be obtained. The areas of the design that could be improved are the volute, where major zones of recirculation can be seen in the conical diffuser section, and the cavitation viewed at the leading-edge of the blades. It is noted that the current pump design meets the proposed SAFFIRE engine performance requirements and that further refinement may not be necessary.

7.2.1 Full volute design

A large zone of recirculation was observed in the conical diffuser sections of both exits (Figure 6-28). This is attributed to the low meridional velocity in the exit pipes and the positioning of the volute tongue or cutwater. The flow accelerates at the tongue of the volute and then decelerates at the exit causing the circumferential rise in pressure. The acceleration at the tongue leads to extreme pressure loading, causing unevenness in the pressure field and complicating the flow field of the impeller.

The first component of the volute that should be investigated is the cutwater or volute tongue. The tongue region is generally one of the most 'chaotic' flow regions in a centrifugal pump and an investigation into various tongue designs can aid in mitigating the effects it has on the flow field. The diameter, profile and the thickness of the cutwater can be altered such that interferences in the flow are avoided. This may help in increasing the efficiency of the pump, stabilise the *Q-H* curve and reduce local velocities and blockage in the tongue region (Gulich, 2014). A CFD study performed on varying the angles of the tongue region showed that a more moderate angle of 50° as opposed to the normal angle of 22.5° used in this work, may provide more even static pressure recovery and better off-design performance (Qiang et al., 2010). The wrap angle of the volute can be investigated to better avoid recirculation with regards to the twin volute approach. The wrap angle affects pressure pulsations through the pump and can be attributed to increasing or decreasing the radial thrust, depending on the angle. The volute contour can be adjusted to promote smooth transition from the diffuser to the volute and avoid recirculation and flow separation in the volute. The contour design would need to be iterated, and the flow field analysed through a CFD study. The pump operates at a low specific speed and it is recommended in some cases to use a partial volute (double volute) exit. This may prevent recirculation at the volute exit but is a complicated solution to implement practically.

The improvement of the volute performance could serve as a future study requiring various CFD analyses to determine the optimal volute geometry for the oxidiser pump.

7.2.2 Cavitation

The unsteady analysis provided evidence of cavitation formation and slight propagation at the leading-edges of the blades. The cavitation did not appear significant enough to cause a major performance reduction, with the pump still meeting the overall requirements. However, there remain a few design changes that can be implemented to reduce the cavitation at the inlet and increase the performance of the pump.

The profile of the leading-edge is an interesting geometrical feature. A blunt profile promotes local flow accelerations resulting in static pressure drops due to shock and entrance losses that are encouraged by the sharp contour. A CFD study by Balasubramanian and Bradshaw (2011) on blade leading-edges determined that sharp, elliptical leading-edges had the best performance with superior $NPSH_r$ performance compared to other designs. Furthermore, the growth of bubbles and the area affected by cavitation were far smaller than the other tested profiles. The current leading-edge profile of the oxidiser impeller can be re-evaluated using different elliptical profiles to determine the elliptical profile with the best performance.

A further alternative to reduce or suppress the cavitation at inlet, is the implementation of an axial inducer. Inducers raise the static pressure upstream of the impeller, thus reducing the $NPSH_r$ required by up to 50%. This allows for the pump to operate at higher speeds and at higher efficiencies. An inducer typically consists of 2 to 4 blades of a helical-shape. Gulich (2014) provides a design process for an inducer which is described below:

1. Parameters such as flow rate, speed and approach flow angle are set by the impeller design
2. Blade numbers typically 2 – 4 are selected
3. Inlet diameter is designed for a selected suction speed
4. Inlet blade angles are determined using velocity triangles
5. The outlet diameter is based upon hub profile and inlet diameter of the pump impeller
6. The outlet blade angle is assumed to be equal to the inlet blade angle and static pressure rise is calculated

The design process described above is summarised and there are still further parameters to calculate to generate a full inducer geometry. The inducer should then be investigated via CFD analysis to determine whether the suction performance improves or the inducer itself cavitates (Franc et al., 2004; Hosangadi et al., 2004).

7.3 Future Work

The SAFFIRE LOX pump impeller and its components have been designed and have successfully met the performance objectives set out in the pump and engine requirement study. Before the pump can be implemented in the rocket engine, further analyses, component design and tests are required.

7.3.1 Pump system and layout

The final impeller design presented here does not include various components such as bearings, wear rings and seals. A full mechanical assembly design and analysis is required before the impeller can be manufactured for testing. The use of LOX further complicates the process due to the volatility of the fluid. An analysis is required to determine unbalanced forces that exist due to fluid pressure and fluid momentum changes in the pump. This can be achieved through a Fluid-Structure Interaction (FSI) analysis. The FSI analysis is a hybrid study using both CFD and FEA and, among others can help determine the devices required to balance axial thrust forces at the pump bearings. Devices used for balancing include balance ribs, balance pistons, impeller wear rings and thrust bearings. Impeller wear rings are typically made from polychlorotrifluoroethylene (PCTFE) and stainless steel for LOX pump systems. Roller element bearings or hydrostatic bearings are commonly used to balance axial thrust in rocket turbopump systems (Furst, 1973; Japikse et al., 1997).

Seals are required to reduce flow leakage, balance pressures in the system and prevent potentially disastrous interaction between fluids and materials. Gas-type floating ring and face seals are commonly used to seal off LOX components and must withstand extreme temperature gradients and rubbing friction at high speeds. Helium purge seals are favoured in LOX systems for controlling and reducing oxygen leakage (Burcham, 1978).

Lastly, a rotodynamic analysis is required to determine shaft deflection and the effects of vibrations in the system.

7.3.2 Battery and motor design

A challenging aspect of SAFFIRE is that the pumps must be driven by electric motors as opposed to gas-driven turbines. A thorough effort is needed to survey the market and determine suitable batteries for use in the rocket power packs and electric motors that meet the power requirements of the pump. Current battery technology identifies Li-ion batteries and Li-Po batteries as strong candidates for the pack. There can be readily sourced from suppliers such as Valence (Valence, 2017).

The motor design may prove to be trickier than the battery design to accomplish, due to the high-speed and high-power requirements of the pump. Since commercial high-speed motors operate at lower power and high-powered motors operate at low speeds, it is possible that a unique motor design will be required.

7.3.3 Manufacturing and testing

The final step of the impeller design process is manufacturing and testing under controlled conditions. The impeller is to be fabricated out of Inconel 718 and this can be accomplished through either casting or 3D printing. The impeller test rig developed by Philogene (2014) could possibly be used to test the oxidiser pump impeller. Impeller testing would form the last phase of the individual pump design and refinement process with the next step being integration into a full test engine. This should be followed by a single engine hot fire test.

References

Amirante, R., De Bellis, F., Distaso, E. and Tamburrano, P. (2015) 'An Explicit , Non-Iterative , Single Equation Formulation for an Accurate One Dimensional Estimation of Vaneless Radial Diffusers in Turbomachines', *Journal of Mechanics*, 31(2), pp. 113–122. doi: https://doi.org/10.1017/jmech.2014.72.

Anderson, C. (2017) *Milestone for South African satellite technology*, *Brand South Africa*. Available at: https://www.brandsouthafrica.com/investments-immigration/science-technology/milestone-south-african-satellite-technology (Accessed: 27 September 2017).

Ardizzon, G. and Pavesi, G. (1998) 'Optimum incidence angle in centrifugal pumps and radial inflow turbines', *Proceedings of the Institution of Mechanical Engineers, Part A: Journal of Power and Energy*, 212(2), pp. 97–107. doi: 10.1243/0957650981536628.

Bacharoudis, E. C., Filios, A. E., Mentzos, M. D. and Margaris, D. P. (2008) 'Parametric Study of a Centrifugal Pump Impeller by Varying the Outlet Blade Angle', *The Open Mechanical Engineering Journal*, 2(1), pp. 75–83. doi: 10.2174/1874155X00802010075.

Balasubramanian, R. and Bradshaw, S. (2011) 'Influence of Impeller Leading Edge Profiles on Cavitation and Suction Performance', in *27th International Pump Users Symposium proceedings*. Houston, Texas: Turbomachinery Laboratory, Texas A & M University, pp. 34–44.

Barron, R. F. (1985) *Cryogenic Systems*. 2nd edn, *Monographs on Cryogenics*. 2nd edn. New York, USA: Oxford University Press, Inc.

Brennen, C. E. (1994) *Hydrodynamics of Pumps*. 1st edn. Pasadena, California: Concepts ETI.

Burcham, R. (1978) *Liquid Rocket Engine Turbopump Rotating Shaft-Seals*. Lewis Research Center, Cleveland: NASA SP-8121.

CD-Adapco (2017) 'Star-CCM+ User Guide v12.04'. New York, USA: Siemens.

Chetty, C. (2017) *Conceptual Development of a Liquid Rocket Engine and Subsequent Hydrodynamic Design of a RP-1 Electropump (submitted)*. MScEng Thesis: Mechanical Engineering, University of KwaZulu-Natal: Durban.

Concepts NREC (2016a) 'AxCent v8.4.3 User Guide'. White River Junction, VT: Concepts NREC.

Concepts NREC (2016b) 'PUMPAL v8.0 User Guide'. White River Junction, VT: Concepts NREC.

Daily, J. W. and Nece, R. E. (1960) 'Chamber Dimension Effects on Induced Flow and Frictional Resistance of Enclosed Rotating Disks', *Journal of Basic Engineering*, 82(1), pp. 217–230. doi: 10.1115/1.3662532.

Dean, R. C. (1974) *The Fluid Dynamic Design of Advanced Centrifugal Compressors*. 1st edn. Von Karman Institute, Brussels: Creare, Incorporated.

Dimitrenko, A., Ivanov, A., Kravchenko, A., Mishin, A. and Pershin, V. (2000) 'Development Testing of an Advanced Liquid Oxygen Turbopump', in *36th AIAA Joint Propulsion Conference and Exhibit proceedings*. Huntsville, Alabama: American Institute of Aeronautics and Astronautics, p. 8.

Fernholz, T. (2016) *The 'super chill' reason SpaceX keeps aborting launches*, *Quartz*. Available at: https://qz.com/627430/the-super-chill-reason-spacex-keeps-aborting-launches/ (Accessed: 30 November 2017).

Firefly Space Systems (2017) *Firefly Alpha*, *Firefly Space Systems*. Available at: http://www.fireflyspace.com/vehicles/firefly-a (Accessed: 27 January 2017).

Fitzgerald, D. (2016) *Design and Aerodynamic Analysis of a Supersonic Gas Turbine to Drive a Commercial Rocket Booster Engine Turbopump*. MScEng Thesis: Mechanical Engineering, University of KwaZulu-Natal: Durban.

Franc, J.-P., Rebattet, C. and Coulon, A. (2004) 'An Experimental Investigation of Thermal Effects in a Cavitating Inducer', *Journal of Fluids Engineering*, 126(5), p. 716. doi: 10.1115/1.1792278.

Furst, R. B. (1973) *Liquid Rocket Engine Centrifugal Flow Turbopumps*, *NASA Space Vehicle Design Criteria*. Cleveland, Ohio: Lewis Research Centre, NASA SP-8109.

Gu, F., Thilges, C. and Cambio, M. (2010) 'Extracting Two-Zone Model Parameters for Centrifugal Compressor Design', in *ASME Turbo Expo proceedings*. Glasgow, UK: American Society of Mechanical Engineers, pp. 1847–1857.

Gulich, J. F. (2014) *Centrifugal Pumps*. 3rd edn. Villeneuve, Switzerland: Springer-Verlag Berlin Heidelberg. doi: 10.1007/978-3-642-40114-5.

Haidn, O. J. (2008) *Advanced Rocket Engines*. Neuilly-sur-Seine, France: RTO. Available at: https://www.sto.nato.int/publications/STO Educational Notes/RTO-EN-AVT-150/EN-AVT-150-06.pdf (Accessed: 18 January 2017).

Hands, B. A. (1986) *Cryogenic Engineering*. 1st edn. London. UK: Academic Press Ltd.

Haselden, G. (1971) *Cryogenic Fundamentals*. 1st edn. London: Academic Press Ltd.

Hawash, S. A. F., Abdullah, E., Mohamed, H. I. and Shehata, M. H. (2015) 'Slip factor evaluation for centrifugal pump impeller with and without splitter blades, using CFD technique', *International Journal of Innovative Research and Creative Technology*, 1(2), pp. 131–138.

High Performance Alloys (2013) *Bars and Forgings in Inconel 718*, *AZO Materials*. Available at: https://www.azom.com/article.aspx?ArticleID=8249 (Accessed: 29 August 2017).

Hosangadi, A., Ungewitteif, R. J. and Ahuja, V. (2004) 'Simulations of Cavitating Cryogenic Inducers', in *40th AIAA Joint Propulsion Conference and Exhibit proceedings*. Fort Lauderdale, Florida: American Institute of Aeronautics and Astronautics, pp. 1–11. doi: https://doi.org/10.2514/6.2004-4023.

Hoshide, R. K. and Nielsen, C. E. (1973) *Study of Blade Clearance Effects on Centrifugal Pumps*. NASA Lewis Research Centre Cleveland, Ohio: NASA CR-120815.

Huzel, D. and Huang, D. (1992) *Modern Engineering Design of Liquid-Propellant Rocket Engines*. Revised. Washington, US: American Institute of Aeronautics and Astronautics.

Japikse, D. (1985) 'Assessment of Single and Two-Zone Modeling of Centrifugal Compressors', in *International Gas Turbine Conference and Exhibit proceedings*. Houston, Texas: American Society of Mechanical Engineers, pp. 1–13. doi: 10.1115/85-GT-73.

Japikse, D., Marscher, W. D. and Furst, R. B. (1997) *Centrifugal Pump Design and Performance*. 1st edn. White River Junction, VT: Concepts NREC.

Jewett, R. and Halchak, J. (1991) 'The Use of Alloy 718 in the Space Shuttle Main Engine', in *Superalloys 718, 625 and Various Derivatives*. Canoga Park, California: The Minerals, Metals and Materials Society.

Johnson, M. W. and Moore, J. (1980) 'The Development of Wake Flow in a Centrifugal Impeller', *Journal of Engineering for Power*. American Society of Mechanical Engineers, 102(2), pp. 382–389. doi: 10.1115/1.3230265.

Kalia, S. and Fu, S. Y. (2013) *Polymers at cryogenic temperatures*. 1st edn, *Polymers at Cryogenic Temperatures*. 1st edn. Solan, India: Springer Berlin Heidelberg. doi: 10.1007/978-3-

642-35335-2.

Kamijo, K., Sogame, E. and Okayasu, A. (1982) 'Development of Liquid Oxygen and Hydrogen Turbopumps for the LE-5 Rocket Engine', *Journal of Spacecraft and Rockets*, 19(3), pp. 226–231. doi: 10.2514/3.62241.

Kanagaraj, S. and Pattanayak, S. (2004) 'Thermal Expansion of Glass Fabric-Epoxy Composites at Cryogenic Temperatures', in *AIP Conference Proceedings*. American Institute of Physics, pp. 201–208. doi: 10.1063/1.1774570.

Kang, C. and Li, Y. (2015) 'The effect of twin volutes on the flow and radial hydraulic force production in a submersible centrifugal pump', *Proceedings of the Institution of Mechanical Engineers, Part A: Journal of Power and Energy*, 229(2), pp. 1–17. doi: 10.1177/0957650914562920.

Karassik, I. J., Messina, J. P., Cooper, P. and Heald, C. C. (2001) *Pump Handbook*. 3rd edn. New York, USA: McGraw-Hill Professional.

Kergourlay, G., Younsi, M., Bakir, F. and Rey, R. (2007) 'Influence of Splitter Blades on the Flow Field of a Centrifugal Pump : Test-Analysis Comparison', *International Journal of Rotating Machinery*, 2007(1), p. 13. doi: 10.1155/2007/85024.

Lemmon, E. and Jacobsen, R. (2004) 'Viscosity and Thermal Conductivity Equations for Nitrogen, Oxygen, Argon, and Air', *International Journal of Thermophysics*, 25(1), pp. 21–69. doi: 10.1023/B:IJOT.0000022327.04529.f3.

Malone, H. E. (1976) *Analysis of Rocket Propellants*. 1st edn. New York: Academic Press Inc. Ltd.

Mikhail, S., Khalafallah, M. G. and El-Nady, M. (2001) 'Disk Friction Loss In Centrifugal and Mixed Flow Pumps', in *Seventh International Congress on Fluid Dynamics and Propulsion*. Cairo, Egypt, pp. 1–6.

Milberg, E. (2016) *SpaceX Successfully Tests Carbon Fiber Tank for Mars Spaceship*, *Composites Manufacturing*. Available at: http://compositesmanufacturingmagazine.com/2016/11/spacex-successfully-tests-carbon-fiber-tank-mars-spaceship/ (Accessed: 27 March 2017).

NASA (1996) *Safety Standard for Oxygen and Oxygen Systems*. Office of Safety and Mission Assurance, Washington DC: NASA NSS 1740.15.

Oh, H. W. and Chung, M. K. (1999) 'Optimum Values of Design Variables Versus Specific Speed for Centrifugal Pumps', in *Institution of Mechanical Engineers, Part A: Journal of Power and Energy proceedings*. Institution of Mechanical Engineers, pp. 219–226. doi: 10.1243/0957650991537563.

Ono, Y., Yuri, T., Sumiyoshi, H., Takeuchi, E., Matsuoka, S. and Ogata, T. (2006) 'High-Cycle Fatigue Properties at Cryogenic Temperatures in INCONEL 718', in *AIP Conference Proceedings*, pp. 184–191. doi: http://dx.doi.org/10.1063/1.2192350.

Pavesi, G., Cavazzini, G., Santolin, A., Ardizzon, G. and Lorenzi, R. (2015) 'Using Splitter Blades to Improve Suction Performance of Centrifugal Impeller Pumps', in *Institution of Mechanical Engineers, Part A: Journal of Power and Energy proceedings*. Institution of Mechanical Engineers, pp. 309–323. doi: 10.1177/0957650914563364.

Pelton, R. J. (2007) *One-Dimensional Radial Flow Turbomachinery Performance Modeling*. MScEng Thesis: Mechanical Engineering, Brigham Young University, US.

Pentermann, W. and Wagner, W. (1978) 'New Pressure-Density-Temperature Measurements and New Rational Equations for the Saturated Liquid and Vapour Densities of Oxygen', *The Journal*

of Chemical Thermodynamics, 10(12), pp. 1161–1172. doi: http://dx.doi.org/10.1016/0021-9614(78)90033-2.

Performance Composites (2017) *Carbon Fiber Composite Design Guide*, *Performance Composites*. Available at: http://www.performancecomposites.com/about-composites-technical-info/124-designing-with-carbon-fiber.html (Accessed: 27 March 2017).

Philogene, L. C. (2014) *Development of a Universal Impeller Test Rig for Scaled Testing of High Performance Impellers*. MScEng Thesis: Mechanical Engineering, University of KwaZulu-Natal:

Qiang, X., Teng, J. and Du, Z. (2010) 'Influence of various volute designs on volute overall performance', *Journal of Thermal Science*, 19(6), pp. 505–513. doi: 10.1007/s11630-010-0416-7.

Rachov, P. (2010) *Electric Feed Systems for Liquid Propellant Rocket Engines*. Buenos Aires: University of Buenos Aires. doi: 10.13140/2.1.4431.9042.

Richings, M. J. (2015) *The Prediction of Cavitation in High Speed Centrifugal Pumps*. MScEng Thesis: Mechanical Engineering, University of KwaZulu-Natal:

Rocket Lab (2017) *Electron*, *Rocket Labs*. Available at: https://www.rocketlabusa.com/electron/ (Accessed: 27 January 2017).

Rodgers, C. (1978) 'A Diffusion Factor Correlation for Centrifugal Impeller Stalling', *Journal of Engineering for Power*, 100(4), pp. 1–10. doi: 10.1115/1.3446403.

Schilling, J. (2009) *Launch Vehicle Performance Calculator*. Silverbird Astronautics. Available at: http://silverbirdastronautics.com/LVperform.html (Accessed: 3 April 2017).

Scott, R. B. (1963) *Cryogenic Engineering*. Princeton, NJ: Van Nostrand Company.

Smyth, J. (2014) *The Design and Analysis of a Kerosene Turbopump for a South African Commerical Launch Vehicle*. MScEng Thesis: Mechanical Engineering, University of KwaZulu-Natal:

Spaceflight 101 (2017) *Electron*, *Spaceflight*. Available at: http://spaceflight101.com/spacerockets/electron/ (Accessed: 27 January 2017).

Special Metals (2017) *Inconel 718*, *Special Metals*. Available at: http://www.specialmetals.com/assets/smc/documents/inconel_alloy_718.pdf (Accessed: 25 September 2017).

Stepanoff, A. J. (1949) *Centrifugal and Axial Flow Pumps*. 2nd edn. Krieger Publishing Company.

Stewart, R. B. and Jacobsen, R. T. (1991) 'Thermodynamic Properties of Oxygen from Triple Point to 300 K with Pressures to 80 MPa', *Physical and Chemical Reference Data*, 20(5), pp. 919–1021. doi: https://doi.org/10.1063/1.555897.

Strain, W. (2008) *Design of an Oxygen Turbopump for a Dual Expander Cycle Rocket Engine*. MScEng Thesis: Aeronautics and Astronautics, Air Force Institute of Technology.

Stripling, L. B. and Acosta, A. J. (1962) 'Cavitation in Turbopumps—Part 1', *Journal of Basic Engineering*. American Society of Mechanical Engineers, 84(3), pp. 326–338. doi: 10.1115/1.3657314.

Sutton, G. (2001) *Rocket Propulsion Elements*. 7th edn. USA: John Wiley & Sons.

Turner, M. J. L. (2006) *Rocket and Spacecraft Propulsion*. 2nd edn. Leicester, UK: Springer.

Valence (2017) *Valence Product*, *Valence*. Available at: https://www.valence.com/products/ (Accessed: 2 December 2017).

Vector Space Systems (2017) *Vector*, *Vector Space Systems*. Available at: https://vectorspacesystems.com/company/ (Accessed: 1 September 2017).

Weber, L. (1977) *Thermodynamic and Related Properties of Oxygen from the Triple Point to 300 K at Pressures to 1000 Bar*. National Bureau of Standards NBSIR 77-865: Boulder, Colorado.

Wiesner, F. J. (1967) 'A Review of Slip Factors for Centrifugal Impellers', *Journal of Engineering for Gas Turbines and Power*, 89(4), pp. 558–566. doi: 10.1115/1.3616734.

Wilcox, D. C. (2008) 'Formulation of the k-ω Turbulence Model Revisited', *AIAA Journal*, 46(11), pp. 2823–2838. doi: 10.2514/1.36541.

Woellert, K., Ehrenfreund, P., Ricco, A. J. and Hertzfeld, H. (2011) 'CubeSats: Cost-effective science and technology platforms for emerging and developing nations', *Advances in Space Research*, 47(4), pp. 663–684. doi: https://doi.org/10.1016/j.asr.2010.10.009.

Wood, G. M., Welna, H. and Lamers, R. P. (1965) 'Tip-Clearance Effects in Centrifugal Pumps', *Journal of Basic Engineering*. American Society of Mechanical Engineers, 87(4), pp. 932–939. doi: 10.1115/1.3650846.

Wunderlin, N., Pitot, J. and Brooks, M. (2017) 'Design of an Ablatively Cooled Combustion Chamber for the SAFFIRE Engine'. Pretoria, South Africa: AESSA Presentation.

Xu, J., Wu, Y., Zhang, Y. and Zhang, J. (2010) *Fluid Machinery and Fluid Mechanics: 4th International Symposium (4th ISFMFE)*. 1st edn. Springer Berlin Heidelberg.

Appendix A: Fluid Data

Table A-1: Liquid oxygen viscosity (Lemmon and Jacobsen, 2004)

Parameter	**Value**
$\frac{\epsilon}{k}$ (K)	118.5
σ (nm)	0.3428
Collision Integral Equation coefficients	
i	**b_i**
0	0.431
1	-0.4623
2	0.08406
3	0.005341
4	-0.00331

Residual fluid viscosity coefficients				
i	**N_i**	**t_i**	**d_i**	**l_i**
1	17.67	0.05	1	0
2	0.4042	0.0	5	0
3	0.0001077	2.10	12	0
4	0.3510	0.0	8	1
5	-13.67	0.5	1	2

Appendix B: PUMPAL™ Preliminary Design Output File

```
PUMPAL 8.5.12
 RUN ID: Output run ID
--------------------------------------------------------------------------------
 Stage   1 of   1:

********************************************************************************
GENERAL SETTINGS
********************************************************************************
 Run Mode:              Design
 Fluid Type:            NIST 7.2 real fluid
                         -OXYGEN:1.0000
 Solver Type:           Wilder two-zone model
 Stage Layout:
   -IGV:                None
   -Impeller:           Open with no seal
   -Diffuser:           1: Vaneless;
   -Exit:               Volute
 Unit System:           Metric
   -Angle reference:    Tangential
   -Length:             mm
   -Velocity:           m/s
   -Flow:               Kg/s
   -Pressure:           KPa
   -Head rise:          m
   -Temperature:        K
   -Power:              kW


 ********************************************************************************
 *     STATION-BY-STATION OUTPUTS                                               *
 ********************************************************************************

 >>>>>>>>>>>>>>>>>>>
 Upstream (Station 0)
 >>>>>>>>>>>>>>>>>>>

T00 = 80.00      P00 = 300.00     M = 6.13   N = 23000.00

 >>>>>>>>>>>>>>>>>>>>>>>>
 Impeller Inlet (Station 1)
 >>>>>>>>>>>>>>>>>>>>>>>>

R1H       = 10.000    R1M     = 14.584     R1T = 18.038     LEN1 = 0.000
BETA1HB = 18.648    BETA1MB = 13.925     BETA1TB = 11.974
PHI1 = 90.000
 ZI      = 4          TLET    = 0.500      CLRF    = 0.800      Mass_in = 6.130
 BLK1    = 0.020      LC1     = 0.010      AK      = 1.030      Throat Area= 170.890

_____________________Impeller Inlet Hub (Station 1H) _____________________
 C       = 7.20       CM      = 7.20       CT      = 0.00       ALPHA   = 90.00
 W       = 25.14      WT      = -24.09     BETA    = 16.65      I       = 2.00
 U       = 24.09                           RHO     = 1190.91
 P       = 268.79     P0      = 299.67     T       = 80.00      T0      = 80.00

_____________________Impeller Inlet RMS (Station 1M) _____________________
 C       = 7.42       CM      = 7.42       CT      = 0.00       ALPHA   = 90.00
 W       = 35.90      WT      = -35.13     BETA    = 11.92      I       = 2.00
 U       = 35.13                           RHO     = 1190.91
 P       = 266.91     P0      = 299.67     T       = 79.99      T0      = 80.00

_____________________Impeller Inlet Tip (Station 1T) _____________________
 C       = 7.64       CM      = 7.64       CT      = 0.00       ALPHA   = 90.00
 W       = 44.11      WT      = -43.45     BETA    = 9.97       I       = 2.00
```

```
U       = 43.45                          RHO     = 1190.90
P       = 264.91     P0      = 299.67    T       = 79.99      T0      = 80.00

_____________________Operating Range_____________________________________
Cavitation Model:    Traditional
                     NPSHR   = 12.90     CAVCOEF = 0.10

>>>>>>>>>>>>>>>>>>>>>>>>>>>
Impeller Exit (Station 2)
>>>>>>>>>>>>>>>>>>>>>>>>>>>

R2avg   = 37.388     R2rms   = 37.388    R2hub   = 37.388     R2tip   = 37.388
B2      = 4.228      BETA2B  = 22.500    CLRR    = 0.800      TN      = 0.600
AxLngth = 20.137     ZR      = 8         Rexp    = 37.388     Bexp    = 4.228

DR2     = 1.29       DR2I    = 3.10
MSECM   = 0.20       E       = 0.71      MU      = 0.12       LAM2    = 12.49
SIG2    = 0.83       DELTA2P = 3.23      DELTA2S = 0.00       Mass_out= 6.13
ETAa    = 0.60       ETAb    = 0.30      DRstall = 1.50

_____________________Primary Zone (Station 2P)____________________________
C2P     = 60.99      CM2P    = 14.90     CT2P    = 59.14      ALPHA2P = 14.14
W2P     = 34.31      U2P     = 90.05     BETA2P  = 25.73      DELTA2P = 3.23
P2P     = 4434.50    P02P    = 6659.04   T2P     = 80.65      T02P    = 80.99

_____________________Secondary Zone (Station 2S)__________________________
C2S     = 86.33      CM2S    = 1.55      CT2S    = 86.32      ALPHA2S = 1.03
W2S     = 4.04       U2S     = 90.05     BETA2S  = 22.50      DELTA2S = 0.00
P2S     = 4434.50    P02S    = 8892.05   T2S     = 81.00      T02S    = 81.69

_____________________Mixed-Out (Station 2M)_____________________________
C2M     = 64.78      CM2M    = 5.17      CT2M    = 64.57      ALPHA2M = 4.58
W2M     = 25.99      U2M     = 90.05     BETA2M  = 11.47      DELTA2M = -11.03
P2M     = 4478.04    P02M    = 6985.75   T2M     = 80.94      T02M    = 81.33
M2M_ABS = 0.06       RHO2M   = 1193.86

_____________________Parasitic Power Losses _____________________________
PRD     = 0.90       PBF     = 0.71      PFC     = 0.00       PRC     = 0.00
PRD/PEUL= 0.03       PBF/PEUL= 0.02      PFC/PEUL= 0.00       PRC/PEUL= 0.00

>>>>>>>>>>>>>>>>>>>>>>>>>>>>>>>
Diffuser #1: Vaneless Diffuser
>>>>>>>>>>>>>>>>>>>>>>>>>>>>>>>

Rin     = 37.388     Rex     = 44.865    Bin     = 4.228      Bex     = 4.651
Rpin    = 33.649     Bpin    = 3.805     PHIex   = 90.000     LENaxial= 0.000
Model Option:        Reynolds number correlation.

Cex     = 47.510     CMex    = 3.787     CTex    = 47.358     ALPHAex = 4.572
Pex     = 5159.438   P0ex    = 6507.110  Tex     = 81.288     T0ex    = 81.498
                     RHOex   = 1193.449  Mass_out= 6.130      BLK     = -0.034
CP      = 0.272      LC      = 0.191     Re      = 2423680.243 CF     = 0.006


VANELESS SPACE CALCULATION       :
-------------------------------------------------------------------------------
  R        B      CM    CT     T        P         P0    ALPHA CP   LC %Tr-1 %FR-1
37.388   4.228   5.2   64.6   80.9  4478.039  6985.742   4.6 0.00 0.00 0.00  0.00
38.634   4.181   4.9   61.1   81.0  4633.575  6878.515   4.6 0.06 0.04 0.10 -3.33
39.880   4.275   4.6   57.9   81.1  4768.611  6784.549   4.6 0.12 0.08 0.18 -3.33
41.126   4.369   4.4   55.0   81.1  4886.320  6701.910   4.6 0.16 0.11 0.25 -3.33
42.373   4.463   4.2   52.2   81.2  4989.313  6628.987   4.6 0.20 0.14 0.32 -3.33
43.619   4.557   4.0   49.7   81.2  5079.753  6564.431   4.6 0.24 0.17 0.38 -3.33
44.865   4.651   3.8   47.4   81.3  5159.438  6507.110   4.6 0.27 0.19 0.43 -3.33
-------------------------------------------------------------------------------

>>>>>>>>>>>>>>>>>>>>>>>>>>>>>>>
```

```
Volute (Single Exit)
>>>>>>>>>>>>>>>>>>>>>>>>>>>>>>>

D7      = 13.05      D8      = 30.00      A7      = 133.68     A8      = 706.86
AR      = 0.10       ExitLen = 228.68     NormArea= 13.37      VR7     = 44.87

C7      = 42.69      C8      = 7.26
P7      = 5348.10    P07     = 6436.24    P8      = 6300.98    P08     = 6332.47
T7      = 81.35      T07     = 81.52      T8      = 81.55      T08     = 81.56

CP57    = 0.14       CP78    = 0.88       CP58    = 0.85       CP57design= 0.14
LC57    = 0.05       LC78    = 0.10       LC58    = 0.13       LAMAR   = 1.28
```

FULL AREA DISTRIBUTION

Angle	Area	Angle	Area	Angle	Area	Angle	Area
0	13.3676			180	73.5220		
15	18.3805	105	48.4577	195	78.5349	285	108.6121
30	23.3934	120	53.4706	210	83.5477	300	113.6249
45	28.4062	135	58.4834	225	88.5606	315	118.6378
60	33.4191	150	63.4963	240	93.5735	330	123.6507
75	38.4320	165	68.5091	255	98.5863	345	128.6635
90	43.4448	180	73.5220	270	103.5992	360	133.6764

```
Mass_out= 6.130

Mass Flow Rate(Kg/s)                        6.130
Volume Flow Rate (m^3/s)                    0.005
Power (kW)                                  37.258

Head Rise (m)
    -Total-To-Total                         516.516
    -Total-To-Static                        513.820

Stage Efficiency
    -Adiabatic, Total-To-Total              0.831
    -Adiabatic, Total-To-Static             0.827

Rotor Efficiency
    -Total-To-Total, without leakage        0.921

Rotor Reaction
    -Enthalpy based                         0.659
    -Pressure based                         0.691

Efficiency Decrement
    -Inlet duct loss                        0.000
    -Impeller total loss                    0.079
       *Internal loss                                0.037
       *Recirculation loss                           0.019
       *Disk friction loss                           0.023
       *Front leakage loss                           0.000
       *Rear leakage loss                            0.000
    -Total diffuser efficiency decrement    0.066
    -Exit element efficiency decrement      0.024
    -Exit leaving kinetic energy            0.004

Flow Coefficient
    -CM1m/U1m                               0.211
    -CM2m/U2m                               0.057
    -MFLOW/(RHO00*N*D2^3)                   0.032
    -MFLOW/(RHO02*N*D2^3)                   0.032

Head Coefficient
    -T-T, (H0ex_ise-H00)/(U2^2)             0.623
    -T-S, (Hex_ise-H00)/(U2^2)              0.620
```

```
Work Coefficient
    -(H0ex-H0in)/(U2^2)                     0.750

Power Coefficient
    -Power/(RHO00*N^3*D2^5)                 0.238

Specific Speed (based on stage total head rise)
    -Non-dimensional                        0.288
    -US unit, N*Q^0.5/(dH)^0.75             787.032
    -Metric unit, N*Q^0.5/(dH)^0.75         15.241
```

Appendix C: Preliminary Star-CCM+™ Results

The preliminary Star-CCM+™ analysis utilised the same CAD preparation, mesh generation and steady-state physics models as discussed in Section 6.2, Section 6.3 and Section 6.4.1. Figure C-1 and Figure C-2 are static pressure and velocity scenes showing the development of the fields through the impeller geometry. The preliminary design delivers 52.08 bar of pressure and a mass flow rate of 6.1297 kg/s. This was below the required delivery pressure of 62.8 bar, prompting the subsequent re-design of the pump impeller.

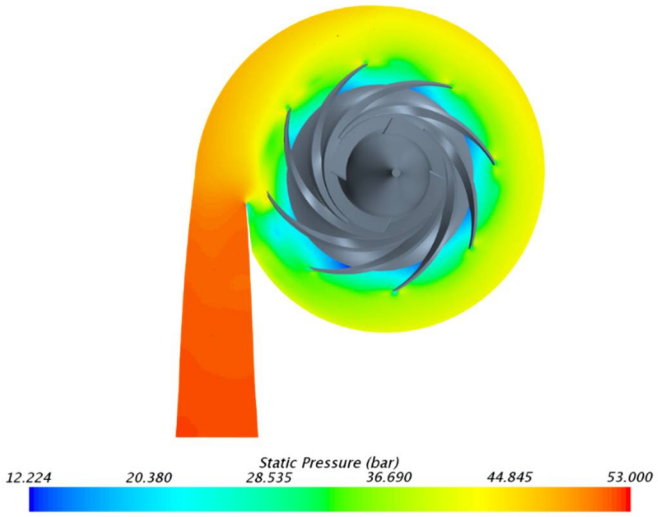

Figure C-1: Static pressure development through preliminary impeller design

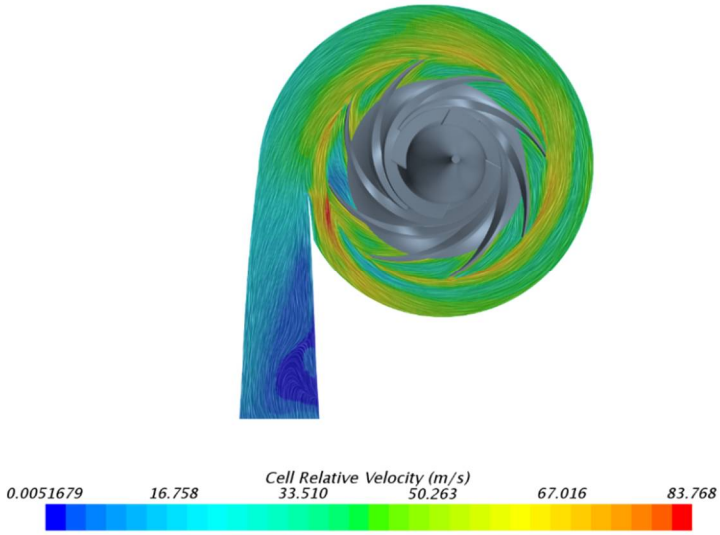

Figure C-2: Velocity field in X-Y plane